STATISTICAL SHAPE MODELING FOR CUSTOM DESIGN AND ANALYSIS

by

Xilu Wang

A dissertation submitted in partial fulfillment of
the requirements for the degree of

Doctor of Philosophy

(Mechanical Engineering)

at the

UNIVERSITY OF WISCONSIN–MADISON

2017

Date of final oral examination: 10/06/2017

The dissertation is approved by the following members of the Final Oral Committee:
Dr. Qian, Xiaoping, Professor, Mechanical Engineering
Dr. Shapiro, Vadim, Professor, Mechanical Engineering
Dr. Suresh, Krishnan, Professor, Mechanical Engineering
Dr. Thelen, Darryl, Professor, Mechanical Engineering
Dr. Liu, Kaibo, Assistant Professor, Industrial & Systems Engineering

To my parents, who cultivated my interest in science when I was young

Acknowledgments

Foremost, I would like to express my sincere gratitude to my advisor Professor Xiaoping Qian for the continuous support and guidance of my Ph.D study and research.

Besides my advisor, I would like to thank the rest of my thesis committee: Professor Vadim Shapiro, Professor Krishnan Suresh, Professor Darryl Thelen, and Professor Kaibo Liu, for their insightful comments that help enrich my work.

My sincere thanks also goes to Dr. Songtao Xia, Dr. Kang Li, Dr. Kangmin Xu, who were the senior students in the lab and helped me a lot in my research and studies.

I thank my fellow labmates in UW Computational Design and Manufacturing Laboratory for the inspiring discussions and for the fun we have in the last four years.

I thank all my friends here for the help I received from them.

Last but not the least, I would like to thank my parents, Yun Wang and Fengchun Wen, for giving birth to me, raising me and cultivating me. Without their supports and encouragements, I cannot achieve what I've achieved now.

Contents

List of Tables

List of Figures

Abstract

The goal of this dissertation research is to use pre-existing shape data to improve efficiency and quality of custom design and analysis.

The rapid advancement of sensor miniaturization and growing sensor networks and computer power has lead to wide availability of massive shape data from populations of objects. Such massive shape data range from human body shapes to longitudinal knee observations of osteoarthritis patients. Populations of shape data also include shapes of man-made objects, such as part shapes of the same model due to manufacturing process variation as well as part shapes due to shape degradation after deployment. Mining and analysis of such massive population-based shape data can result in knowledge of shape variability of the population and lead to the construction of faithful subject-specific 3D shape models from sparse measurements. It is then possible to predict shape-specific functional performance and population-wide structural performance variation. Such an ability brings about unprecedented capabilities and tantalizing opportunities for mass customization, part-specific failure prediction and just-in-time part maintenance, and patient-specific biomedical intervention and treatment.

This work aims at developing efficient approaches that can: 1) construct faithful subject-specific shape models from sparse measurements; 2) predict shape-specific structural performance from a given subject-specific shape model; and 3) predict structural performance variation over a shape population. Toward this end, we present

a statistical atlas based approach that incorporates statistical shape modeling in subject-specific shape reconstruction, finite element (FE) modeling and analysis.

The statistical atlas contains three parts: the mean shape and the variation modes of the shape population which span a linear shape space, the FE mesh of the mean shape, and the selected feature points and sizing dimensions. The feature points and sizing dimensions are selected by maximizing the total variance they capture of the shape population. Given a subject (e.g. a person), the corresponding dimensions are measured and the subject specific shape model is synthesized. The FE mesh of the mean shape serves as the template mesh which can be morphed to the subject shape to conduct subject-specific FE analysis. The FE solution on the template mesh can also be extrapolated to the subject shape through Taylor expansion. The shape variances along the variation modes are obtained by the principal component analysis. These variances tell the amount of shape variabilities in the population and are combined with the Taylor expansion of the FE solution to obtain the structural performance variation across the population. The numerical testings with various 2D and 3D shape databases demonstrate the efficiency and effectiveness of the proposed approach for custom design and analysis.

In this dissertation a statistical atlas based framework is developed for custom design and analysis. The main contributions of this work are: 1) An approach that selects feature points and sizing dimensions based on the total variance captured of the shape population. 2) Automated subject-specific FE modeling through mesh morphing based on the shape correspondence obtained by searching in the shape space. A multi-correlation based metric is developed to evaluate the quality of the obtained

shape correspondences. 3) A Taylor expansion approach for predicting subject-specific structural performance and computing structural performance variation over a shape population. Multi-point Taylor expansion approach is developed for the cases that the structural performance is highly nonlinear with respect to the shape parameters.

1

Introduction

The goal of this dissertation research is to use pre-existing shape data to enhance custom design and analysis. It is achieved through building a statistical atlas that incorporates statistical shape modeling in subject-specific shape reconstruction, finite element (FE) modeling, and finite element analysis.

1.1 Background, motivation and challenges

The rapid advancement of sensor miniaturization and growing sensor networks and computer power has lead to wide availability of massive shape data from populations of objects. Such massive shape data range from human body shapes in Civilian American and European Surface Anthropometry Resource [1] and Size China [2], to longitudinal knee observations of a large population of osteoarthritis patients [3]. Populations of shape data also include shapes of man-made objects, such as part shapes of the same model due to manufacturing process variation as well as part shapes due to shape degradation after deployment. Mining and analysis of such massive population-based shape data can result in knowledge of shape variability of the population and lead to the construction of faithful subject-specific 3D shape models from sparse measurements. It is then possible to predict shape-specific

functional performance and population-wide structural performance variation. Such an ability brings about unprecedented capabilities and tantalizing opportunities for mass customization [4; 5], part-specific failure prediction [6; 7] and just-in-time part maintenance, and patient-specific biomedical intervention and treatment [8; 9]. Thus this work aims at developing efficient approaches that can: 1) construct faithful subject-specific shape models from sparse measurements; 2) predict shape-specific structural performance from the given subject-specific shape model; and 3) compute structural performance variation over the shape population.

1.1.1 Constructing faithful subject-specific shape models

Constructing faithful subject-specific shape model for a given subject is the first step to custom design and analysis. For example, subject-specific human body shape models are used in virtual reality for custom fitting and interaction design of personalized items like eye-glasses [5], shoes [4], and helmet [10]. The shape models of patient-specific anatomical structures (tibias, femurs) are used in the implant design [11] and prediction of structural performance via subject-specific finite element analysis [8; 12]. However, due to the tedious and error-prone process [13] of obtaining neat subject shape models from images or scanned point clouds, its applications have been limited.

In order to address this issue, methods that bypass the above processes have been proposed. For example, parametric shape models [14; 13; 15] are widely used in personalized customization, where the complete shape model of a subject is generated by a few dimensions measured on the subject (sparse measurements). However,

as pointed out in [5], there is no standardized method to determine what suitable dimensions are and how to choose them. Sparse shape reconstruction is another technique [16; 17] for rapid shape completion. The inputs are the positions of the sparse markers on the subject obtained by sensors. The output is the reconstructed shape. Similarly, the challenge is where to put the markers so we can have faithful reconstructions.

Feature points are the points that capture the geometric characteristics of an object. They usually have certain anatomical significance or geometric meaning. For example, the left and right lateral malleolus points on the human body model in the CAESAR project [1] are among the anatomical feature points. The high curvature points and the extremity points are often used as geometric feature points. In [4], the heel point is defined as "the vertex having the smallest x-coordinate value". The selection of feature points is a fundamental problem in computer graphics [18] and in CAD based custom data [14; 13] with various applications. The selected feature points are used as the marker points based on which the 3D shape is reconstructed [16; 17; 19]. In parametric shape design, the feature points are used to generate semantic features [14; 13] and are used as the reference points for constructing meaningful sizing dimensions[4; 5].

In the literature, feature point is selected on a single shape by its differential property or the saliency. For example, in [20] the feature points are automatically calculated on a shape by scale saliency [21]. In [22] a center-surround operator on Gaussian-weighted mean curvatures is used to calculate saliency map on the shape. In [23], the vertices on the convex hull of the multi-dimensional scaling (MDS) transform

of the 3D mesh are selected as the feature points. In [16; 14] the landmarks on the human body model were chosen by the anthropometry. In [24] the 14 feature points are chosen from among the local protrusion points, high-curvature points, and anatomically meaningful points.

Being carefully designed, the feature points selected by the above approaches can represent the corresponding shape well. However, the population information of similar shapes are not considered and the variations between different shapes in the population are overlooked. Often, capturing the shape variations in the population is important, especially in sparse shape reconstruction and parametric shape design.

The inputs to sparse shape reconstruction are the coordinates of sparse markers, and the output is the reconstructed shape. The mapping from the feature points to the complete shape is learned by regressing the shape examples in the training set on the coordinates of the feature points [17]. If there exist variations in the population that are not captured by the feature points, then no matter how sophisticated the regression method is, the reconstructed shape would be very different from the real shape, since some of the population information is missing.

Figure 1.1 shows the effects of different marker points on sparse shape reconstruction. The marker points in the top row are located at the tips of the fingers, the marker points in the bottom row are located at the valleys of the fingers. From the perspective of saliency, both of them are prominent points at high curvature areas. However, as could be seen in Figure 1.1(b) and 1.1(e), the marker points in the top row have captured the swings of the fingers while the marker points in the bottom row have not. Since swings of fingers are the major variations in the population

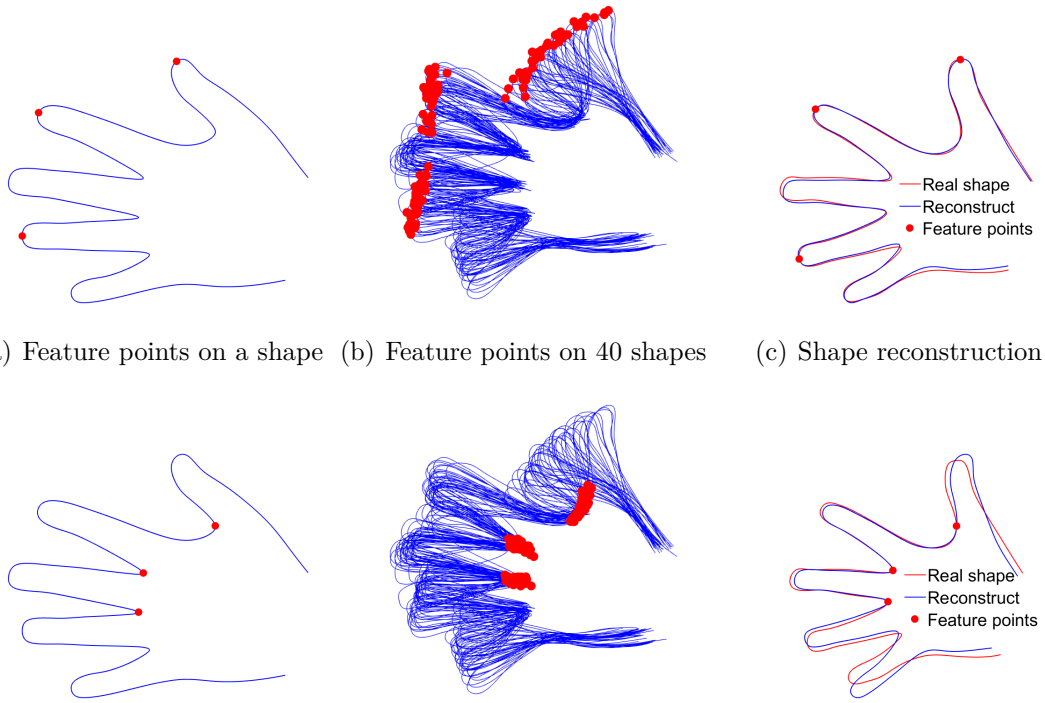

(a) Feature points on a shape (b) Feature points on 40 shapes (c) Shape reconstruction

(d) Feature points on a shape (e) Feature points on 40 shapes (f) Shape reconstruction

Figure 1.1: The effects of different marker points on the sparse shape reconstruction.

(compared to size and local shape changes), failing to capture them would lead to major loss of the population information. As shown in Figure 1.1(c) and 1.1(e), the shape reconstructed by the marker points in the top row is closer to the real shape than that of the bottom row.

Similarly for the parametric shape design, where the inputs are the sizing dimensions, the output is the synthesized shape. The mapping from sizing dimensions to the complete shape is learned by regressing the shape examples in the training set on the measured sizing dimensions [13; 14]. The obtained parametric shape model can then be used in, for example, mass-customization of foot wear [4] and personalized item

design (eyeglass) [5]. In [4], 24-foot dimensions (including heel length and midfoot width) are manually chosen among the lengths and angles constructed from the 14 geometric feature points. In [5], 12 dimensions that are related to facial anatomy are chosen by referring to the anatomical landmarks. Since capturing population information is helpful for shape reconstruction and synthesis, we hypothesize that the chosen sizing dimensions must capture the shape variations in the population.

1.1.2 Predicting shape-specific structural performance

The obtained subject-specific shape model enables us to predict the shape-specific structural performance through finite element modeling and analysis. The ability of in-time prediction of shape-specific structural performance from the given subject shape model is critical in clinical settings such as surgical planning, surgical guidance during surgery, and patient-specific biomedical intervention and treatment [6; 9]. However, the task of creating FE meshes such as hexahedral mesh for each subject shape usually requires manual intervention and can be tedious and time consuming. For example, in [8; 7] it takes 10 hours to create high quality hexahedral mesh for the ascending aorta from the boundary triangulations by Hypermesh software. Such lack of automation in FE modeling and its lengthy laborious process pose substantial challenges for applications where FE modeling and analysis need to be done in a short period of time. The ability to automate FE modeling of subject-specific shapes would enable the wider application of subject-specific models with applications in surgical planning, implant design and maintenance, and patient-specific treatment.

In the literature, a common approach to efficient shape modeling or FE modeling of subject-specific objects is through template-based deformation. For example, morphing template meshes to subject-specific shapes has been explored in [25; 26; 27]. A mesh morphing approach to conducting statistical models of femurs was studied in [28]. However, it has not been used to generate subject-specific FE models. Recently, an atlas based geometry pipeline for constructing three-dimensional cubic Hermite finite element meshes from tomographic patient image data and deforming the atlas to a second patient has been studied in [29].

Their approaches contain two steps: 1) registration of the subject shape [25; 26; 27; 28] or image [29] to the template shape; 2) FE mesh morphing of the template mesh to the subject with the shape correspondence obtained in the registration. However, their approaches are unaware of the specificity of the subject shapes and have the issues of: 1) too many variables to control the registration; 2) lack of robustness; 3) manually dependent. For example, in the free-form deformation, as pointed out by [27], the resolution of the deformation should be approximately the size of the smallest anatomical structures to be registered, so it requires a large number of degrees of freedom (thousands) for the accurate registration of fine structures. This makes the problem complex, inefficient and more importantly, not robust. Thus when a subject shape deviates significantly from the template shape, a simple deformation based approach, without manual specification of corresponding landmarks between the template shape and the given shape, would fail to generate proper correspondence between the two shapes. Therefore, the FE mesh cannot be properly transferred from the template shape to the given shape. How to choose the template mesh also

remains an issue in their approaches, which will affect the subject shape registration and later volumetric mesh morphing.

For a certain class of shapes, the shape variations follow some particular patterns, and the deformations within the class are really constrained by a limited number of degrees of freedom. Thus it is important to analyze the pre-existing shapes examples and use the learned knowledge of the population to guide the shape registration and help automate the FE modeling.

In the literature, approximation based approaches exist for structural performance prediction that bypass the process of subject-specific FE modeling. For example, in structural reliability analysis [30; 31; 32; 33], Taylor expansion is used to extrapolate the FE solution of the template mesh to subject-specific structures. However, the Taylor expansion approach requires parameterization of the finite element model with respect to the design variables for sensitivity analysis. In the literature, such design variables are usually material properties (e.g. density, Young's modular) and sizes (e.g. lengths, thickness, fillet radius, tangential and axial directions). However, for many subject shapes, for example the shapes of bio-structures, there are no variables directly available to parameterize the freestyle shape variations among them. Thus, an efficient and compact way to parameterize the subject-specific shapes are needed, which can be obtained by the statistical analysis of pre-existing shape examples [34].

Compared with subject-specific FE modeling and analysis, the Taylor expansion approach is more efficient, however, it is an approximation of the true FE solution and is generally not suitable to approximate highly non-linear structural performance functions. Thus which method to use depends on the specific applications.

1.1.3 Computing structural performance variation over the shape population

Nowadays, due to the ubiquitous availability of 3D sensors, it is more and more easier to have access to massive scanning data of different subjects. As a consequence, the population based structural analysis becomes popular, which allows us to study the variability of structural performances within the population. The inputs for the population based structural analysis are subject-specific shape models, the output is the probability distribution of the structural performance within the population.

The population based analysis is crucial in a variety of applications, for example: the structural reliability analysis and risk evaluation [31], the bio-structure fatigue analysis and implant design [9].

Currently, there are two major approaches to conduct structural analysis over a shape population: the subject-specific approach [12; 8] and the statistical model based approach [6; 35; 36]. Given the shape models of different subjects, the subject-specific approach conduct FE analysis on each individual subject shapes, from which the structural performance over the population is obtained. The statistical model based approach parameterizes the shape variations in the population by statistical shape modeling (SSM) [34], based on which the statistical finite element models are generated and Monte Carlo simulations [37; 38] are performed. The knowledge of the performance variation is then gained.

In the subject-specific approach, given a set of shape models of different subjects, researchers [8; 12] conduct FE analysis on each individual subject in the set to gain the knowledge of the structural performances over the population. For example, in [8] the

catastrophic ascending aorta aneurysm (AsAA) inflation and rupture was simulated in 27 patient-specific finite element models. The simulation results were used to guide the selection of meaningful metrics in risk evaluation. The subject-specific approach is direct and easy to implement. However, since from FE meshing to FE analysis, the subjects are modeled and analyzed independently from each other and there's no inter-subject correspondences, the analysis results are difficult to generalize (interpolate and extrapolate) and it is hard to reach statistically rigorous conclusions.

To overcome the limitations due to the drawbacks of the subject-specific approach, the statistical model based approach has been applied in structural analysis over shape populations [6; 35; 36]. In the statistical model based approach, the shape models of the subjects are not directly used for FE analyses, instead they are used to construct the statistical shape model (SSM) [34], which parameterizes the shape variations within the population. Then, by the statistical shape model, a large number of sampling shapes are randomly generated, on which the FE models are created and the corresponding FE analysis are performed (Monte Carlo simulations). At the end, the results are collected and analyzed.

The use of statistical shape modeling techniques to understand shape variations and its effect on biomechanical performance has been recently attempted in [6; 28; 35; 39; 36]. In [6], femoral neck fracture risk in a fall was studied within a population. The geometric differences between the high risk and low risk groups were evaluated. The uncertainties in both geometry and material properties were considered and were modeled by principal component analysis. The statistical shape modeling in [6] follows the general steps in [28]. Different from the typical statistical shape modeling

[34; 40] approaches, where the shapes are in the boundary representations, the shapes in [6; 28] are solid models with tetrahedral elements. In [36], the performance of a cementless osseointegrated tibial tray in a general population was studied using the finite element analysis. The variation of the tibial shape and internal loads are modeled by principal component analysis following the steps in [39]. In [35], the statistical shape and alignment model that accounts for the shape and alignment variabilities of knee joints was developed and applied in the analysis of knee joint mechanics. The review paper [9] gives a summary of the common approaches and recent developments in this field, where the statistical shape modeling acts as a tool that incorporates the variations in a shape population and parameterizes a shape with several parameters.

In the foregoing literature, Monte Carlo simulations was performed to investigate the structural performance variability caused by shape variations. That is by randomly generating the shape parameters according to the obtained probabilistic distributions, and obtaining a set of new shapes and new finite element mesh usually through mesh deformation. The finite element analysis was then performed on the generated finite element models and the results were collected, from which the distribution of the structural performances and the relationship between shape and function are studied.

Compared with the subject-specific approach, the statistical model based approach provides a more statistically rigorous and comprehensive way of studying the performance variation within a shape population. The drawback of this approach lies in its inefficiency since to obtain a result with reasonable accuracy, a large number of experiments (usually > 500) are needed and each experiment requires an expensive

finite element analysis. Thus a more efficient way to utilize the pre-existing shape data is needed.

1.2 Learning from the shape population

Our approach builds on statistical analysis of shape variations, also known as statistical shape modeling (SSM). SSM has emerged as a powerful tool [34] for shape learning from a population where statistical analysis of shape variations is conducted, typically through principal component analysis.

Statistical shape modeling was initially proposed and applied in the field of image segmentation in the 1990's. Some of the earliest works are done by T.F. Cootes and C.J. Taylor [41; 42]. In their work the image is segmented by evolving the contour of a Smart Snake in the image domain. Different from the Active Contour Models who deform the Snake freely, the Smart Snake is deformed within the linear shape space learned from the training shapes. The method is called the Active Shape Models.

As an important part of the Active Shape Models, the Point Distribution Model was introduced by T.F.Cootes in 1992 [43], which was later called the statistical shape model. In this work, a shape is represented by a set of labeled points. Given a set of training shapes $\{\mathbf{S}_1, \mathbf{S}_2, \cdots, \mathbf{S}_{n_s}\}$, the mean shape $\bar{\mathbf{S}}$ and the modes of shape variations (eigen-shapes) $\{\boldsymbol{\psi}_1, \boldsymbol{\psi}_2, \cdots, \boldsymbol{\psi}_{n_s-1}\}$ of the population are obtained by principal component analysis. A linear shape space is spanned by the mean shape

and the variation modes. An instance in the shape space is explicitly modeled by

$$\mathbf{S} = \overline{\mathbf{S}} + \sum_{i=1}^{n_s-1} \boldsymbol{\psi}_i w_i, \tag{1.1}$$

where $\mathbf{w} = [w_1, \cdots, w_{n_s-1}]^T$ are the shape parameters. The Smart Snake evolves in the shape space by adjusting its shape parameters $\mathbf{w}$. Compared with the Active Contour Models, where the Snake is usually a free curve, the Active Shape Models has much fewer shape parameters and has accommodated the model specificity in the sacrifice of variability. However, if we are only interested in a specific class of shapes, then the model specificity is just what we need. The smaller number of shape parameters in the Active Shape Models make the Snake evolve more robustly and efficiently.

Statistical shape modeling has later found its success in various fields including motion tracking [44] and parametric shape design [24; 13].

1.3 Proposed research

In this research, we present a statistical atlas based approach that incorporates statistical shape modeling in subject-specific shape reconstruction, finite element modeling and finite element analysis.

The statistical atlas contains three parts: a linear shape space spanned by the mean shape $\overline{\mathbf{S}}$ and eigen-shapes $\{\boldsymbol{\psi}_1, \boldsymbol{\psi}_2, \cdots, \boldsymbol{\psi}_{n_s-1}\}$, the FE mesh $\overline{\mathbf{T}}$ of the mean shape $\overline{\mathbf{S}}$, and the selected feature points $\mathbf{f}$ and dimensions $\mathbf{L}$.

The feature points and dimensions are selected on the mean shape by maximizing

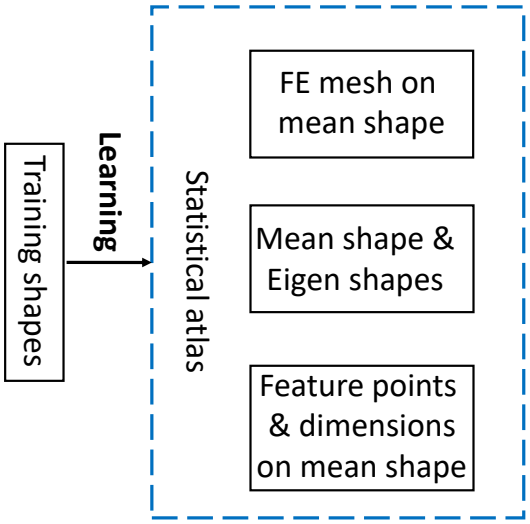

Figure 1.2: The statistical atlas.

the total variance they capture of the shape population. Then, given a subject (e.g. a person), the corresponding measurements are made and the subject specific shape model is reconstructed.

The FE mesh $\overline{\mathbf{T}}$ of the mean shape serves as the template mesh by which we either morph it to the given subject shape and conduct subject specific FE analysis or directly extrapolate the FE solution on it to the given subject shape through Taylor expansion.

The variances $\lambda_1, \cdots, \lambda_{n_s-1}$ in each variation modes $\boldsymbol{\psi}_1, \cdots, \boldsymbol{\psi}_{n_s-1}$ are obtained by principal component analysis. These variances tell us the amount of shapes variabilities in the population and are combined with Taylor expansion of the FE solution to obtain the structural performance variation across the population.

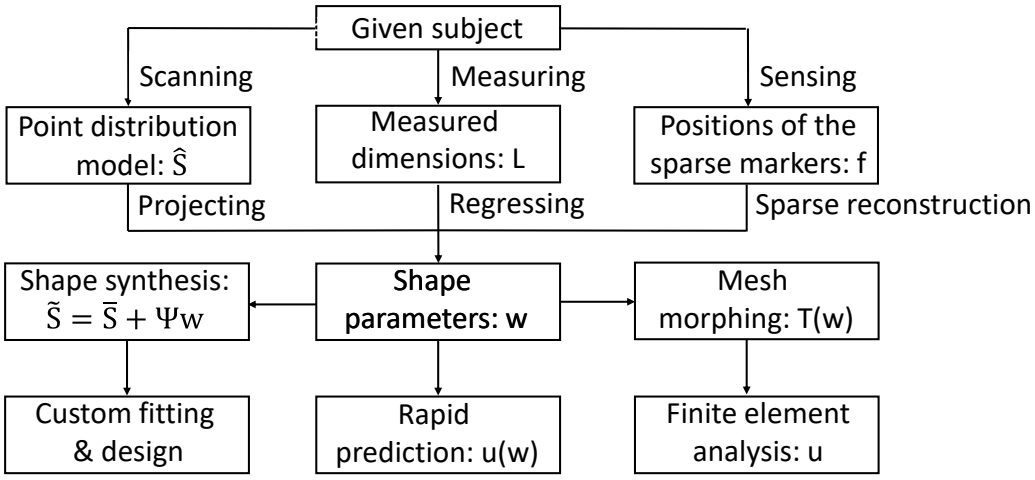

Figure 1.3: The proposed approach.

As shown in Figure 1.3 is a schematic diagram of the proposed approach. Given a subject, the first step is to obtain its corresponding shape parameters $\mathbf{w}$ in the linear shape space. With the obtained shape parameters $\mathbf{w}$, we could 1) synthesize a subject-specific shape model for the given subject based on which the custom fitting and interaction design can be performed; 2) efficiently predict the shape-specific structural performance by the Taylor expansion of the FE solution of the mean shape over the shape parameters: $\mathbf{u}(\mathbf{w}) = \mathbf{u}(\mathbf{0}) + \sum \frac{\partial \mathbf{u}}{\partial w_i}|_{\mathbf{0}} w_i$; 3) create subject-specific FE model by morphing the template FE mesh to the obtained shape parameters $\mathbf{T}(\mathbf{w})$ and conduct subject-specific FE analysis $\mathbf{u}(\mathbf{T})$. Compared with (2), method (3) is more accurate but is also more time consuming, which method to choose depends on the applications.

In the schematic diagram, three approaches are provided to obtain the shape

parameters **w** of the given subject.

In the first approach, the given subject is scanned to obtain a point-distribution model. However, the point-distribution model will not be in the same representation space with the instances of the statistical shape model. For example, the number of points will be different and they will not be in correspondence. We propose to automatically search the shape correspondence between the obtained point-distribution model and the instance of the statistical shape model by deforming the mean shape in the shape space. Based on the shape correspondence the point-distribution model is projected into the linear shape space to obtain the corresponding shape parameters.

In the second and third approaches, mappings from the feature points and the sizing dimensions to the shape parameters are built. Such mappings are obtained by regressing the shape parameters of the training shapes on the simulated measurements (e.g. positions of the feature points), since the locations of the feature points and sizing dimensions are well defined on the mean shape and thus on all the training shapes. Then, given the sizing dimensions or the positions of the feature points, the regression model outputs the corresponding shape parameters. The second and third approaches are more efficient than the first one, however, they are less accurate since the regression is not perfect and there will always be some unexplained variations, so which approach to use depends on the applications.

This dissertation research includes the following research contributions:

- Development of a statistical atlas based framework for custom design and analysis.

- Development of an approach that selects feature points and sizing dimensions by the total variance they capture of the shape population.

- Development of a statistical shape model based approach for automated shape registration and finite element modeling.

  In the literatures, the non-rigid registration [45; 16; 46] and free-form deformation [47; 48] are commonly used methods for shape registration. In this research we propose to search the shape correspondence by iteratively deforming the mean shape to subject-shape in the shape space. This is inspired by the Active Shape Model in image segmentation [49], The difference is that in [49], the shape evolves in the image domain and domain information (e.g. nearby pixel values, gradient information) is utilized to guide the deformation. However, our goal is to find the point correspondences between two shapes in 2D or 3D space, which is essentially a discrete problem. A direct adoption of the algorithm in [49] causes oscillations and fails to find the right correspondence.

- Development of a metric to evaluate the quality of the obtained shape correspondence.

  In this research we propose to use the multi-correlation of the normal vectors of two shapes to evaluate the obtained shape correspondence.

- Development of a Taylor expansion approach for predicting shape specific structural performance and structural performance variation over a shape population.

Taylor expansion is used in structural reliability analysis [31; 32; 50] to extrapolate the FE solution of the template structure to the structures with different design parameters. However, for the structures that are not readily parameterized (e.g. bio-structures with freestyle shape variations), direct application of this approach remains challenging. In this research, the design parameters (shape parameters) are learned by the statistical analysis of training shapes.

- Development of a multi-point Taylor expansion approach for the cases that the structural performance is highly nonlinear with respect to the shape parameters.

1.4 Organization of this dissertation

The remainder of this dissertation is organized as follows. Chapter 2 briefly overviews the process of statistical shape modeling. Chapter 3 demonstrates the total variance based feature points selection and its applications in sparse shape reconstruction and construction of new dimensions. Chapter 4 illustrates the automated shape registration and FE modeling for subject specific shapes by the statistical atlas and develops a metric to evaluate the quality of the obtained shape correspondences. Chapter 5 proposes a Taylor expansion approach for predicting the shape-specific structural performance and structural performance variation over a shape population. Chapter 6 summarizes this dissertation research.

2

Statistical shape modeling

In this work, statistical shape modeling is used to learn from a population of shapes. This section introduces the background of statistical shape modeling.

2.1 Shape population

Shape determines the appearance of an object. In 2D, shapes are often represented by boundary contours (Figure 2.1), in 3D, shapes are often represented by boundary surfaces. There are many other ways to represent a shape, for example, the volumetric representation adopted in [28], Fourier shape descriptors and medial axis [51]. In this dissertation, the shapes are in boundary representations such as polygonal contours (2D) and triangle meshes (3D).

Statistical shape modeling (SSM) [34] is used to captures the variations and the characteristics of a specific class of shapes through the analysis of the training shapes. In the analysis, each training shape is represented by a set of labeled points (Figure 2.2(a)). Through principal component analysis, the mean shape is found and the shape variations within the population are explicitly modeled. A linear shape space is then spanned by the mean shape and the modes of shape variations. Through statistical shape modeling, a shape instance is parameterized in the linear shape

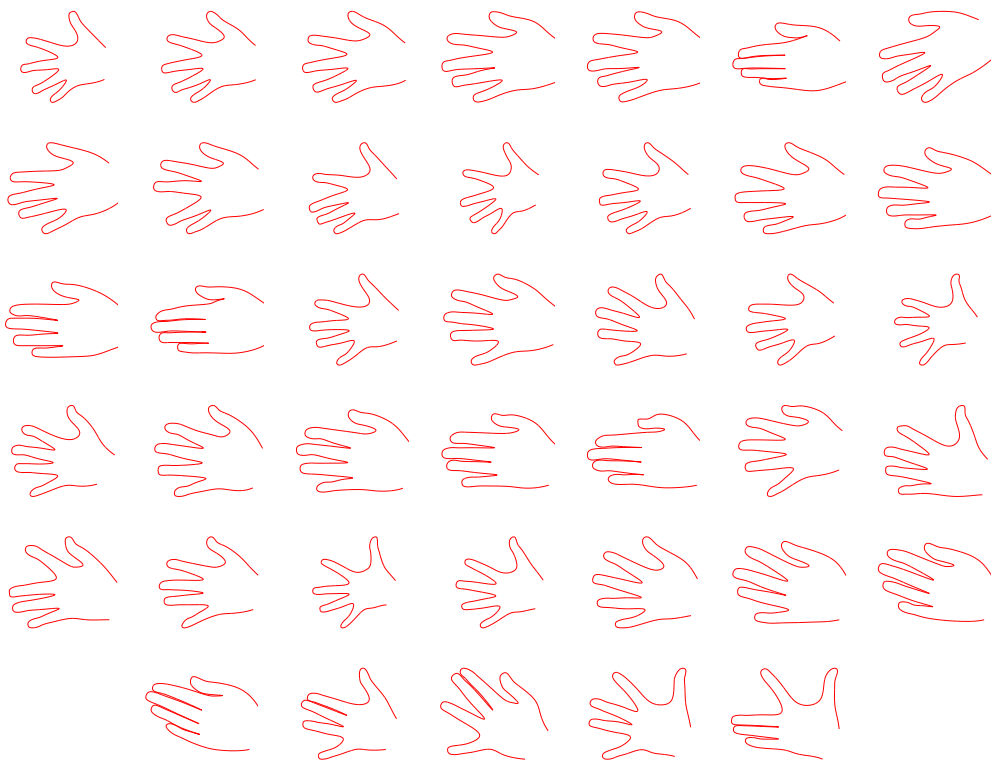

Figure 2.1: 40 hand shapes.

space by a few shape parameters, the probabilistic distribution of the shapes in space are modeled by the probabilistic distribution of the shape parameters. The mean shape of the population provides a statistical atlas, on which the template FE mesh is created and the corresponding feature points and sizing dimensions are defined.

Figure 2.1 shows 40 hand shapes with different sizes and poses that are collected from 4 different persons by [40]. The hand shapes are used as the training shapes for statistical shape modeling and in this chapter serve the goal of demonstrating the three steps of statistical shape modeling: shape registration, shape alignment, and shape modeling. Here, all the 40 shapes are included in the training set. However, in

practice, noises and errors are unavoidable and outliers among the training shapes may affect the quality of statistical shape modeling. To prevent the outliers, we check the shape parameters of each training shape after the statistical shape modeling and exclude the shapes that have shape parameters beyond four-standard deviations from the training set, and then we redo the statistical shape modeling with the cleaned training set.

2.2 Shape registration

Given the training set of n_s number of shapes $\mathcal{S} = \{\mathbf{S}_1, \mathbf{S}_2, \cdots, \mathbf{S}_{n_s}\}$, in order to correctly calculate the population mean and model the shape variations, correspondences between these shapes must be built. Based on such correspondences, we sample the same number of points on each shape and conduct statistical shape analysis.

The goal of shape registration is to find the correspondences between two shapes (Figure 2.2(b)), which associate a point in one shape to a point in another shape. Some well established shape registration methods include the rigid ICP (iterative closest point) algorithm [52], which aligns one shape to another shape through iterative rotations and translations. The non-rigid ICP algorithm [45; 53; 24] assigns an affine transformation matrix to each point and iteratively matching points in one set to the closest points in the other set. The free-form deformation based approach [46; 54; 47] embeds a shape in the underlying domain (e.g. a B-spline cube) and iteratively deforms the domain to match the points on another shape. Shape registra-

tion through reparameterization is demonstrated in [55; 56; 57], where the training shapes are represented by parametric surfaces (e.g. Bspline surfaces [57]) and are re-parameterized in the parametric domain to find the correct shape correspondences. However, the reparameterization approach requires surface parameterizations which has limited its applications to the shape registration of complex geometries and arbitrary topologies (e.g. aortas, tibia-fibulas).

In this research, the deformation based approach is used for shape registration. A reference shape $\mathbf{S}_{ref}$ is chosen from among the training shapes $\left\{\mathbf{S}_1^{raw}, \cdots, \mathbf{S}_{(n_s)}^{raw}\right\}$ and is deformed to each training shape to find the shape correspondences. Ideally, the reference shape should be close to the mean shape of the population. In practice, the mean shape is unknown, the reference shape is chosen by avoiding the extreme cases that it is far away from most of the other shapes in the population, since large shape deformations are usually not robust [58]. The shape registration process takes three steps: firstly, the reference shape is rigidly aligned (through rotations and translations) to the training shape by the rigid ICP algorithm [52]; Then the reference shape is further deformed to the training shape through iterative free-form deformations [46]; Finally, the vertices of the deformed reference shape are projected onto the training shape along the directions of normal vectors. Based on the obtained correspondences, the training shapes are re-sampled by the same number of points in correspondence:

$$\mathbf{S}_k = [\mathbf{v}_1^{(k)}, \cdots, \mathbf{v}_{n_b}^{(k)}]^t, \ k = 1, \cdots, n_s, \tag{2.1}$$

where $\mathbf{S}_k$ is the kth re-sampled training shape, n_b is the number of sampling points

on each shape, n_s is the number of training shapes, and $\mathbf{v}_i^{(k)} = [x_i^{(k)}, y_i^{(k)}, z_i^{(k)}]$ are the coordinates of the ith vertex on the kth shape.

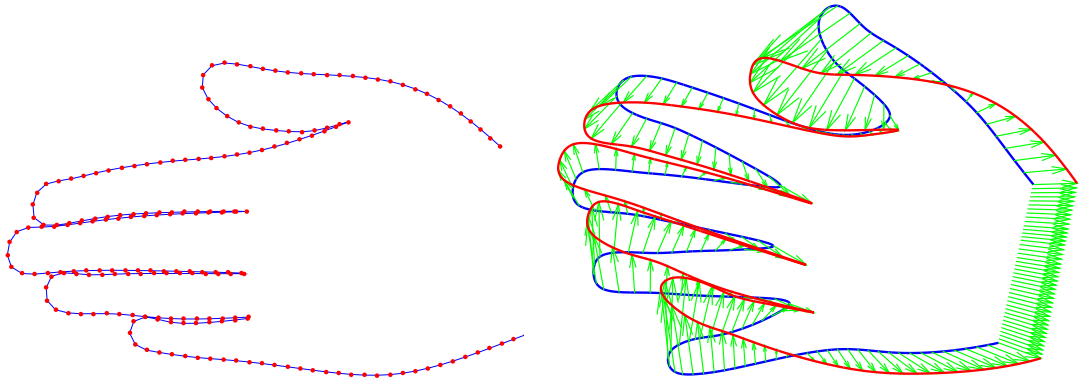

(a) The point distribution model (b) The shape correspondence

Figure 2.2: Shape registration and sampling.

The following subsections demonstrate the above processes of shape registration.

2.2.1 Shape alignment by rigid iterative closest point algorithm

Rigid ICP algorithm is proposed by Besl and McKay [52] for finding the rigid transformation between two point sets.

Here, among the n_s number of training shapes, one shape is chosen as the reference shape, note it as $\mathbf{S}_r$. It is aligned to the other shapes $\mathbf{S}_k^{raw},\ k = 1, \cdots, n_s$ in the training set respectively by the rigid ICP algorithm. For simplicity, let's denote the reference shape $\mathbf{S}_r = \left\{\mathbf{v}_1^{(r)}, \mathbf{v}_2^{(r)}, \cdots, \mathbf{v}_{N_1}^{(r)}\right\}$, and the corresponding training shape $\mathbf{S}_t = \left\{\mathbf{v}_1^{(t)}, \mathbf{v}_2^{(t)}, \cdots, \mathbf{v}_{N_2}^{(t)}\right\}$. The goal of rigid alignment is to find the optimal rotation $\mathbf{R}$ and translation $\mathbf{T}$ such that the squared sum of the distances of the points in $\mathbf{S}_r$

to $\mathbf{S}_t$ is minimized:

$$\min_{\mathbf{R},\mathbf{T}} \sum_{i=1}^{N_1} d(\mathbf{R}\mathbf{v}_i^{(r)} + \mathbf{T}, \mathbf{S}_t)^2, \tag{2.2}$$

where $d(\mathbf{R}\mathbf{v}_i^{(r)} + \mathbf{T}, \mathbf{S}_t)$ is the distance of the transformed point $\mathbf{R}\mathbf{v}_i^{(r)} + \mathbf{T}$ to $\mathbf{S}_t$. When $\mathbf{S}_t$ is a point set, $d(\mathbf{R}\mathbf{v}_i^{(r)} + \mathbf{T}, \mathbf{S}_t)$ is the distance of $\mathbf{R}\mathbf{v}_i^{(r)} + \mathbf{T}$ to its closest point in $\mathbf{S}_t$. The optimization problem in equation (2.2) is a discrete problem and is solved by the iterative closest point algorithm [52]:

1. Firstly, the closest points of $\mathbf{S}_r = \left\{\mathbf{v}_1^{(r)}, \mathbf{v}_2^{(r)} \cdots, \mathbf{v}_{N_1}^{(r)}\right\}$ in $\mathbf{S}_t$ are found: $\mathbf{S}_t^c = \left\{\mathbf{v}_1^{(t,c)}, \mathbf{v}_2^{(t,c)} \cdots, \mathbf{v}_{N_1}^{(t,c)}\right\}$.

2. Then the optimal translation $\mathbf{T}$ and rotation $\mathbf{R}$ are found for:

$$\min_{\mathbf{R},\mathbf{T}} \sum_{i=1}^{N_1} (\mathbf{R}\mathbf{v}_i^{(r)} + \mathbf{T} - \mathbf{v}_i^{(t,c)})^T (\mathbf{R}\mathbf{v}_i^{(r)} + \mathbf{T} - \mathbf{v}_i^{(t,c)}),$$

   which has analytical solution as in [52].

3. If R and T converge, then stop; else go to step 1.

For more details of the rigid ICP algorithm, please refer to paper [52].

The rigid ICP algorithm is guaranteed to converge to a local minimum [52] and is used here to align the reference shape to the corresponding training shape so to reduce the amount of deformation in the following shape registration step. However, in our 3D experiments we do observed several cases that the rigid ICP algorithm has converged to bad local minimums (e.g. the head of a femur is aligned to the bottom

part of another femur). In such situations manually chosen landmarks are used to guide the alignment:

$$\min_{\mathbf{R},\mathbf{T}} \sum_{i=1}^{N_1} d(\mathbf{R}\mathbf{v}_i^{(r)} + \mathbf{T}, \mathbf{S}_t)^2 + \sum_{j=1}^{l} (\mathbf{R}\bar{\mathbf{v}}_j^{(r)} + \mathbf{T} - \bar{\mathbf{v}_j}^{(t)})^T (\mathbf{R}\bar{\mathbf{v}}_j^{(r)} + \mathbf{T} - \bar{\mathbf{v}_j}^{(t)}),$$

where $\{(\bar{\mathbf{v}}_1^{(r)}, \bar{\mathbf{v}}_1^{(t)}), \cdots, (\bar{\mathbf{v}}_l^{(r)}, \bar{\mathbf{v}}_l^{(t)})\}$ are the pairs of landmarks on $\mathbf{S}_r$ and $\mathbf{S}_t$, the second term in (2.3) is used to penalize the landmark mismatches.

2.2.2 Pairwise shape registration by free-form deformation

Having aligned the reference shape to the corresponding training shape, the iterative free-form deformation (FFD) is used to find the correspondence between the reference shape and the training shape. Our approach is simplified from the approach in [46], where an automated approach for shape registration by iterative free-form deformations and fuzzy correspondences is proposed. Since in this dissertation, our goal is to stably obtain good quality shape correspondences and apply that in statistical shape analysis and the later custom design and analysis, a more conservative way of shape registration is chosen. We drop the part of fuzzy correspondences in [46] and guide the registration process by penalizing the mismatch error of the pairs of manually specified landmarks as in the non-rigid ICP algorithm [45].

In free-form deformation (FFD) [59], a shape $\mathbf{S} \subset \mathcal{R}^d$ in d dimensional Euclidean space $d = 2, 3$ is morphed by deforming its underlying domain $\Omega \subset \mathcal{R}^d$. Here we use

the B-spline FFD:

$$\mathbf{f}(\mathbf{u}) = \sum_{\mathbf{i}\in\mathcal{I}} \mathbf{P}_\mathbf{i} B_\mathbf{i}(\mathbf{u}),\ \ \mathbf{u} \in [0,1]^d, \tag{2.3}$$

$\{\mathbf{P}_\mathbf{i} : \mathbf{i} \in \mathcal{I}\}$ is the set of control points, $\{B_\mathbf{i} : \mathbf{i} \in \mathcal{I}\}$ is the set of B-bases, $\mathbf{u}$ is the parameter value.

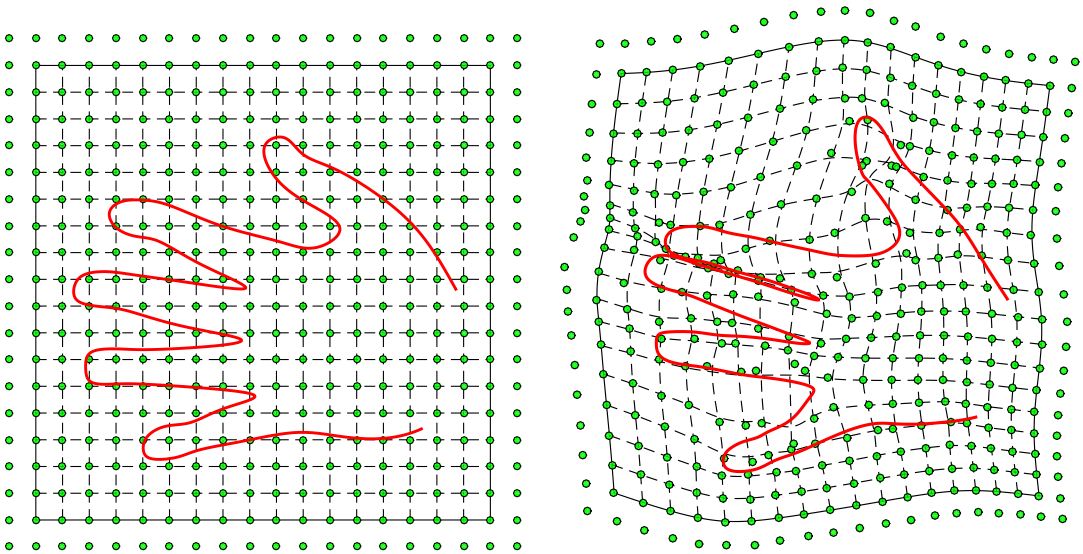

(a) Before deformation (b) After deformation

Figure 2.3: Deformation of a B-spline patch and the embedded shape.

Figure 2.3 shows the free-form deformation of a hand shape which is embedded in a B-spline patch. The green points in the figure are the B-spline control points.

As shown by Figure 2.4(a), in this work, the shapes are represented by discrete points. The goal of shape registration is to find the positions of the control points $\{\mathbf{P}_\mathbf{i}\}$ and the point-to-point shape correspondences $c : \mathbf{v}_i^r \rightarrow \mathbf{v}_j^t$ such that the below

equation is minimized:

$$\min_{\{\mathbf{P_i}\},c} E_{deviation} + \alpha E_{smooth} + \beta E_{landmarks}. \tag{2.4}$$

The first term in (2.4)

$$E_{deviation} = \sum_{j=1}^{N_1} \|\mathbf{f}(\mathbf{v}_j^{(r)}) - \mathbf{v}_j^{(t,c)}\|^2,$$

is the sum of square of deviations between the deformed reference shape $\mathbf{f}(\mathbf{S}_r)$ and the target shape $\mathbf{S}_t$, $\mathbf{f}$ is the deformation field as defined in (2.3), and $\mathbf{v}_j^{(t,c)}$ is the closest point of $\mathbf{v}_j^{(r)}$ in $\mathbf{S}_t$.

The second term in (2.4)

$$E_{smooth} = \int_\Omega \|(\sum_{i=1}^{d} \frac{\partial}{\partial x_i})^2 \mathbf{f}\|^2 d\mathbf{x},$$

is the smoothing term and penalizes large deformations. The smoothing coefficient α in (2.4) is chosen to be large at the initial deformation steps and reduced gradually.

To guide the deformation, we manually assign a set of landmarks to each shape with presumed correspondences. The third term in (2.4)

$$E_{landmarks} = \sum_{i=1}^{l} \|\mathbf{f}(\bar{\mathbf{v}}_i^{(r)}) - \bar{\mathbf{v}}_i^{(t)}\|^2,$$

captures the mismatch error of the landmarks, where $\{(\bar{\mathbf{v}}_1^{(r)}, \bar{\mathbf{v}}_1^{(t)}), \cdots, (\bar{\mathbf{v}}_l^{(r)}, \bar{\mathbf{v}}_l^{(t)})\}$ are the pairs of landmarks on $\mathbf{S}_r$ and $\mathbf{S}_t$. The landmark weight β in (2.4) is decided so

that $\alpha E_{deviation}$ and $\beta E_{landmarks}$ are in the same order of magnitude.

Formula (2.4) is a formulation that has been widely used in the pairwise shape registrations, while the shape deformation techniques applied are different. In [46; 54] Bspline filed is used for free-form deformation. In [47] the Thin-spline is adopted. In [45; 53; 24] affine transformation matrices are assigned to each vertex in the deformation. Similarly as in the rigid ICP algorithm, iterative optimization approach [45; 48; 60] is used to minimize (2.4):

- For $\alpha = N, N/2, N/4, \cdots, n$:

  1. The closest points of $\mathbf{S}_r = \left\{\mathbf{v}_1^{(r)}, \mathbf{v}_2^{(r)} \cdots, \mathbf{v}_{N_1}^{(r)}\right\}$ in $\mathbf{S}_t$ are found: $\mathbf{S}_t^c = \left\{\mathbf{v}_1^{(t,c)}, \mathbf{v}_2^{(t,c)} \cdots, \mathbf{v}_{N_1}^{(t,c)}\right\}$.
  2. The positions of the control points $\{\mathbf{P_i}\}$ that minimizes (2.4) are solved. This equals solving a set of linear equations since (2.4) is a quadratic formula.
  3. If $\{\mathbf{P_i}\}$ converge, then stop; else go to step 1.

In the above algorithm, α is a very big number N initially so only global deformations are allowed. As the reference shape gets deformed closer to the training shape, α is decreased so to allow finer local shape deformations.

With fixed values of α and γ, equation (2.4) is guaranteed to converge to a local minimum, since each step reduces the total energy function in (2.4). The correspondence is updated by the closest points, so $E_{deviation}$ is reduced by step 1 while E_{smooth} and $E_{landmarks}$ remain the same. Based on the obtained correspondence,

in step 2 the optimal positions of the control points $\{\mathbf{P_i}\}$ are solved so E is again reduced.

After we have found the desired deformation $\mathbf{f}$, we project the deformed reference shape $\mathbf{f}(\mathbf{S}_r)$ onto the target shape $\mathbf{S}_t$ along the vertex normal and establish a point-wise correspondence between $\mathbf{S}_r$ and $\mathbf{S}_t$. The normal on the vertex is calculated by averaging the normals of its surrounding elements (line segments in 2D and triangle facets in 3D).

In Figure 2.4(a) we show two shapes with landmarks, in Figure 2.4(b) we show the process of free form deformation, and in Figure 2.4(c) is the projection.

2.3 Shape alignment

After the shape registration, the training shapes are sampled by the same number of points in correspondence as in equation (2.1). Generalized Procrustes analysis [61] is conducted to align the registered shapes $\{\mathbf{S}_1, \cdots, \mathbf{S}_{n_s}\}$ to the same coordinate frame and to eliminate the effects of translation, rotation and scaling

$$\min_{\{\mathbf{R}_k, \mathbf{T}_k, s_k\}} \quad \sum_{k=1}^{n_s} (s_k \mathbf{S}_{(k)} \mathbf{R}_k + \mathbf{T}_k - \overline{\mathbf{S}})^2, \tag{2.5}$$

where s_k is the scaling coefficient of the kth shape, $\mathbf{R}_k$ the rotation matrix, and $\mathbf{T}_k$ the translation. We have the mean shape

$$\overline{\mathbf{S}} = \frac{1}{n_s} \sum_{i=1}^{n_s} (s_k \mathbf{S}_{(k)} \mathbf{R}_k + \mathbf{T}_k). \tag{2.6}$$

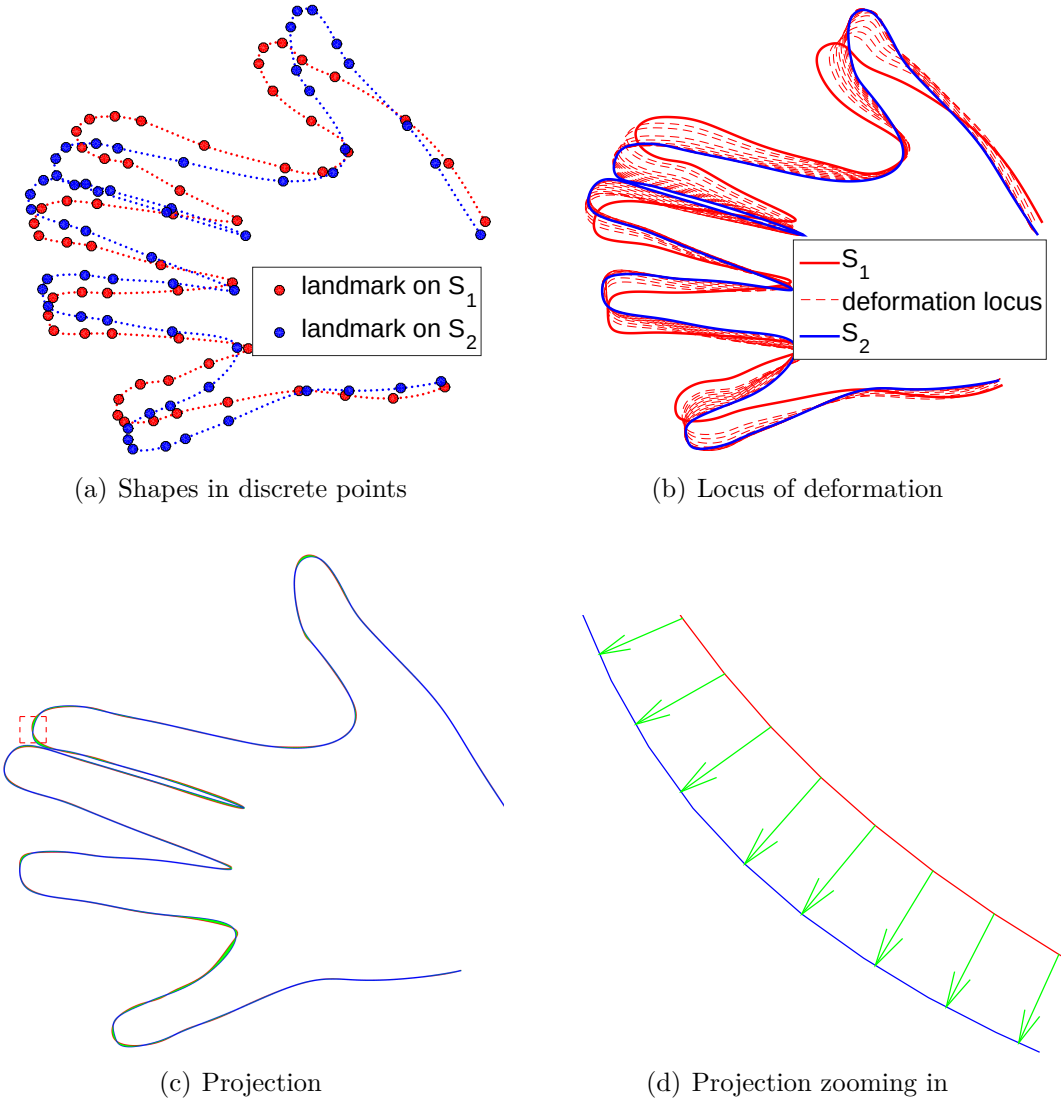

(a) Shapes in discrete points

(b) Locus of deformation

(c) Projection

(d) Projection zooming in

Figure 2.4: Pairwise registration by free-form deformation: the template shape is in red, the target shape is in blue.

The mean shape is set to the unit size trace$(\overline{\mathbf{S}}^t\overline{\mathbf{S}}) = 1$, its centroid is set to the origin and its orientations are fixed in the coordinate frame, so that the optimization (2.5) is well defined. Figure 2.5 shows the results of the generalized Procrustes analysis of 40 hand shapes.

(a) Input shapes (b) Aligned shapes (c) Mean shape

Figure 2.5: By conducting the generalized Procrustes analysis, we obtain a set of aligned shapes and the mean shape.

2.4 Principal component analysis

With the training shapes aligned in the same coordinate frame, principal component analysis is conducted to model the shape variations in the population, where each shape is treated as a vector in the $\mathbb{R}^{n_b d}$ space, n_b is the number of sampling points on each shape, and d is the dimension. The mean shape of the population is

$$\overline{\mathbf{S}} = \frac{1}{n_s}\sum_{k=1}^{n_s}\mathbf{S}_k, \tag{2.7}$$

the shape covariance matrix is

$$\mathbf{\Sigma} = \frac{1}{n_s - 1}\mathbf{\Phi}\mathbf{\Phi}^T, \tag{2.8}$$

where $\mathbf{\Phi} = [\mathbf{S}_1 - \overline{\mathbf{S}}, \cdots, \mathbf{S}_{n_s} - \overline{\mathbf{S}}]$. Just as all the covariance matrices do, the shape covariance matrix $\mathbf{\Sigma}$ describes the pattern and range of variations deviate from the population mean $\overline{\mathbf{S}}$. Through eigen-decomposition, we have

$$\mathbf{\Sigma}\boldsymbol{\psi}_k = \lambda_k \boldsymbol{\psi}_k, \ k = 1, \cdots, n_s - 1, \tag{2.9}$$

where $\boldsymbol{\psi}_1, \cdots, \boldsymbol{\psi}_{n_s-1}$ are the eigenvectors of the covariance matrix $\mathbf{\Sigma}$ and are orthonormal to each other. The amount of shape variations is maximized along the first eigenvector, and is maximized along the second eigenvector with the components along the first eigenvector removed and so on. $\lambda_1, \cdots, \lambda_{n_s-1}$ are the eigenvalues and correspond to the amount of shape variances along these eigenvectors, they are ordered from large to small.

The obtained mean shape $\overline{\mathbf{S}}$ and eigenvectors (eigen-shapes) $\boldsymbol{\psi}_1, \cdots, \boldsymbol{\psi}_{n_s-1}$ span a linear shape space Θ. An instance in the shape space can be represented by:

$$\mathbf{S} = \overline{\mathbf{S}} + \sum_{k=1}^{n_s-1} w_k \boldsymbol{\psi}_k, \tag{2.10}$$

where $w_1 \cdots w_{n_s-1}$ are the weights on each eigen-shapes and are called the shape parameters. The shape parameters uniquely determine an instance in the shape space.

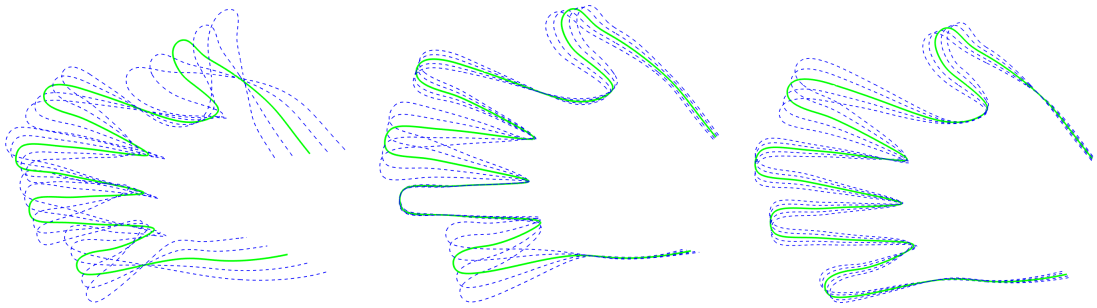

(a) The first mode (b) The second mode (c) The third mode

Figure 2.6: Principal component analysis: (a) the first variation mode: $\overline{\mathbf{S}} + w_1\boldsymbol{\psi}_1$, $w_1 \in [-2\sigma_1, 2\sigma_1]$; (b) the second variation mode: $\overline{\mathbf{S}} + w_2\boldsymbol{\psi}_2$, $w_2 \in [-2\sigma_2, 2\sigma_2]$; (c) the third variation mode: $\overline{\mathbf{S}} + w_3\boldsymbol{\psi}_3$, $w_3 \in [-2\sigma_3, 2\sigma_3]$.

In Figure 2.6 we show the first three eigen-shapes obtained by the principal component analysis of 40 hand shapes. As a result of principal component analysis, we have 39 eigen-shapes. However, due to the dimensionality reduction of principal component analysis, the first several eigen-shapes capture most of the shape variances in the population, thus only a small number of eigen-shapes need to be incorporated in the statistical shape model. So a compact representation of the shape population can be obtained and the potential noises in the last several eigen-shapes with close to zero eigenvalues are avoided. Such noises are usually come from the errors in image segmentation, shape reconstruction and surface rectification.

A truncated statistical shape model would be

$$\mathbf{S} = \overline{\mathbf{S}} + \sum_{k=1}^{m} w_k\boldsymbol{\psi}_k + \boldsymbol{\epsilon}, \tag{2.11}$$

m is the number of modes chosen and can be determined, e.g. from $\sum_{k=1}^{m} \lambda_k / \sum_{k=1}^{n_s-1} \lambda_k \geq$

99%, which means that the first m modes should capture more than 99% of the total shape variances in the training set, where $\boldsymbol{\epsilon}$ is the random vector that captures the remaining shape variances in the population.

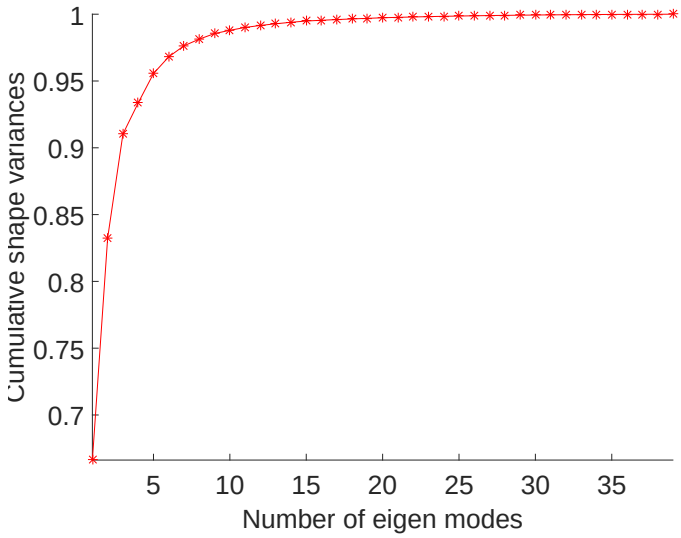

Figure 2.7: The cumulative variances of the shape population captured by the increasing number of eigen-shapes.

Figure 2.7 shows the cumulative variances captured by the increasing number of eigen-shapes. The first 8 eigen-shapes have captured 98.14% of the shape variances in the population and the first 11 eigen-shapes have captured 99.01% of the shape variances in the population. The 40 hand shapes are come from [40] and are used here to illustrate the statistical shape modeling procedure. In our late chapters more practical 3D shape data such human body shape models, rabbit tibia models will be used.

2.5 Probabilistic distributions of the shapes

For a training shape $\mathbf{S}_i$, its shape parameters can be obtained by projecting it into the shape space:

$$w_{i,k} = (\mathbf{S}_i - \overline{\mathbf{S}})^T \boldsymbol{\psi}_k, k = 1, \cdots, n_s - 1, \tag{2.12}$$

where $w_{i,k}$ means the kth shape parameter for the ith shape.

Thus the probabilistic distribution of the shapes in space can be modeled by the distributions of the shape parameters. Assuming that the shapes are normally distributed, the probability density of the vector of the shape parameters $\mathbf{w}$ is:

$$p(\mathbf{w}) = \Pi_{k=1}^{m} (2\pi\sigma_k^2)^{-\frac{1}{2}} e^{-\frac{w_k^2}{2\sigma_k^2}}, \tag{2.13}$$

where $\sigma_k = \sqrt{\lambda_k}$ is the standard deviation along the kth mode, and λ_k is the kth eigenvalue of the principal component analysis. Noted that as a result of the principal component analysis, the shape parameters are uncorrelated with each other. While most researches exploit the synthesis power of the statistical shape model and focus on shape synthesis by the mean shape and the eigen-shapes, we view equations (2.11) and (2.13) a probabilistic description of the shape distributions and build our methods on it. In each of the later chapters there is a section briefly introduces the statistical shape modeling to make them self contained.

3

Total variance based feature point selection and applications

Constructing faithful subject-specific shape model for a given subject is the first step to custom design and analysis. However, the process of obtaining neat subject shape models from images or scanned point clouds is tedious and error-prone. The sparse shape reconstruction and parametric shape model are used to bypass this process. The inputs are the positions of the sparse markers obtained by sensors or the measurements of sizing dimensions. The output is the complete shape model reconstructed for the subject. The challenge is where to put the markers and what dimensions to choose so we can have faithful reconstructions.

Feature points are the points that capture the geometric characteristics of an object. They usually have certain anatomical significance or geometric meaning. The selection of feature points is a fundamental problem with various applications. For example, they are used as the marker points in sparse shape reconstruction and are used as the reference points for generating meaningful sizing dimensions in the parametric shape design. The selection of feature points have many more applications including shape registration, cross-parameterization, and shape approximation, which

will not be enumerated here.

In the literature, feature point is selected on a single shape by its differential property or saliency. The population information of similar shapes are not considered. Being carefully chosen, they can represent the corresponding shape well. However, the variations between different shapes within the population are overlooked.

In this work, through statistical shape modeling, we evaluate the feature points by the amount of variance they capture of the shape population, which leads to an algorithm that sequentially selects and ranks the feature points. In this way, the selected feature points explicitly incorporate the population information of the shapes. Then, we demonstrate how the proposed feature point selection approach can be incorporated in the applications of sparse shape reconstruction, construction of new dimensions and shape classification through sparse measurements.

The numerical examples validate the effectiveness and efficiency of the proposed approach.

3.1 Method overview

The proposed feature points selection approach takes two steps as shown in Figure 3.1: 1) statistical shape modeling to learn the shape variations in the population; 2) selecting the feature points by the amount of variance they capture of the shape population.

Given the training shapes, firstly, statistical shape modeling [40] is conducted to learn the mean shape $\mathbf{S}$ and the variation modes $\mathbf{\Psi} = [\boldsymbol{\psi}_1, \boldsymbol{\psi}_2, \cdots, \boldsymbol{\psi}_{n_s-1}]$ of the

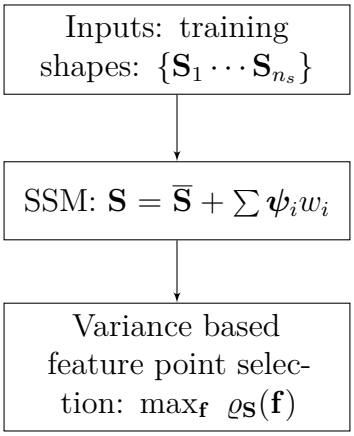

Figure 3.1: Total variance based feature points selection.

shape population. The mean shape and the variation modes span a linear shape space, any instance in the shape space can be represented as the linear combination of the mean shape and the variation modes as shown in Figure 3.1. The weights $\mathbf{w} = [w_1, w_2, \cdots, w_{n_s-1}]$ of the variations modes are called the shape parameters, whose probability distribution $p(\mathbf{w})$ is learned from statistical shape modeling of the shape population. Since the variation modes are unit vectors, the total variance of the shape population equals the total variance of the shape parameters $\text{var}(\mathbf{w})_{p(\mathbf{w})}$. The foregoing notation means the variance of $\mathbf{w}$ under the distribution of $p(\mathbf{w})$.

Then, given the vector of feature points $\mathbf{f} = \left\{\mathbf{v}_{i_1} \cdots \mathbf{v}_{i_{n_f}}\right\}$, the conditional probability distribution of the shape parameters $p(\mathbf{w}|\mathbf{f})$ is calculated, the corresponding conditional variance $\text{var}(\mathbf{w})_{p(\mathbf{w}|\mathbf{f})}$ is obtained. The difference between the total variance and the conditional variance is the amount of variance of the shape parameters explained (captured) by the feature points. The percentage of the total variance in

the shape population captured by the feature points is then:

$$\varrho_{\mathbf{w}}(\mathbf{f}) = \frac{\mathrm{var}(\mathbf{w})_{p(\mathbf{w})} - \mathrm{var}(\mathbf{w})_{p(\mathbf{w}|\mathbf{f})}}{\mathrm{var}(\mathbf{w})_{p(\mathbf{w})}}. \tag{3.1}$$

Thus, from the population perspective, the best set of feature points is the set that captures the highest percentage variance (3.1) of the shape population. This leads to a forward selection algorithm that sequentially selects and ranks the feature points.

Then, the selected feature points are incorporated in the applications of: 1) sparse shape reconstruction, 2) construction and selection of new dimensions, and 3) shape classification by sparse measurements.

3.2 Statistical shape modeling

Statistical shape modeling is used to obtain the variation modes of the shape population and the variances along the variation modes.

Given the set of training shapes $\{\mathbf{S}_1, \cdots, \mathbf{S}_{n_s}\}$ registered by the free-form deformation approach and re-sampled by the same number of points in correspondences:

$$\mathbf{S}_k = [\mathbf{v}_1^{(k)}, \cdots, \mathbf{v}_{n_v}^{(k)}]^T, \ k = 1, \cdots, n_s. \tag{3.2}$$

Generalized Procrustes analysis [61] is used to align them in the same coordinate frame and then principal component analysis is applied to obtain the mean shape $\overline{\mathbf{S}}$ and eigen-shapes $\mathbf{\Psi} = [\boldsymbol{\psi}_1, \cdots, \boldsymbol{\psi}_{n_s-1}]$ of the population. The first m number of eigen-shapes are chosen such that 99% of the variances in the shape population is

captured $\sum_{k=1}^{m} \lambda_k / \sum_{k=1}^{n_s-1} \lambda_k \geq 99\%$. The mean shape and the first m eigen-shapes give a compact representation of the shape population:

$$\mathbf{S} = \overline{\mathbf{S}} + \sum_{k=1}^{m} w_k \boldsymbol{\psi}_k + \boldsymbol{\epsilon}, \tag{3.3}$$

where $\mathbf{w} = [w_1, \cdots, w_m]^T$ are the shape parameters, $\boldsymbol{\epsilon}$ is the random vector that captures the remaining shape variances in the population.

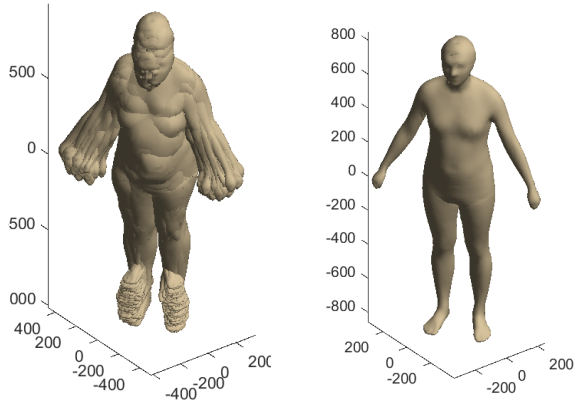

(a) Training Shapes (b) Mean shape

Figure 3.2: Shape population of human body: (a) training shapes in the same coordinate frame, (b) the mean shape.

Figure 3.2 shows the training shapes of the human body model and the corresponding mean shape. Figure 3.2 shows the first three eigen-shapes of the population. The first eigen-shape is related to the change in height, the second eigen-shape is related to the change in width, and the third eigen-shape is related to some local shape changes.

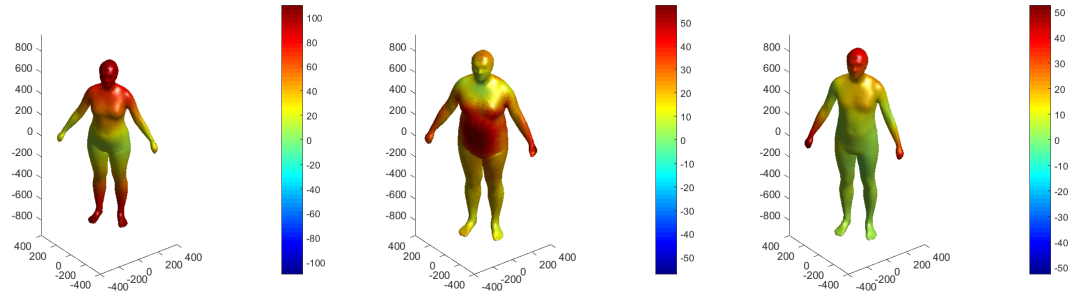

(a) +Mode 1 (b) +Mode 2 (c) +Mode 3

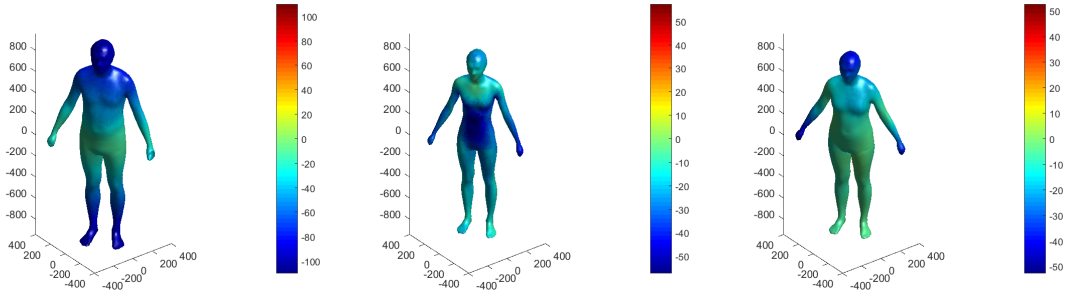

(d) -Mode 1: height (e) -Mode 2: width (f) -Mode 3: body shape

Figure 3.3: The first three eigen-shapes. The units are in mini-meters. The color on the surface shows the amount of deviation from the mean shape.

Assuming that the shapes are normally distributed, the probability density of the vector of the shape parameters $\mathbf{w}$ is:

$$p(\mathbf{w}) = |2\pi\Lambda|^{-\frac{1}{2}} e^{-\frac{1}{2}\mathbf{w}^T\Lambda^{-1}\mathbf{w}}, \ , \Lambda = \text{diag}(\lambda_1, \cdots, \lambda_m) \tag{3.4}$$

where λ_i is the variance of shape parameter w_i and is the ith largest eigenvalue of the shape covariance matrix (2.8). The cumulative variance of the shape population captured by the increasing number of eigen-modes is shown in Figure 3.5.

Figure 3.4 shows the distributions of the first six shape parameters obtained by

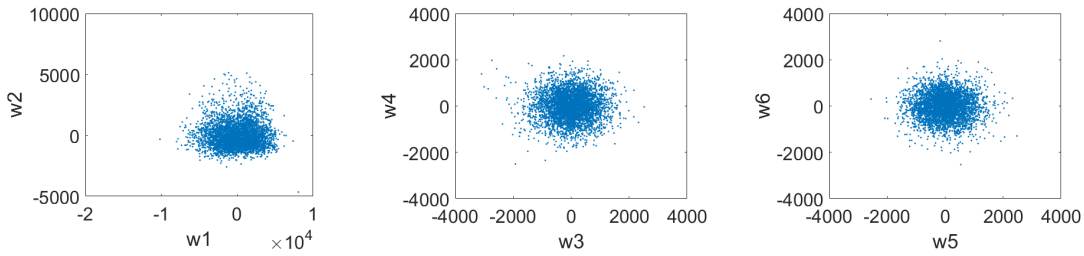

Figure 3.4: The distributions of the shape parameters.

projecting the shapes on the eigen-modes by equation (2.12). It can be seen that the distributions are similar to discs with denser points in the center and sparser points at the outer area. Thus the normal distribution would be a good approximation to the true distribution.

While most researches exploit the synthesis power of the statistical shape model and focus on shape synthesis by the mean shape and the eigen-shapes, we view equations (3.3) and (3.4) as the probabilistic description of the shape space and build our method on it.

3.3 Feature point identification

Through statistical shape modeling, the eigen-modes of the shape population are learned and are ranked by the amount of percentage variance they captured of the shape population, as shown in Figure 3.5(a). Since the goal of feature points selection is to capture as much information as possible of the shape population, in this section, the feature points are selected and ranked by the amount of percentage variance they capture of the shape population, as shown in Figure 3.5(b).

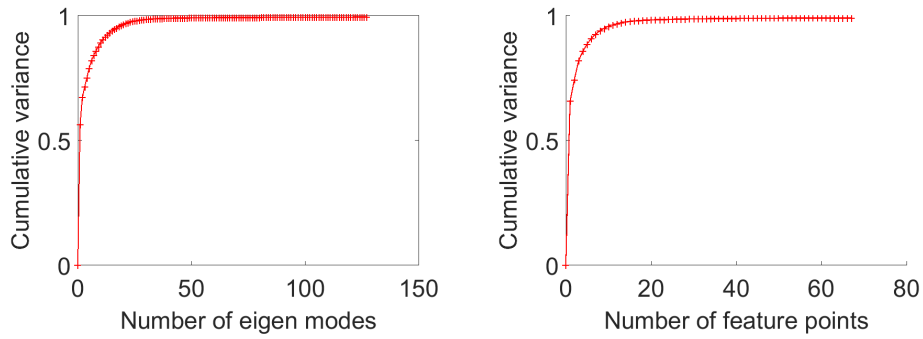

(a) Cumulative variance (b) Cumulative variance

Figure 3.5: The percentage of variance of the training shapes captured by the increasing number of (a) eigenvectors; (b) feature points.

With the statistical shape model (3.3), a shape in the population is parameterized by a few shape parameters $\{w_1, \cdots, w_m\}$, and the major amount of variance (i.e. 99.5%) in the population is captured by the variances of the shape parameters $\{\lambda_1, \cdots, \lambda_m\}$, which are the eigenvalues of the shape covariance matrix $\mathbf{\Sigma}$. The remaining variance is captured by the residual vector $\boldsymbol{\epsilon}$ in (3.3). Since it is not meaningful to capture the variance in the residual vector, the selected feature points are targeted to capture as much variance in the shape parameters as possible.

The inputs of the feature points selection is the statistical shape model, and the number of points to be selected: n_f. The outputs are the vertex indices of the selected feature points $\mathbb{I} = \left\{i_1, \cdots, i_{n_f}\right\} \subset \{1, \cdots, n_v\}$, where n_v is the total number of vertices. The feature points on the shape vectors can then be sampled by the indices, for example, the vectors of feature points on the n_s number of training shapes

are:

$$\mathbf{F} = [\mathbf{f}_1, \mathbf{f}_2, \cdots, \mathbf{f}_{n_s}], \tag{3.5}$$

where $\mathbf{f}_k = [\mathbf{v}_{i_1}^{(k)}, \mathbf{v}_{i2}^{(k)}, \cdots, \mathbf{v}_{in_f}^{(k)}]^T$ is the vector of feature points sampled on the kth training shape, which is abbreviated as the feature vector in the latter context.

Given the indices of the feature points, equation (3.3) can be partitioned into

$$\mathbf{f} = \overline{\mathbf{S}}_f + \mathbf{\Psi}_f \mathbf{w} + \boldsymbol{\epsilon}_f, \tag{3.6}$$

where $\mathbf{f}$ is the corresponding part of the shape vector $\mathbf{S}$, $\overline{\mathbf{S}}_f$ is the corresponding part of the mean shape $\overline{\mathbf{S}}$, $\mathbf{\Psi}_f$ is the corresponding part of the matrix of eigenvectors $\mathbf{\Psi} = [\boldsymbol{\psi}_1 \cdots \boldsymbol{\psi}_m]$, and $\boldsymbol{\epsilon}_f$ is the corresponding part of the residual vector $\boldsymbol{\epsilon}$.

The covariance matrix of the shape parameters are known from the principal component analysis $\Lambda = \mathrm{diag}(\lambda_1, \cdots, \lambda_m)$. The covariance matrix of the residual vector can be estimated by the residual variance $\sum_{k=m+1}^{n_s-1} \lambda_k$ of the remaining eigen-modes and the resolution and quality of image segmentation:

$$\begin{aligned} \mathrm{Cov}(\boldsymbol{\epsilon}_f) &= \left(\sum_{k=m+1}^{n_s-1} \frac{\lambda_k}{3n_f} + c \right) \mathbf{I} \\ &= \epsilon \mathbf{I}, \end{aligned} \tag{3.7}$$

where $\mathbf{I}$ is the identity matrix. The first component in $\mathrm{Cov}(\boldsymbol{\epsilon}_f)$ accounts for the residual variance of the remaining eigen-modes, the second component accounts for the noises from, for example, the image segmentation, shape extraction, and surface

rectification.

Since the covariance matrices of the shape parameters and the residual vector are known, the the covariance matrix of the feature vector $\mathbf{f}$ and the covariances between the feature vector and the shape parameters can be calculate from equation (3.6) as

$$\mathrm{Cov}(\mathbf{f},\mathbf{f}) = \mathbf{\Psi}_f \Lambda \mathbf{\Psi}_f^T + \epsilon \mathbf{I},\ \mathrm{Cov}(\mathbf{f},\mathbf{w}) = \mathbf{\Psi}_f \Lambda,\ \mathrm{Cov}(\mathbf{w},\mathbf{f}) = \Lambda \mathbf{\Psi}_f^T, \tag{3.8}$$

where Cov represent the covariance matrix.

In statistical shape modeling, it is assumed that the shape parameters are normally distributed. Since equation (3.6) represents a linear relationship between $\mathbf{f}$ and $\mathbf{w}$, so their joint distribution is also normal distribution:

$$p(\mathbf{f},\mathbf{w}) \sim N(\begin{pmatrix} \overline{\mathbf{S}}_f \\ 0 \end{pmatrix}, \begin{pmatrix} \mathbf{\Psi}_f \Lambda \mathbf{\Psi}_f^T + \epsilon \mathbf{I} & \mathbf{\Psi}_f \Lambda \\ \Lambda \mathbf{\Psi}_f^T & \Lambda \end{pmatrix}), \tag{3.9}$$

where $N(\cdot,\cdot)$ stands for the normal distribution with the first parameter its mean and the second parameter its covariance matrix. The conditional distribution of the shape parameters $\mathbf{w}$ given the feature vector is:

$$p(\mathbf{w}|\mathbf{f}) \sim N\left(\Lambda \mathbf{\Psi}_f^T (\mathbf{\Psi}_f \Lambda \mathbf{\Psi}_f^T + \epsilon \mathbf{I})^{-1} (\mathbf{f} - \overline{\mathbf{S}}_f),\ \Lambda - \Lambda \mathbf{\Psi}_f^T (\mathbf{\Psi}_f \Lambda \mathbf{\Psi}_f^T + \epsilon \mathbf{I})^{-1} \mathbf{\Psi}_f \Lambda\right) \tag{3.10}$$

The first term inside $N(\cdot,\cdot)$ is the conditional mean, and the second term is the conditional covariance matrix. Originally, the shape parameters are distributed in a relatively larger area shaped by its covariance matrix Λ. Given the observation of the feature points $\mathbf{f}$, the shape becomes less free since it has to conform with

the observed feature points. So the shape parameters are distributed in a smaller area shaped by the conditional covariance matrix $\Lambda - \Lambda\mathbf{\Psi}_f^T(\mathbf{\Psi}_f\Lambda\mathbf{\Psi}_f^T + \epsilon\mathbf{I})^{-1})\mathbf{\Psi}_f\Lambda$, which tells us the remaining covariance structure of the shape parameters given the observation of the feature points. The remaining variance in the shape parameters is $\text{trace}(\Lambda - \Lambda\mathbf{\Psi}_f^T(\mathbf{\Psi}_f\Lambda\mathbf{\Psi}_f^T + \epsilon\mathbf{I})^{-1}\mathbf{\Psi}_f\Lambda)$, thus the total amount of variance in the shape parameters explained by the feature points is

$$\begin{aligned} \text{var}(\mathbf{w})_{p(\mathbf{w})} - \text{var}(\mathbf{w})_{p(\mathbf{w}|\mathbf{f})} &= \text{trace}(\Lambda) - \text{trace}(\Lambda - \Lambda\mathbf{\Psi}_f^T(\mathbf{\Psi}_f\Lambda\mathbf{\Psi}_f^T + \epsilon\mathbf{I})^{-1}\mathbf{\Psi}_f\Lambda) \\ &= \text{trace}(\Lambda\mathbf{\Psi}_f^T(\mathbf{\Psi}_f\Lambda\mathbf{\Psi}_f^T + \epsilon\mathbf{I})^{-1}\mathbf{\Psi}_f\Lambda), \end{aligned} \tag{3.11}$$

and the percentage of the variance in the training shapes explained by the feature points is

$$\varrho_{\mathbf{S}}(\mathbf{f}) = \text{trace}(\Lambda\mathbf{\Psi}_f^T(\mathbf{\Psi}_f\Lambda\mathbf{\Psi}_f^T + \epsilon\mathbf{I})^{-1}\mathbf{\Psi}_f\Lambda) / \sum_{k=1}^{n_s-1}\lambda_k. \tag{3.12}$$

By equation (3.12), we have Definition 1 for the selection of feature points.

Definition 1: The most important feature points on the shapes are the ones that capture the highest percentage of the variance of the shape population.

By Definition 1, the optimization formula for feature points selection is:

$$\max_{\{i_1\cdots i_{n_f}\}\subset\{1\cdots n_v\}} \varrho_{\mathbf{S}}(\mathbf{f}). \tag{3.13}$$

Assume the set of training shapes well represent the underlying shape population, then the subject-shapes that will be encountered in future also follow the same

distribution $p(\mathbf{f}, \mathbf{w})$, the expectation of the squared error of shape reconstructions by the chosen feature points is:

$$\begin{aligned} E^{se} &= \int (\mathbf{w}_{test} - \tilde{\mathbf{w}})^T (\mathbf{w}_{test} - \tilde{\mathbf{w}}) p(\mathbf{w}_{test}|\mathbf{f}) \\ &= \text{trace}(\Lambda - \Lambda \mathbf{\Psi}_f^T (\mathbf{\Psi}_f \Lambda \mathbf{\Psi}_f^T + \epsilon \mathbf{I})^{-1} \mathbf{\Psi}_f \Lambda), \end{aligned} \tag{3.14}$$

where $\tilde{\mathbf{w}} = \Lambda \mathbf{\Psi}_f^T (\mathbf{\Psi}_f \Lambda \mathbf{\Psi}_f^T + \epsilon \mathbf{I})^{-1} (\mathbf{f} - \overline{\mathbf{S}}_f)$ is the conditional mean in (3.10) and is used to estimate the shape parameters from the positions of the feature points. If the feature points are selected according to (3.13), then E^{se} is minimized.

The optimization problem in (3.13) is N^p hard [62] whose global optimal can only be achieved by exhaustive search, which is very time consuming. For example, selecting 30 feature points from the human body shape with 6000 vertices will evaluate equation (3.12) for $C_{6000}^{30} = 7.75e + 80$ times, which is computational prohibitive. Instead of optimizing globally, here a forward selection algorithm is developed for two reasons: 1) it efficiently finds a suboptimal solution that is good enough; 2) it gives a ranking of the selected feature points that tells which points are more important and which are less.

Algorithm 1:

1. Firstly, the point $\mathbf{v}_{i_1}$ that maximizes (3.12) is added to the set $\mathbb{I}$.
2. The next point is added such that $\varrho_{\mathbf{S}}(\mathbf{v}_{\mathbb{I}}, \mathbf{v}_i)$ is maximized. Keep iterate until n_f number of feature points are selected.

Figure 3.6 shows the first four feature points selected by Algorithm 1. The color shows the percentage variance $\varrho_{\mathbf{S}}(\mathbf{v}_{\mathbb{I}}, \mathbf{v}_i)$ captured by moving the feature point on

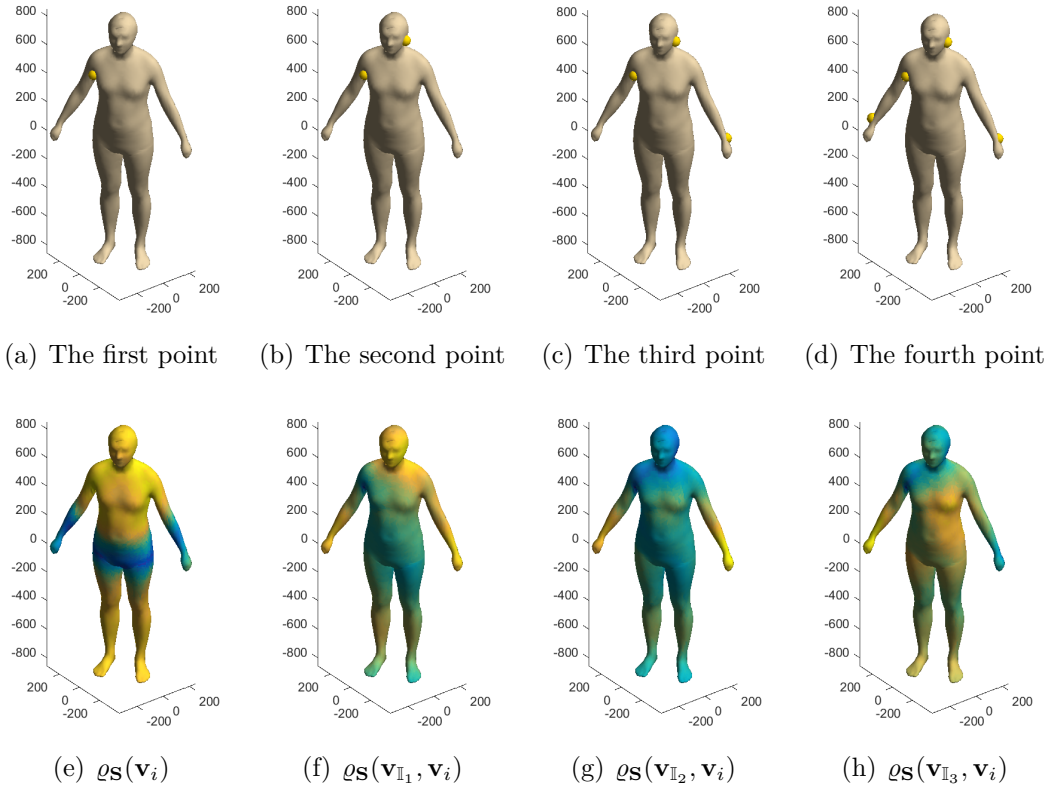

(a) The first point (b) The second point (c) The third point (d) The fourth point

(e) $\varrho_{\mathbf{S}}(\mathbf{v}_i)$ (f) $\varrho_{\mathbf{S}}(\mathbf{v}_{\mathbb{I}_1}, \mathbf{v}_i)$ (g) $\varrho_{\mathbf{S}}(\mathbf{v}_{\mathbb{I}_2}, \mathbf{v}_i)$ (h) $\varrho_{\mathbf{S}}(\mathbf{v}_{\mathbb{I}_3}, \mathbf{v}_i)$

Figure 3.6: Feature points (yellow balls) on the human body model selected by Algorithm 1. The color shows the percentage variance $\varrho_{\mathbf{S}}(\mathbf{v}_{\mathbb{I}}, \mathbf{v}_i)$ captured by moving the feature point on the shape surface. The warmest color corresponds to the highest percentage of variance.

the surface of the shape. The warmest color corresponds to the highest percentage of variance, and is where the next feature point is put.

3.4 Applications

In this section, we demonstrate how to incorporate the feature point identification approach in the below applications: 1) sparse shape reconstruction; 2) dimensions

construction and selection; 3) shape classification by sparse measurements.

3.4.1 Sparse shape reconstruction

The feature points are selected by maximizing the amount of variance they capture of the shape population, which makes them powerful for being the marker points in sparse shape reconstruction.

The shape reconstruction is based on the statistical shape model and takes two steps:

1) Estimate the corresponding shape parameters $\mathbf{w} = [w_1, w_2, \cdots, w_m]^T$ by the coordinates of the observed feature points

$$\widetilde{\mathbf{w}} = \Lambda \mathbf{\Psi}_f^T (\mathbf{\Psi}_f \Lambda \mathbf{\Psi}_f^T + \epsilon \mathbf{I})^{-1} (\mathbf{f} - \overline{\mathbf{S}}_f), \tag{3.15}$$

note that $\widetilde{\mathbf{w}}$ is the conditional mean in (3.10).

2) Reconstruct the shape by the estimated shape parameters $\tilde{\mathbf{S}} = \overline{\mathbf{S}} + \mathbf{\Psi}\widetilde{\mathbf{w}}$.

Through statistical shape modeling, the probabilistic distribution $p(\mathbf{w})$ of the shape parameters is obtained as in (3.4). Without any other information, the maximum likelihood estimation of the shape parameters will be $\mathbf{w} = \mathbf{0}$, which is just the mean shape. Given the information of the feature vector $\mathbf{f}$, the conditional distribution $p(\mathbf{w}|\mathbf{f})$ of the shape parameters is obtained as in equation (3.10). The maximum likelihood estimation of $\mathbf{w}$ is then the corresponding conditional expectation as in equation (3.15).

3.4.2 Dimension construction and selection

As pointed out in [5], there is no standardized method to determine what the suitable dimensions are and how to choose them for the parametric shape design. In their study, twelve dimensions that are related to facial anatomy are chosen. In [24], 24 dimensions were manually constructed from the 14 expert chosen geometrical feature points. Here, a way to automatically construct and select sizing dimensions is given. It takes two steps: firstly, a dimension pool that contains a large number of dimensions is automatically constructed. Secondly, a subset of the dimensions in the pool is selected and ranked by the amount of variance they capture of the shape population.

The dimension pool is composed of lengths and angles obtained by measuring the feature points in a combinatorial manner. Given the feature points $\mathbf{v}_{i_1}, \mathbf{v}_{i_2}, \cdots, \mathbf{v}_{i_{n_f}}$, $C_{n_f}^2 = n_f(n_f-1)/2$ number of length dimensions are constructed:

$$\left\{ l_1, l_2, \cdots, l_{n_f(n_f-1)/2} \right\}. \tag{3.16}$$

Similarly, $3C_{n_f}^3 = n_f(n_f-1)(n_f-2)/2$ number of angle dimensions are constructed by each time choosing three feature points and measuring the angles of the composed triangle:

$$\left\{ \theta_1, \theta_2, \cdots, \theta_{n_f(n_f-1)(n_f-2)/2} \right\}. \tag{3.17}$$

Combined with the list of traditional measurements [1], a big pool of dimensions

is constructed:

$$\mathbb{P} = \{l_1, l_2, \cdots, l_N\}. \tag{3.18}$$

A subset of dimensions $\mathbf{L} = [l_{j_1}, l_{j_2}, l_{j_{n_l}}]$ is selected from $\mathbb{P}$ by maximizing the variance they capture of the shape population.

It is worth noting that $\mathbb{P}$ usually contains hundreds or even thousands of dimensions (e.g. $C_{12}^2 = 66, 3C_{12}^3 = 660$). Some of the dimensions in $\mathbb{P}$ may be correlated or even dependent on each other. However, the goal of dimension construction is to create enough number of candidates for the dimension selection. It doesn't matter whether the dimensions in $\mathbb{P}$ are dependent or not, since the selected dimensions will be as independent as possible. Any dimension that is dependent on the dimensions in $\mathbf{L}$ will not be selected since it has no contribution to capturing the population variance.

In order to compute the amount of variance of the shape population captured by the selected dimensions, the joint probability $p(\mathbf{w}, \mathbf{L})$ of the shape parameters $\mathbf{w}$ and the sizing dimensions $\mathbf{L}$ is learned from the training shapes. The covariance matrix Λ of the shape parameters is already obtained by statistical shape modeling. The covariance matrix Σ_l of the selected dimensions $\mathbf{L}$ is obtained by measuring on the training shapes:

$$\Sigma_l = \sum_{k=1}^{n_s} (\mathbf{L}_k - \overline{\mathbf{L}})(\mathbf{L}_k - \overline{\mathbf{L}})^T / (n_s - 1), \tag{3.19}$$

where $\mathbf{L}_k$ are the measurements on the kth training shape, $\overline{\mathbf{L}} = \sum_{k=1}^{n_s} \mathbf{L}_k / n_s$ is the mean dimension vector of the training shapes, the covariance matrix between the shape

parameters and the sizing dimensions is obtained by:

$$\Sigma_{lw} = \sum_{k=1}^{n_s} (\mathbf{L}_k - \overline{\mathbf{L}})\mathbf{w}_k^T/(n_s - 1), \tag{3.20}$$

where $\mathbf{w}_k$ is the vector of shape parameters for the kth training shape. Under the assumption of normal distribution, we have the joint probability

$$p(\mathbf{L}, \mathbf{w}) \sim N(\begin{pmatrix} \overline{\mathbf{L}} \\ 0 \end{pmatrix}, \begin{pmatrix} \Sigma_l & \Sigma_{lw} \\ \Sigma_{wl} & \Lambda \end{pmatrix}), \tag{3.21}$$

where $N(\cdot, \cdot)$ stands for the normal distribution. The corresponding conditional distribution is:

$$p(\mathbf{w}|\mathbf{L}) \sim N(\Sigma_{wl}\Sigma_l^{-1}(\mathbf{L} - \overline{\mathbf{L}}),\ \Lambda - \Sigma_{wl}\Sigma_l^{-1}\Sigma_{lw}), \tag{3.22}$$

where the first item inside $N(\cdot, \cdot)$ is the conditional mean, the second item is the conditional covariance. The variance in the shape parameters captured by the selected dimensions is:

$$\begin{aligned} \text{var}(\mathbf{w})_{p(\mathbf{w})} - \text{var}(\mathbf{w})_{p(\mathbf{w}|\mathbf{L})} &= \text{trace}(\Lambda) - \text{trace}(\Lambda - \Sigma_{wl}\Sigma_l^{-1}\Sigma_{lw}) \\ &= \text{trace}(\Sigma_{wl}\Sigma_l^{-1}\Sigma_{lw}) \end{aligned} \tag{3.23}$$

The percentage of the variance in the training shapes explained by the selected

dimensions is:

$$\varrho_{\mathbf{S}}(\mathbf{L}) = \text{trace}(\Sigma_{wl}\Sigma_l^{-1}\Sigma_{lw}) / \sum_{k=1}^{n_s-1} \lambda_k. \tag{3.24}$$

Based on the foregoing deducing, we have Lemma 2 for the dimension selection.

Definition 2: the best set $\mathbf{L} = [l_{j_1}, l_{j_2}, \cdots, l_{j_{n_l}}] \subset \mathbb{P}$ of dimensions are the ones that captures the highest percentage of the variance of the shape population:

$$\max_{\{l_{j_1} \cdots l_{j_{n_l}}\} \subset \mathbb{P}} \varrho_{\mathbf{S}}(\mathbf{L}). \tag{3.25}$$

Assume the set of training shapes well represent the underlying shape population, and the shape parameters and sizing dimensions are normally distributed, then the subject-shapes that will be encountered in future also follow the same distribution $p(\mathbf{L}, \mathbf{w})$, the expectation of the squared error of parametric shape synthesis by the selected dimensions is:

$$\begin{aligned} E^{se} &= \int (\mathbf{w}_{test} - \tilde{\mathbf{w}})^T (\mathbf{w}_{test} - \tilde{\mathbf{w}}) p(\mathbf{w}_{test}|\mathbf{L}) \\ &= \text{trace}(\Lambda - \Sigma_{wl}\Sigma_l^{-1}\Sigma_{lw}), \end{aligned} \tag{3.26}$$

where $\tilde{\mathbf{w}} = \Sigma_{wl}\Sigma_l^{-1}(\mathbf{L} - \overline{\mathbf{L}})$ is the conditional mean in (3.22) and is used to synthesize the shape parameters from the sizing dimensions. If the dimensions are selected according to (3.25), then E^{se} is minimized.

Similar as in formula (3.13), the optimization problem in (3.25) is N^p hard [62].

A forward selection algorithm is developed for 1) efficient dimension selection, and 2) ranking the selected dimenions.

Algorithm 2:

1. Firstly, the dimension l_{j_1} that maximizes $\varrho_{\mathbf{S}}(\mathbf{L})$ is added to the set $\mathbf{L}$.

2. The next dimension is added such that $\varrho_{\mathbf{S}}(\mathbf{L}, l_j)$ is maximized. Keep iterate until n_l number of dimensions are selected.

The selected dimensions can be applied in the parametric shape design [14], the mass-customization [24] and the personalized item design [5], since a faithful 3D shape model of the given subject can be efficiently synthesized by the conditional mean in (3.22).

3.4.3 Shape classification by key dimensions

Shape classification is of critical importance in clinics. It can help diagnosis healthy and unhealthy anatomical structures [63] and study the effects of surgeries [64]. It is ideal to have complete shape models for classification and comparing. However, due to the tedious and error-prone process [13] of obtaining neat shape models from images and scanned point clouds, its applications have been limited.

In this section an approach is proposed to construct and select dimensions that can effectively distinguish two different groups of shapes, it takes two steps:

1) Identify the shape parameters $\hat{\mathbf{w}} = [w_{i_1}, \cdots, w_{i_d}]^T \subset [w_1, \cdots, w_m]$ that are related to group differences. Since the shape parameters are uncorrelated to each other due to principal component analysis, the student-t-test is conducted for each

shape parameter separately to decide whether that shape parameter shows differences across the two groups or not.

2) The dimensions are selected to capture the variances in the selected shape parameters $\hat{\mathbf{w}} = [w_{i_1}, \cdots, w_{i_d}]^T$:

$$\max_{\mathbf{L} \subset \mathbb{P}} \ \varrho_{\hat{\mathbf{w}}}(\mathbf{L}) = \text{trace}(\Sigma_{\hat{w}l} \Sigma_l^{-1} \Sigma_{l\hat{w}}) / \sum_{k=1}^{d} \lambda_{i_k}. \tag{3.27}$$

3.5 Numerical examples

The numerical examples are used to test the proposed feature point identification approach and to demonstrate its applications in sparse shape reconstruction, construction of new dimensions and shape classification by sparse measurements.

3.5.1 The Caesar human body models

The Caesar human body database [1] is used to demonstrate the feature point identification and its applications in sparse shape reconstruction and construction of new dimensions. The human body shape models are represented by the boundary triangulations, the 4308 fitted meshes $\{\mathbf{S}_1, \mathbf{S}_2, \cdots, \mathbf{S}_{4308}\}$ in [65] are used in this paper, among which 4092 shapes are used as the training shapes to learn the statistical shape model, select the feature points, and construct new dimensions, 216 shapes are used as the testing shapes for validation. Ideally, to eliminate the sampling bias, the training shapes and testing shapes should be sampled randomly from the database,

however, for the repeatability of the results, the testing shapes are sampled by an interval of 20:

$$\mathbb{S}^{test} = \{\mathbf{S}_1, \mathbf{S}_{21}, \mathbf{S}_{41}, \cdots \mathbf{S}_{4301}\}. \tag{3.28}$$

The remaining shapes are used as the training shapes:

$$\mathbb{S}^{train} = \{\mathbf{S}_2, \mathbf{S}_3, \cdots, \mathbf{S}_{20}, \mathbf{S}_{22}, \mathbf{S}_{23}, \cdots, \mathbf{S}_{40}, \cdots, \mathbf{S}_{4308}\}. \tag{3.29}$$

Feature point identification

At the previous section in Figure 3.6 we show the first four feature points selected from the 6449 vertices by Algorithm 1. Figure 3.7 shows more intermediate results as Algorithm 1 goes from $n_f = 5$ to $n_f = 30$, where n_f is the number of feature points. The top and bottom rows in Figure 3.7 show the front and back views of the human body model. The corresponding statistical shape model is as shown in Section 2.

As shown in Figure 3.6 and Figure 3.7(a), the first point is placed at the armpit, whose position is highly correlated with the first two variation modes (height and width); the second point is placed near the ear (the real ear is missing due to smoothing), which captures the variations above the shoulder; the third and fourth points are placed at the wrists, which capture the variations in the arm length and poses, the fifth point is at the waist, which tell us something about the lower body (i.e. waist height and width).

Checking the other sub-figures in Figure 3.7, it can be seen that the selected feature points distributed evenly on the human body and many of them are at the

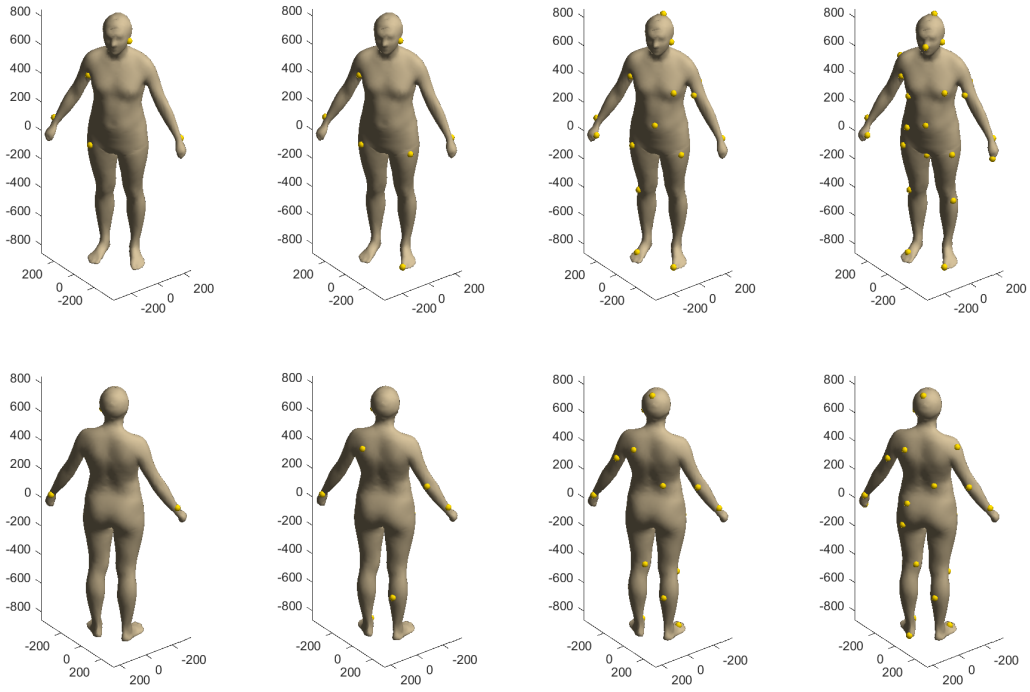

(e) $n_f = 5$ (f) $n_f = 10$ (g) $n_f = 20$ (h) $n_f = 30$

Figure 3.7: The selected feature points (yellow sphere) on the human body model: (a) 5 feature points; (b) 10 feature points; (c) 20 feature points; (d) 30 feature points. The upper and lower rows show the front and back views.

anatomically meaningful places. For example, the point at the belly button, the points at the toes and heels, and the points are the joints (knee joints, arm joints), which shows the reasonability of Algorithm 1.

Figure 3.8 compares the 67 feature points selected by Algorithm 1 and the 67 well defined anatomical landmarks in CAESAR project [1]. It can be seen that the feature points selected by Algorithm 1 are distributed more evenly. For example, the anatomical landmarks from CAESAR database do not have points on the hip, however the shape variation of hip is in-negligible across the population.

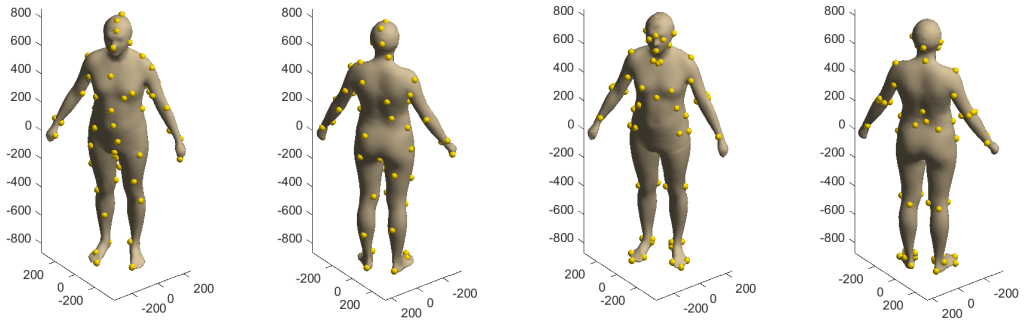

(a) Front view (b) Back view (c) Front view (d) Back view

Figure 3.8: The 67 feature points selected by (a) and (b) Algorithm 1, (c) and (d) well defined anatomical landmarks from CAESAR.

In the foregoing, the feature points are selected from all the 6449 vertices on the human body model. However, the precise positions of some of the selected feature points are hard to locate (e.g. the points in the vast middle area of the belly). Instead of selecting from all the vertices, we select just from the 67 well-defined anatomical landmarks. Figure 3.9 shows the feature points selected from the anatomic landmarks.

Sparse shape reconstruction

In this section, the selected feature points are used as the markers in sparse shape reconstruction. The positions of the feature points $\mathbf{f}$ on the testing shapes are measured and a new shape $\widetilde{\mathbf{S}}_i^{test} = \overline{\mathbf{S}} + \mathbf{\Psi}\widetilde{\mathbf{w}}(\mathbf{f})$ is constructed. The shape parameters $\widetilde{\mathbf{w}}$ are estimated by equation (3.15) by the feature points $\mathbf{f}$. The surface deviation between the reconstructed shape and the original shape is used to evaluate the quality

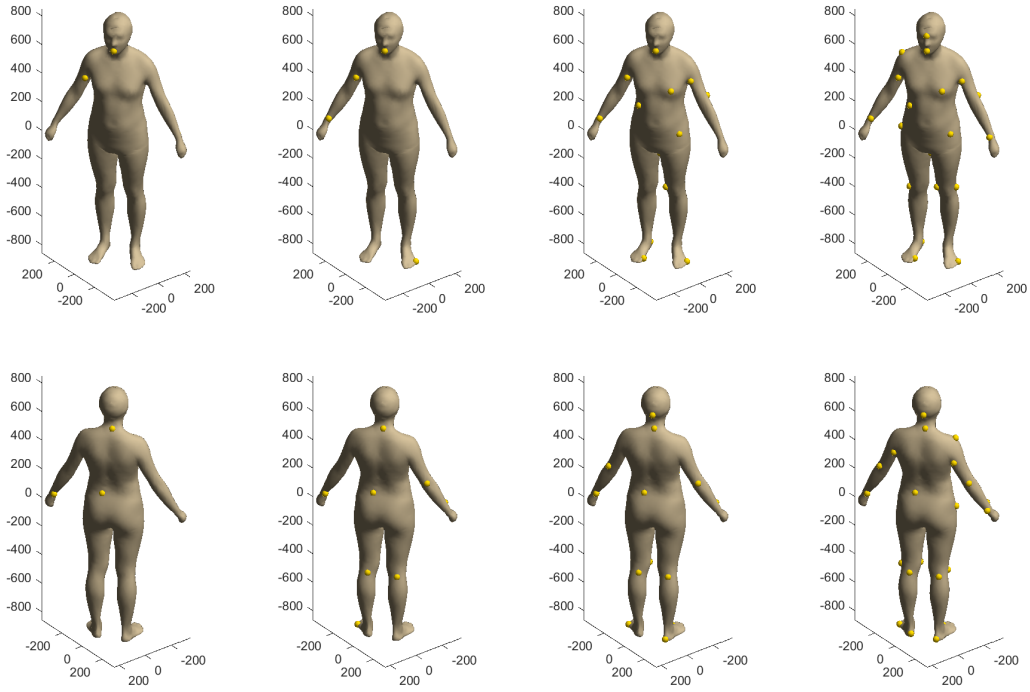

(e) $n_f = 5$ (f) $n_f = 10$ (g) $n_f = 20$ (h) $n_f = 30$

Figure 3.9: Feature points selected from the anatomic landmarks: (a) 5 feature points; (b) 10 feature points; (c) 15 feature points; (d) 20 feature points. The upper and lower rows show the front and back views.

of the reconstruction. The mean surface deviation is calculated as below:

$$d_i = \frac{1}{n_v} \sum_{j=1}^{n_v} \|\mathbf{v}_j^{test_i} - \widetilde{\mathbf{v}}_j^{test_i}\|, \ i = 1, \cdots, 216, \tag{3.30}$$

where $\mathbf{v}_j^{test_i}$ is the position of a vertex on the ith testing shape, $\widetilde{\mathbf{v}}_j^{test_i}$ is the position of the vertex on the reconstructed shape.

Figure 3.10 shows the results of sparse shape reconstruction by the 67 feature points selected from the 6449 vertices (middle row) and by the 67 anatomical landmakrs

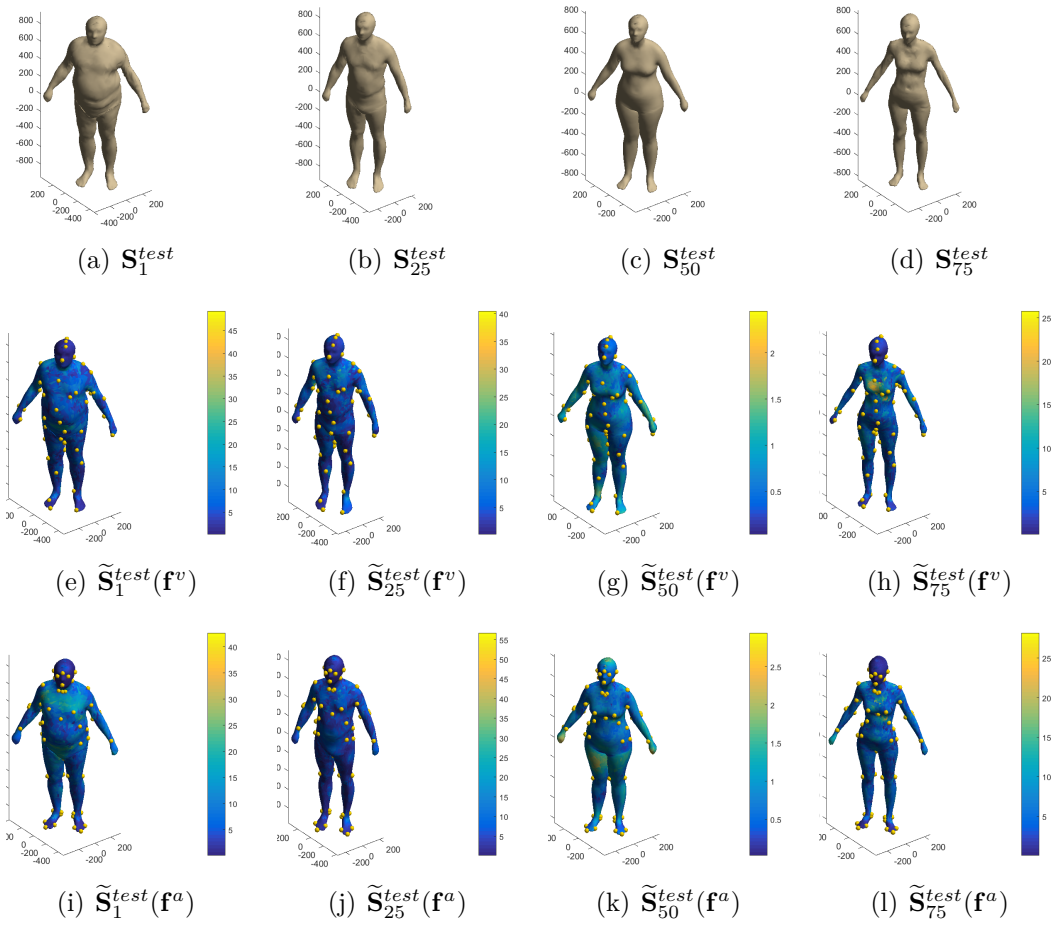

(a) $\mathbf{S}_1^{test}$ (b) $\mathbf{S}_{25}^{test}$ (c) $\mathbf{S}_{50}^{test}$ (d) $\mathbf{S}_{75}^{test}$

(e) $\widetilde{\mathbf{S}}_1^{test}(\mathbf{f}^v)$ (f) $\widetilde{\mathbf{S}}_{25}^{test}(\mathbf{f}^v)$ (g) $\widetilde{\mathbf{S}}_{50}^{test}(\mathbf{f}^v)$ (h) $\widetilde{\mathbf{S}}_{75}^{test}(\mathbf{f}^v)$

(i) $\widetilde{\mathbf{S}}_1^{test}(\mathbf{f}^a)$ (j) $\widetilde{\mathbf{S}}_{25}^{test}(\mathbf{f}^a)$ (k) $\widetilde{\mathbf{S}}_{50}^{test}(\mathbf{f}^a)$ (l) $\widetilde{\mathbf{S}}_{75}^{test}(\mathbf{f}^a)$

Figure 3.10: Sparse shape reconstruction. Top row: the test shapes; middle row: the shapes reconstructed by the 67 feature points $\mathbf{f}^v$ selected from the 6449 vertices; bottom row: the shapes reconstructed by the 67 anatomical landmarks $\mathbf{f}^v a$. The color shows the value of surface deviation in millimeter.

(bottom row). It can be seen that the maximum surface deviations in the middle row are smaller than that of the bottom row.

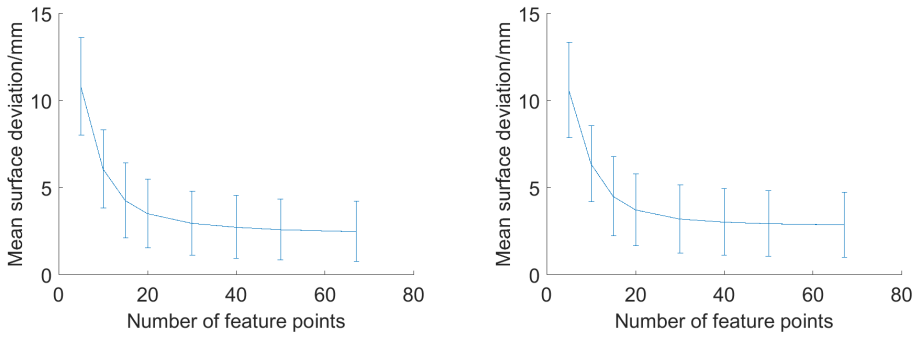

(a) Mean surface deviation (b) Mean surface deviation

Figure 3.11: The mean surface deviations of the shape reconstruction with different number of feature points: (a) feature points are selected from the 6449 vertices; (b) feature points are selected from the 67 anatomical landmakrs.

As shown in Figure 3.11 are the mean surface deviations (3.30) of the shape reconstruction with different number of feature points. The feature points for Figure 3.11(a) are selected from the 6449 vertices. The feature points for Figure 3.11(b) are selected from the 67 anatomical landmakrs. The curve in Figure 3.11(a) and 3.11(b) shows the average of the mean surface deviation over the 216 testing shapes: $\overline{d} = \sum_{i=1}^{216} d_i/216$, the error bar shows the standard deviation of the mean surface deviation over the 216 testing shapes: $\sqrt{\frac{1}{215}\sum_{i=1}^{216}(d_i - \overline{d})^2}$. It could be seen that as the number of feature points increases, the mean surface deviation becomes smaller. At last, the average of the mean surface deviation in Figure 3.11(a) is 2.47mm and in Figure 3.11(b) is 2.86mm, which suggests the accuracy of the reconstruction.

Table 3.1 shows the values of the mean surface deviations, where n_f is the number

Table 3.1: Reconstruction errors by different number of feature points: mm

n_f	5	10	15	20	30	40	50	67
$\overline{d}^{(1)}$	10.81	6.08	4.26	3.51	2.95	2.73	2.59	2.47
$\overline{d}^{(2)}$	10.60	6.37	4.50	3.73	3.20	3.02	2.93	2.86

of feature points, $\overline{d}^{(1)}$ is the mean surface deviation of the reconstructions by the feature points selected from all the vertices, $\overline{d}^{(2)}$ is the mean surface deviation of the reconstructions by the feature points selected from the anatomical landmarks.

It can be seen that the mean surface deviations in the first row is smaller than that in the second row. That's because the feature points for the first row are selected from a much larger pool than the second row. This also demonstrates the effectiveness of Algorithm 1, since the selected feature points in the first case are more powerful than the expert defined anatomical landmarks.

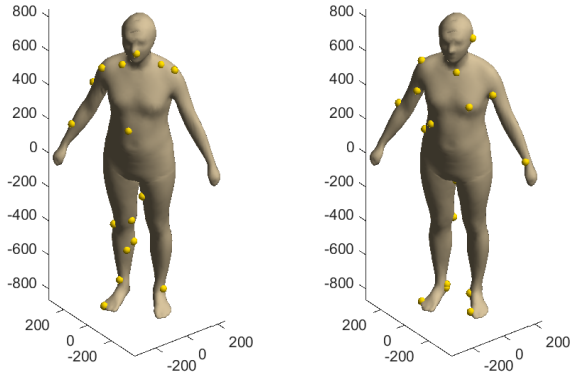

(a) Randomly generated from the 6449 vertices

(b) Randomly generated from the anatomical landmarks

Figure 3.12: The 20 feature points randomly generated from (a) the 6449 vertices, (b) the anatomical landmarks.

To further validate the capability of the feature points selected from the 6449 vertices and from the 67 anatomical landmarks, their performance in sparse shape reconstruction is compared with 100 sets of points randomly generated from the 6449 vertices and from the 67 anatomical landmarks respectively. Figure 3.12 shows two examples of randomly generated feature points.

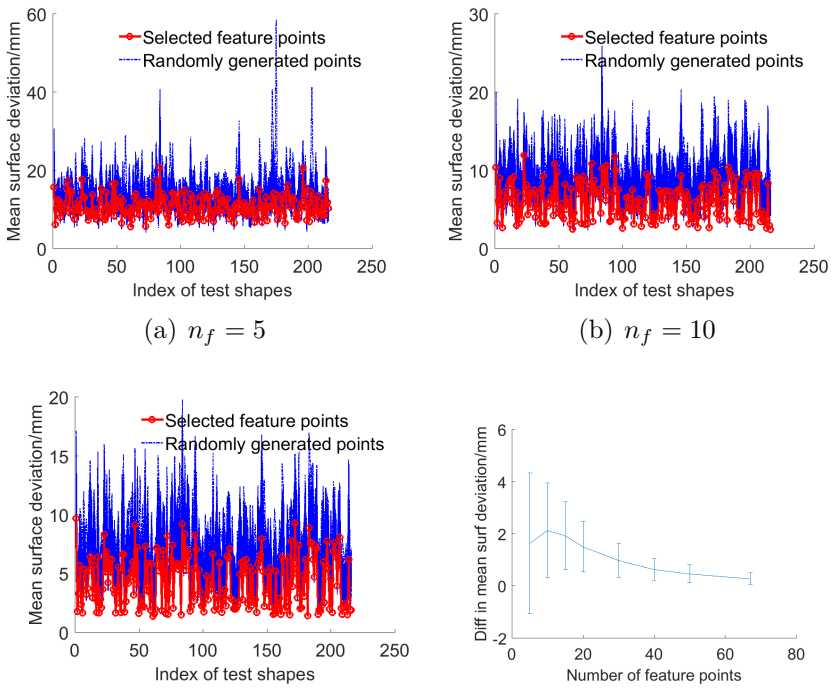

(a) $n_f = 5$

(b) $n_f = 10$

(c) $n_f = 15$

(d) Difference in the mean surface deviation

Figure 3.13: The mean surface deviations of reconstructions of the 216 testing shapes by the selected feature points and by the 100 sets of randomly generated points. Both of the points are selected from the 6449 vertices.

Figure 3.13 shows the mean surface deviations of reconstructions by the selected feature points and by the 100 sets of randomly generated points. Both are selected from the 6449 vertices. It can be seen that the reconstruction error of the selected

feature points is smaller than that of the randomly generated feature points, it stays at the bottom of all the errors curves in Figure 3.13(a), 3.13(b) and 3.13(c). Figure 3.13(d) shows the differences in the mean surface deviation of reconstructions by the selected feature points and by the randomly generated points. The curve shows the average difference over the 216 testing shapes and over the 100 set of randomly generated points: $\frac{1}{100}\sum_{j}^{100}\frac{1}{216}\sum_{i=1}^{216}(d_i^{random_j} - d_i)$, the error bar shows the standard deviation of $d_i^{random_j} - d_i$. It can be seen that the reconstruction by the selected feature points is more precise than that of the randomly generated points. However, as the number of feature points increases, the difference becomes smaller. That is due to the compactness of the statistical shape model (the first 39 eigen-modes captures more than 99% of the total shape variance), so we don't need too many feature points to capture the major shape variance in the population. Some of the feature points will become redundant as the number of the feature points increases.

Figure 3.14 shows the mean surface deviations of the reconstructions by the selected feature points and by the 100 sets of randomly generated points. Both are selected from the 67 anatomical landmarks. It can be seen that the reconstruction error of selected feature points is smaller than that of the randomly generated points, it stays at the bottom of all the errors curves in Figure 3.14(a), 3.14(b) and 3.14(c). Figure 3.14(d) shows the differences in the mean surface deviation of reconstructions by the selected feature points and by the randomly generated points. The curve shows the average difference over the 216 testing shapes and over the 100 sets of randomly generated points, the error bar shows the standard deviation of the differences. It could be seen that the reconstruction by the selected feature points is more precise

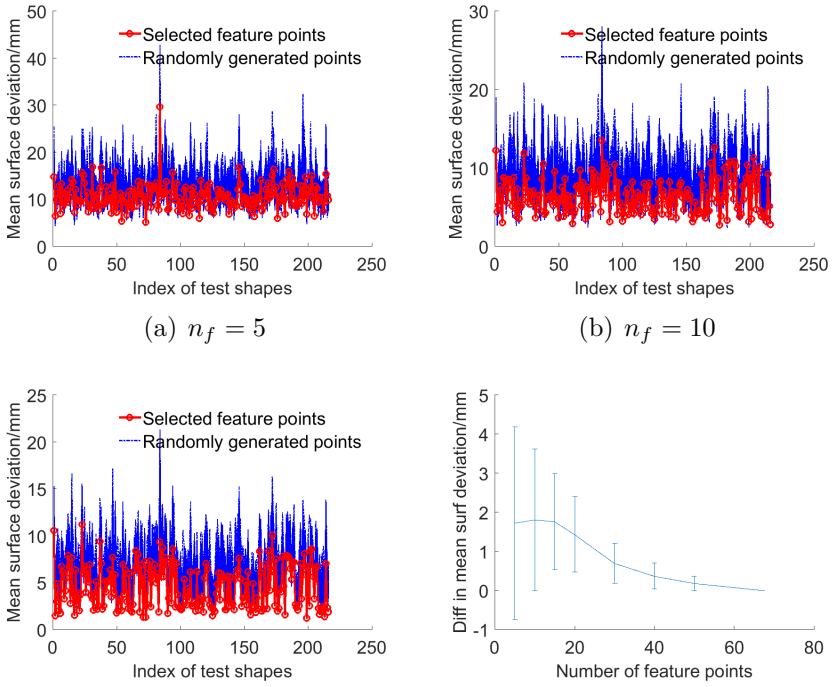

(a) $n_f = 5$ (b) $n_f = 10$

(c) $n_f = 15$ (d) Difference in the mean surface deviation

Figure 3.14: The mean surface deviations of the reconstructions of the 216 testing shapes by the selected feature points and by the 100 sets of randomly generated points. Both of the points are selected from the anatomical landmarks.

than that of randomly generated points.

Dimension construction and selection

The 12 most important feature points (the percentage variance captured = 96.8%) selected from the 67 anatomical landmarks are used for dimension construction. Based on which $C_{12}^2 = 66$ lengths and $3C_{12}^3 = 660$ angles are constructed. Combined with the 25 dimensions from the traditional measurement list:

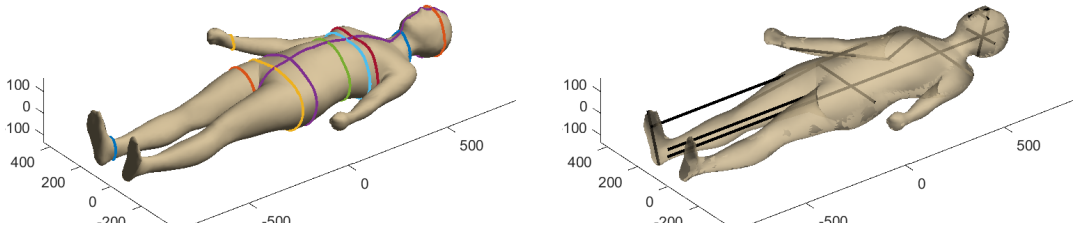

(a) Circumferences (b) Lengths

Figure 3.15: Dimensions from the traditional measurement list: (a) the 11 circumferences, (b) the 14 lengths.

- Circumferences: ankle circ, chest girth, chest circ under bust, head circ, waist circ, vertical trunk circ, hand circ, neck base circ, hip circ maximum, thigh circ maximum, hip circ maximum height.

- Lengths: stature, foot length, arm length (spine-shoulder), arm length (spine-elbow), arm length (spine-wrist), head length, bizygomatic breadth, head breadth, waist height preferred, shoulder (bideltoid) breadth, crotch height, buttock-knee length, face length, hip breadth.

We have a pool of 751 dimensions: $\mathbb{P} = \{l_1 \cdots l_{751}\}$. Figure 3.15 shows the 25 dimensions from the traditional measurement list.

In this section, the dimensions that are selected by expert and by Algorithm 2 are compared. The 4092 training shapes are used to select meaningful dimensions among the population. The 216 testing shapes are used to test the selected dimensions in shape synthesis (3.22). The dimensions are firstly selected from only the traditional measurement list, whose results are then compared with the selections from the big pool $\mathbb{P} = \{l_1 \cdots l_{751}\}$, which includes the constructed dimensions.

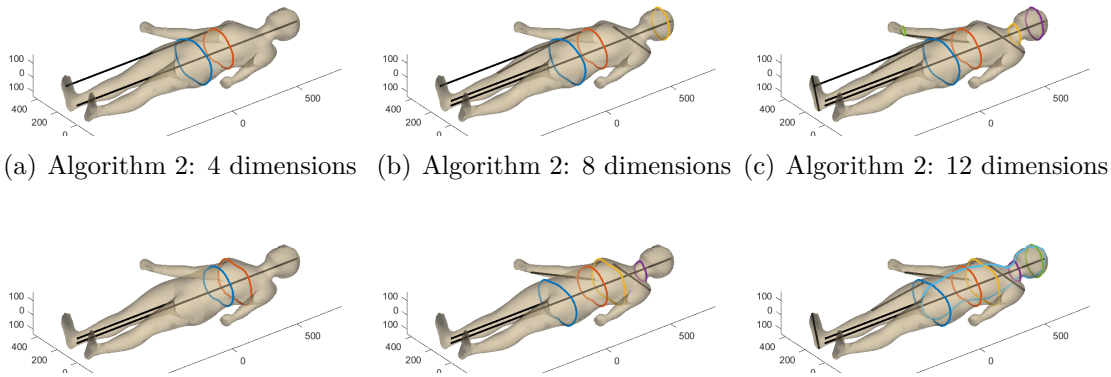

(a) Algorithm 2: 4 dimensions (b) Algorithm 2: 8 dimensions (c) Algorithm 2: 12 dimensions

(d) Expert: 4 dimensions (e) Expert: 8 dimensions (f) Expert: 12 dimensions

Figure 3.16: Dimension selection from the traditional measurement list.

Figure 3.16 shows the results of dimensions selection from the traditional measurement list. Two selection approaches are used: dimension selection by Algorithm 2 and dimension selection by expert.

The first column shows the most important 4 dimensions selected by the two approaches. The dimensions selected by Algorithm 2 are: the height of the body, the waist, the circumference of the buttock, and the height of the waist. The dimensions selected by expert are: the height of the body, the waist, the circumference of the chest, and the height of the crotch. The second and third columns show the most important 8 dimensions and 12 dimensions selected by the two approaches.

Figure 3.17 shows the errors of shape reconstructions of the 216 testing shapes by the dimensions selected from the traditional list. Figure 3.17(a) shows the error of shape reconstructions by the dimensions selected by Algorithm 2. Figure 3.17(b) shows the differences in the shape reconstruction by the expert selected dimensions and by the dimensions selected by Algorithm 2. It could be seen that Algorithm 2

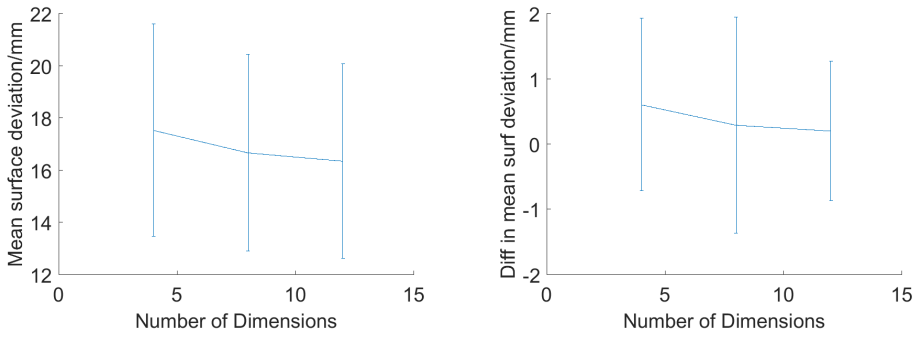

(a) Mean surface deviation

(b) Difference in the mean surface deviation

Figure 3.17: Reconstruction error with different number of dimensions selected from the traditional list: (a) mean surface deviations of the reconstructions by the dimensions selected by Algorithm 2; (b) differences in the mean surface deviations of the reconstructions by the dimensions selected by Algorithm 2 and by expert. The unit is millimeter.

gives smaller errors. However, one thing observed is that the reconstruction errors doesn't decrease much as we increase the number of dimensions, as shown in Figure 3.17(a). This means that some of shape variations in the population are not captured by the list of traditional measurements and new dimensions need to be constructed, which is better illustrated by Figure 3.18.

Figure 3.18 shows the confidence region of the conditional distributions of the shape parameters in the training set, which is obtained from equation (3.21). The red point shows the true shape parameter of the testing shape being investigated. It can be seen that as the number of dimensions increases, the area of the confidence region of $p(w_1, w_2|\mathbf{L})$ decrease obviously, which means that the information provided by the additional dimensions can effectively localize the first two shape parameters of the unknown testing shape. However, the area of the confidence region of $p(w_3, w_4|\mathbf{L})$

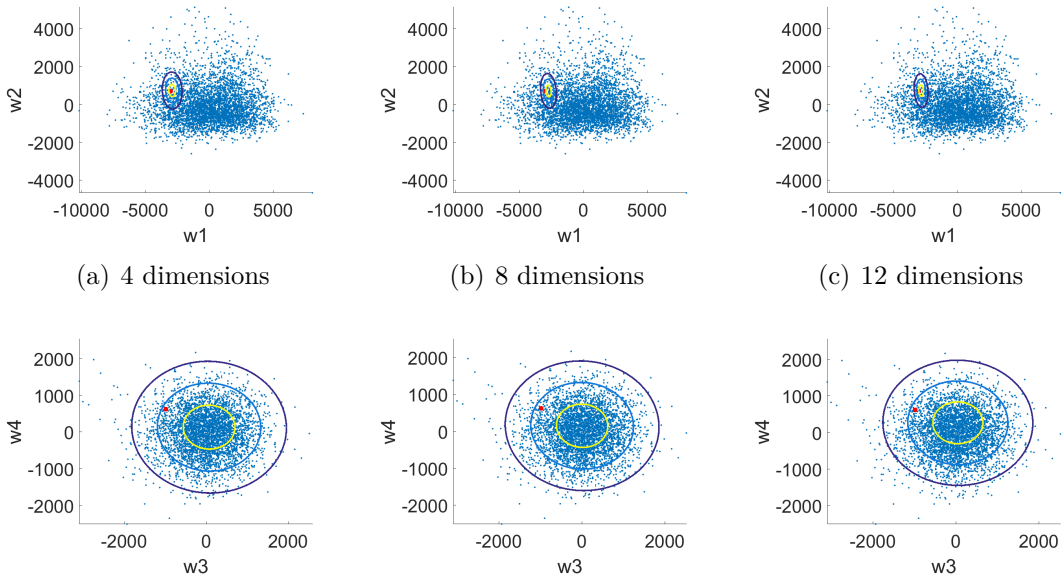

(a) 4 dimensions (b) 8 dimensions (c) 12 dimensions

(d) 4 dimensions (e) 8 dimensions (f) 12 dimensions

Figure 3.18: Confidence regions (66%, 90%, 99%) of the conditional distributions $p(w_1, w_2|\mathbf{L})$ (upper row) and $p(w_3, w_4|\mathbf{L})$ (bottom row). The red point shows the true shape parameter of the testing shape being investigated.

barely decreases, which means that the information provided by the additional dimensions are not relevant.

Figure 3.19 shows the results of dimension selection from the combined pool $\mathbb{P}$, which contains 751 dimensions (25 from the traditional measurement list and 726 constructed from the selected feature points). The first column shows the most important 4 dimensions. It can be seen that the lengths from nose to both hands are selected from the list of constructed dimensions. The second and third columns show the most important 8 dimensions and 12 dimensions selected from the combined pool $\mathbb{P}$. It can be seen that angles are selected, which are constructed by the line segments connecting the feature points. The angles can be computed by the edge lengths of

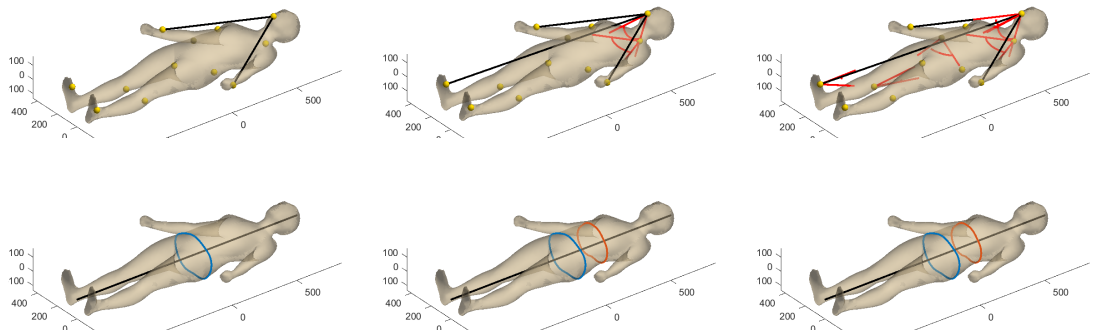

(d) 4 dimensions (e) 8 dimensions (f) 12 dimensions

Figure 3.19: Dimensions selected from the combined pool $\mathbb{P}$ by Algorithm 2: (a) the 4 most important dimensions, (b) the 8 most important dimensions, (c) the 12 most important dimensions. The dimensions in the upper row are the constructed lengths and angles, the dimensions in the lower row are the traditional measurements.

the corresponding triangles. The edge lengths can be precisely measured by vernier caliper, since the feature points are selected from well-defined anatomical landmarks. Figure 3.20 shows the reconstructions by the selected dimensions. The first row shows the shapes reconstructed by the expert selected dimensions, the second row shows the shapes reconstructed by the dimensions selected from the combined pool. It can be seen that the shapes reconstructed by the dimensions selected from the combined pool by Algorithm 2 have smaller surface deviations.

Figure 3.21 shows the errors of shape reconstructions of the 216 testing shapes by the dimensions selected from the combined pool $\mathbb{P}$ by Algorithm 2. It could be seen that the reconstruction error deceases linearly as the number of dimensions increases, and is much smaller than the errors in Figure 3.17, where the dimensions are only selected from the traditional list.

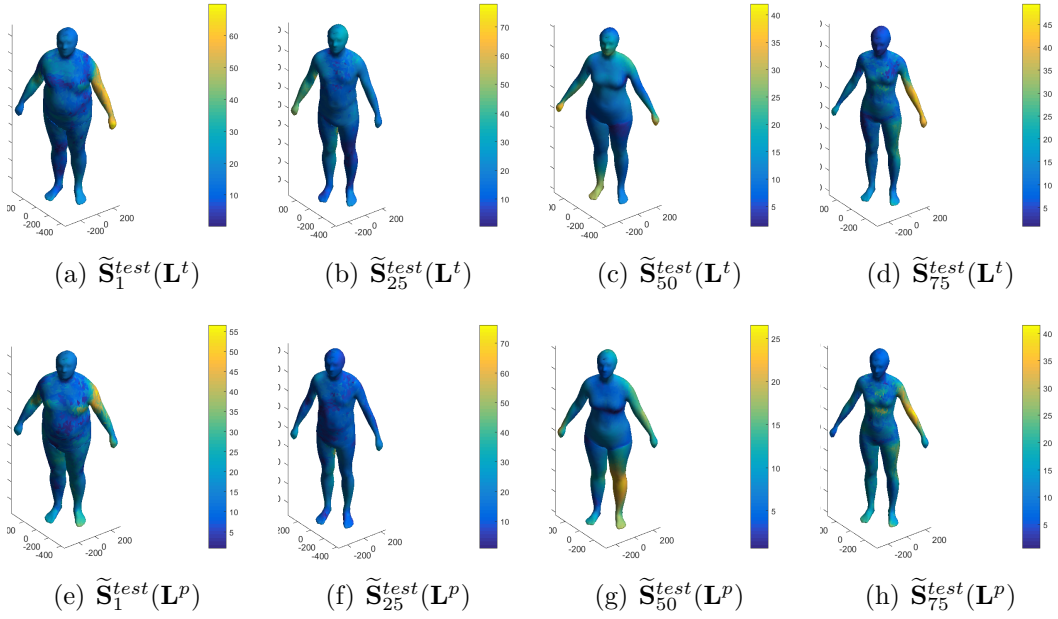

(a) $\widetilde{\mathbf{S}}_1^{test}(\mathbf{L}^t)$ (b) $\widetilde{\mathbf{S}}_{25}^{test}(\mathbf{L}^t)$ (c) $\widetilde{\mathbf{S}}_{50}^{test}(\mathbf{L}^t)$ (d) $\widetilde{\mathbf{S}}_{75}^{test}(\mathbf{L}^t)$

(e) $\widetilde{\mathbf{S}}_1^{test}(\mathbf{L}^p)$ (f) $\widetilde{\mathbf{S}}_{25}^{test}(\mathbf{L}^p)$ (g) $\widetilde{\mathbf{S}}_{50}^{test}(\mathbf{L}^p)$ (h) $\widetilde{\mathbf{S}}_{75}^{test}(\mathbf{L}^p)$

Figure 3.20: Shape reconstruction by the selected dimensions. The first row shows the shapes reconstructed by the expert selected dimensions $\mathbf{L}^t$, the second row shows the shapes reconstructed by the dimensions selected from the combined pool $\mathbf{L}^p$.

Figure 3.22 shows the confidence region of the conditional distributions of the shape parameters. It can be seen that as the number of dimensions increases, the areas of the confidence regions of both $p(w_1, w_2|\mathbf{L})$ and $p(w_3, w_4|\mathbf{L})$ decrease obviously, which means that the information provided by the additional dimensions can effectively localize the shape parameters, including the third and fourth shape parameter, of the unknown testing shape. That demonstrates the necessity and effectiveness of the new dimensions constructed by the feature points.

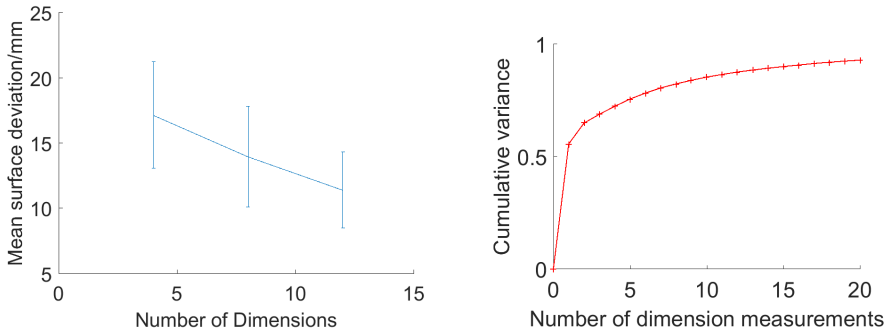

(a) Mean surface deviation (b) Cumulative variance

Figure 3.21: Dimension selection from the combined pool by Algorithm 2: (a) the mean surface deviations of shape reconstructions with different number of dimensions, (b) the percentage variance in the training shapes captured by the increasing number of dimensions.

3.5.2 The rabbit tibia example

The rabbit tibia models are used to demonstrate shape classification by sparse measurements. The database is come from [64]. As show in Figure 3.23(a) there are 64 rabbit tibias, among which 32 are normal tibias and 32 had surgery on the proximal part. The tibias are scanned 8 weeks after the surgery. It is know from [64] that the surgery do affect the growth of the rabbit tibias. In this study we want to extract the dimensions on the tibia shape that can effectively distinguish the surgical tibias and the normal tibias. The selected dimensions will be used in future studies of surgical effects since it can effectively capture the shape differences caused by the surgery.

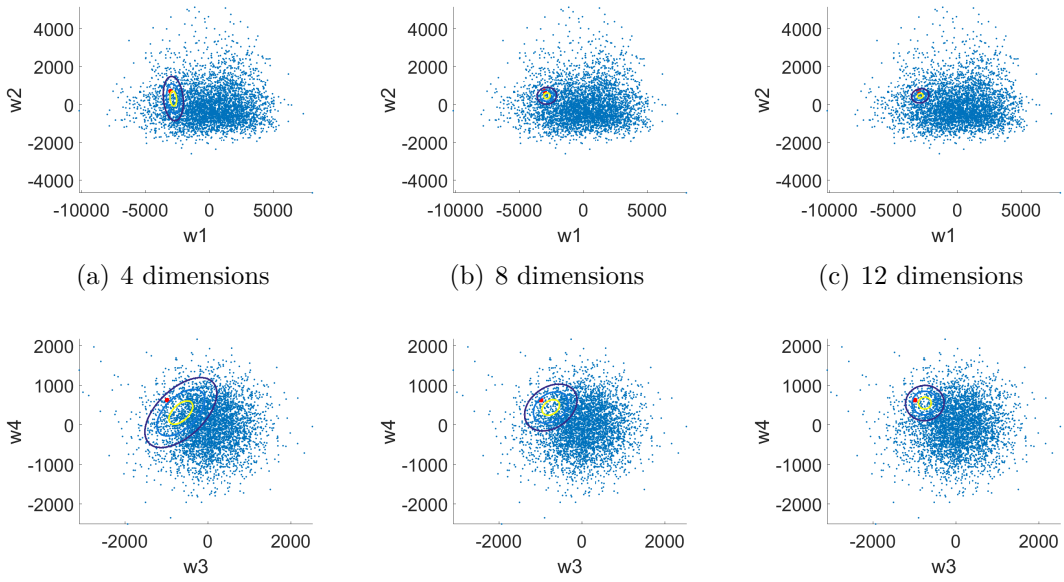

(a) 4 dimensions (b) 8 dimensions (c) 12 dimensions

(d) 4 dimensions (e) 8 dimensions (f) 12 dimensions

Figure 3.22: Confidence regions (66%, 90%, 99%) of the conditional distributions $p(w_1, w_2|\mathbf{L})$ (upper row) and $p(w_3, w_4|\mathbf{L})$ (bottom row). The red point shows the true shape parameter of the testing shape being investigated.

Statistical shape modeling

The statistical shape modeling is used to extract the population information of the rabbit tibias.

Figure 3.23(b) shows the aligned shapes and Figure 3.23(c) shows the mean shape of the population. Figure 3.24 shows the results of principal component analysis. It can be seen that the first mode is about the overall size change, the second mode is related to the thicken and elongation of the back of the tibia head, and the thrid mode is focused on some local shape changes. The paired student t-test is conducted for each shape parameter between the surgical and the normal tibias. The null hypothesis

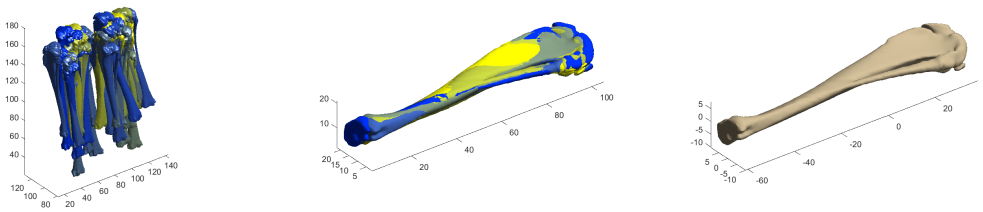

(a) 64 rabbbit tibias (b) Aligned shapes (c) Mean shape

Figure 3.23: Rabbit tibias: (a) the 64 traning shapes; (b) the aligned shapes; (c) the mean shape.

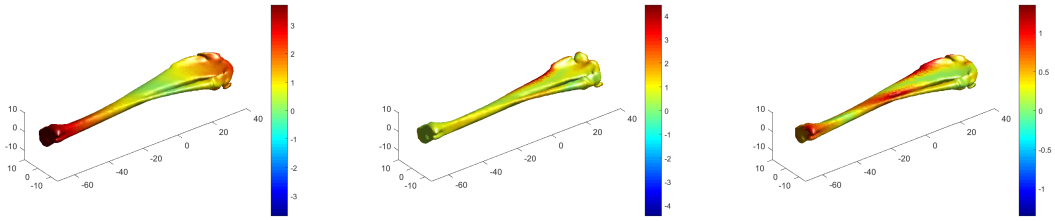

(a) +Mode 1 (b) +Mode 2 (c) +Mode 3

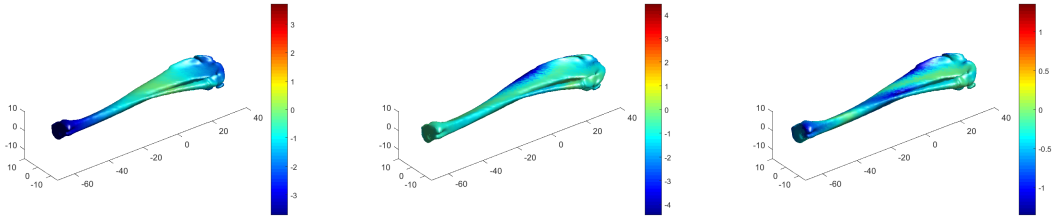

(d) -Mode 1 (e) -Mode 2 (f) -Mode 3

Figure 3.24: Statistical shape modeling of the rabbit tibias: the first three eigenmodes.

is that there's no difference between the surgical and normal tibias in terms of the shape parameters. The significance level is chosen at 0.05, and a p-value less than 0.05 means that the probability that the null hypothesis is true is less then 0.05.

By calculating the p-values of the 27 shape parameters we have $p_1 = 0.0045,\ p_2 =$

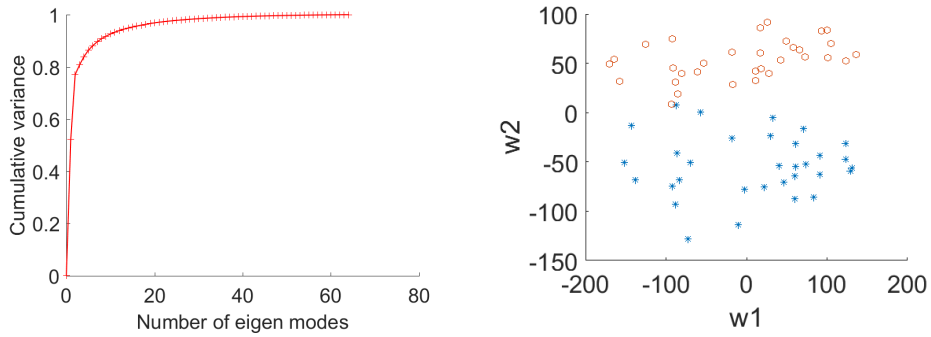

(a) Cumulative variance (b) Distribution of weights

Figure 3.25: Statistical shape modeling of the rabbit tibias: (a) the cumulative variance captured by the increasing number of eigenmodes; (b) the distribution of the first two shape parameters, $*$: normal, o: surgical.

0, $p_3 \cdots p_{27} > 0.05$, which means that the surgical and normal tibias differ along the first and second eigen-modes, which is in accordance with [64].

Figure 3.25(a) shows the variance of the shape population captured by the increasing number of eigenmodes. Figure 3.25(b) shows the distribution of the first two shape parameters. It can be seen that the first two shape parameters nicely distinguish the surgical and the normal tibias. However, in real clinical situations, it is very time consuming to obtain the full 3D shapes. Instead, we'd like to extract the dimensions related to the first two eigen-modes and can be measured efficiently in clinical settings.

Feature points identification

Firstly, the feature points that can capture the total variance in the shape population are extracted. Figure 3.26 shows the results of the feature points selection and the variance of the shape population captured by the increasing number of feature points.

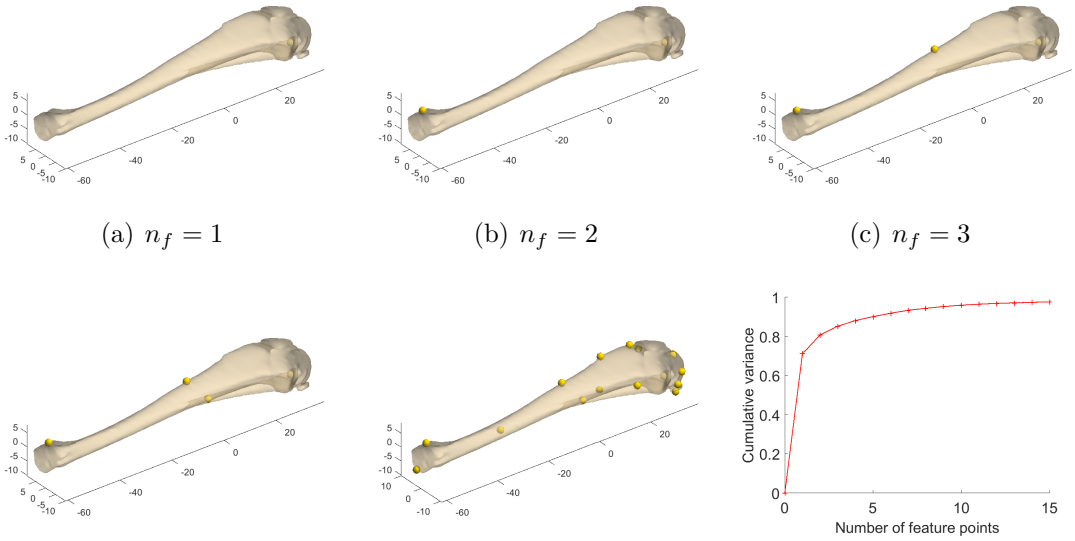

(a) $n_f = 1$ (b) $n_f = 2$ (c) $n_f = 3$

(d) $n_f = 4$ (e) $n_f = 15$ (f) Cumulative variance

Figure 3.26: Feature points selection: (a) - (e) the most important 15 feature points selected by Algorithm 1; (f) the cumulative variance captured by the increasing number of feature points.

Dimension construction and selection

Based on the selected feature points, $C_{15}^2 = 105$ lengths and $3C_{15}^3 = 1365$ angles are constructed. The dimension pool contains 1470 dimensions

$$\mathbb{P} = \{l_1, l_2, \cdots, l_{1470}\}.$$

The conditional variance of the distribution $p(w_1, w_2|\mathbf{L})$ is used to select the dimensions, as in equation (3.27). Since we only care about how much variance in w_1, w_2 are captured by the selected dimensions, where w_1, w_2 are the shape parameters that relevant to the surgical effects.

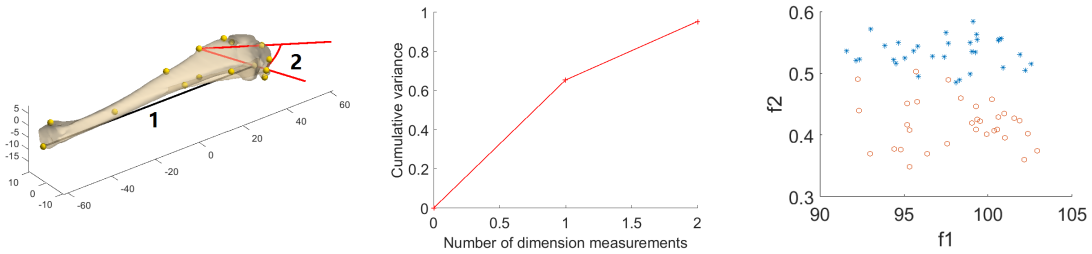

(a) Dimension selection & ranking (b) Cumulative variance (c) Distribution of f_1, f_2

Figure 3.27: Dimension selection: (a) the 2 dimensions that are most relevant to the surgical effects; (b) the variance in the first shape parameters w_1, w_2 captured by the increasing number of dimensions; (c) the distribution of the selected dimensions over the 64 tibias. $*$: normal, o: surgical.

The selected dimensions is shown in Figure 3.27. The rank of the selected dimensions is shown by the number in Figure 3.27(a). The percentage variance of the shape parameters w_1, w_2 captured by the increasing number of dimensions is shown in Figure 3.27(b). The distribution of the selected diemnsions over the groups is shown in Figure 3.27(c). It can be seen that the selected dimensions are powerful in distinguish the control and surgical tibias compared with merely using the overall length as in [64]. The surgical shapes have smaller angles (l_2) compared with the control shapes. The selected angle have successfully captured the variation of the second mode, which is very important in distinguishing the two groups of shapes.

Figure 3.28 shows the dimensions on the control shape and on the corresponding surgical shape. It can be seen that the back of the head of the surgical shape has been thickened and elongated, so the corresponding triangle is also elongated and thus the angle becomes smaller.

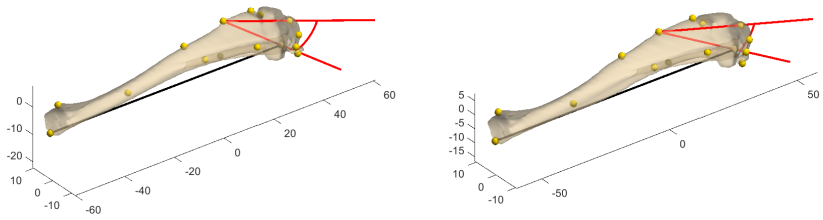

(a) Control (b) Surgical

Figure 3.28: Comparing the sizing dimensions on: (a) the control shape; (b) the surgical shape.

4

A statistical atlas based approach for automated shape registration and finite element modeling

The ability of in-time prediction of subject-specific structural performance from the given subject-specific shape model is critical in clinical setting such as surgical planning, surgical guidance during surgery, patient-specific biomedical intervention and treatment [6; 9]. However, how to automatically create high-quality finite element (FE) mesh remains challenging.

This chapter[1] presents a statistical atlas based approach for automatic meshing of subject-specific shapes. In our approach, shape variations among a shape population are explicitly modeled and the correspondence between a given subject-specific shape and the statistical atlas are sought within the "legal" shape variations. This approach involves three parts: 1) constructing a statistical atlas from a shape population, including the statistical shape model and the FE mesh of the mean shape; 2) es-

[1]This chapter is based on the following paper: Xilu Wang, Xiaoping Qian, "A statistical atlas based approach to automated subject-specific FE modeling", Computer-Aided Design 70 (2016): 67-77.

tablishing the correspondence between a given subject shape and the atlas; and 3) deforming the atlas to the subject shape based on the shape correspondence.

Numerical results on 2D hands, 3D femur bones and 3D aorta demonstrate the effectiveness of the proposed approach.

4.1 Method overview

The goal of this work is to present an approach that can automatically build subject-specific FE models from a given subject-specific shape.

In the literature, a common approach to efficient shape modeling or FE modeling of subject-specific objects is through template-based deformation, which contains two steps: 1) registration of the subject shape to the template shape; 2) FE mesh morphing of the template mesh to the subject with the correspondence obtained in the registration. However, the above approach is unaware of the specificity of the subject shapes and have the issues of: 1) too many variables to control the registration; 2) lack of robustness; 3) manually dependent.

For a certain class of shapes, the shape variations always follow some particular patterns, and the deformations within the class are really constrained by a limited number of degrees of freedom. Thus, for the FE mesh construction of a specific class of subject shapes, we first learn a prior knowledge of the population through statistical shape modeling [40] and build a linear space of shapes. Then, instead of applying a "free style deformation" in the registration, the mean shape of the population is deformed in the "shape space" to match the subject-specific shape. In

this way the deformation could be parameterized by just a few number of variables and becomes simple and robust. The generic FE mesh is built upon the mean shape of the population.

Figure 4.1 gives an overview of our approach: the input is the subject specific shape, the output is the FE mesh of the subject shape. This mesh construction process is based on the statistical atlas and contains two steps: 1) boundary correspondence identification through shape instantiation and projection; 2) FE mesh morphing by the boundary correspondence.

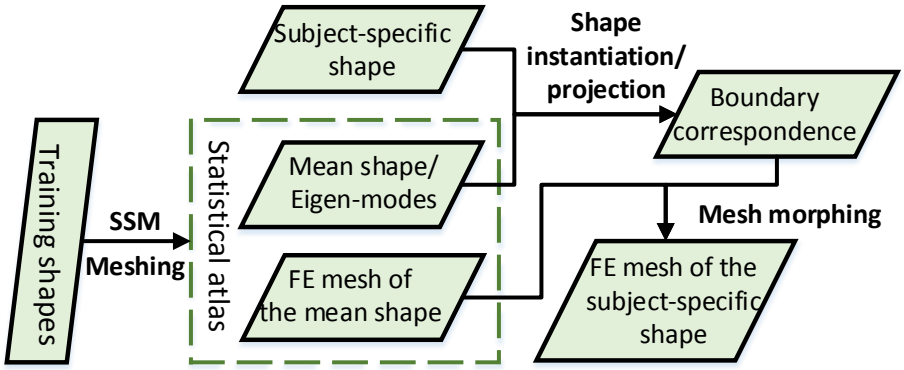

Figure 4.1: A schematic diagram of the statistical atlas based subject-specific FE modeling.

The statistical atlas contains two parts: the statistical shape model which defines a linear shape space and the FE mesh of the mean shape.

The statistical shape model is learned from a population of shapes by principal component analysis, and includes the mean shape $\bar{\mathbf{S}}$ of the population and the eigen-modes $\{\Psi_i\}$ that capture the variations of the population. Originated at the mean shape, the eigen-modes together span a linear shape space Θ and any instance in

that space can be instantiated by:

$$\widetilde{\mathbf{S}} = \bar{\mathbf{S}} + \sum_i w_i \Psi_i,$$

where $\{w_i\}$ are the shape parameters.

In the step of correspondence identification, the mean shape is deformed to the subject shape along a path in the shape space by optimizing the shape parameters $\{w_i\}$ and is then projected onto the subject shape to establish the boundary correspondence between the mean shape and the subject shape.

Based on the obtained boundary correspondence, the FE mesh of the mean shape is then morphed to the subject shape through free-form deformation.

The contribution of this work is a new approach that can automatically, efficiently and robustly produce high quality FE meshes for given subject-specific shapes. To examine the quality of the proposed approach, we use three measures: the distance between the instantiated shape and the given shape, the correlation coefficient of normal vectors between the mean shape and the given shape, and the mesh quality. Numerical examples on 2D hands, 3D femur bones and 3D aorta demonstrate that the proposed approach outperforms the simple deformation based approach.

The remainder of this work is organized as follows. Section 2 introduces the construction of statistical atlas, section 3, 4 covers the two steps of the proposed approach, section 5 introduces the three measures for our approach. Numerical results are presented in Section 7.

4.2 Constructing statistical atlas

The statistical atlas is constructed to incorporate the prior knowledge of a specific class of shapes and provide a generic FE mesh for mesh morphing. The prior knowledge are learned by the statistical shape modeling of a population of training shapes. The generic FE mesh is constructed on the population mean whose overall distance to other instances in the population is minimized.

In this section we briefly introduce the process of statistical atlas construction. The 40 hand shapes in [40] are used as examples to demonstrate the process.

Given the set of training shapes $\{\mathbf{S}_1, \cdots, \mathbf{S}_{n_s}\}$ registered by the iterative free-form deformation approach in chapter 2 and re-sampled by the same number of points in correspondences:

$$\mathbf{S}_k = [\mathbf{v}_1^{(k)}, \cdots, \mathbf{v}_{n_v}^{(k)}]^T, \ k = 1, \cdots, n_s. \tag{4.1}$$

Generalized Procrustes analysis [61] is used to align the shapes into the same coordinate frame and then principal component analysis is applied to obtain the mean shape $\overline{\mathbf{S}}$ and eigen-shapes $\mathbf{\Psi} = [\boldsymbol{\psi}_1, \cdots, \boldsymbol{\psi}_{n_s-1}]$ of the population. The first m number of eigen-shapes are chosen such that 99% of the variances in the shape population is captured $\sum_{k=1}^{m} \lambda_k / \sum_{k=1}^{n_s-1} \lambda_k \geq 99\%$. In this case we have $m = 11$. The mean shape and the first m eigen-shapes give a compact representation of the shape population:

$$\mathbf{S} = \overline{\mathbf{S}} + \sum_{k=1}^{m} w_k \mathbf{\Psi}_k, \tag{4.2}$$

where $\mathbf{w} = [w_1, \cdots, w_m]^T$ are the shape parameters. The shape space spanned by the chosen m eigen-modes are called the eigen-space.

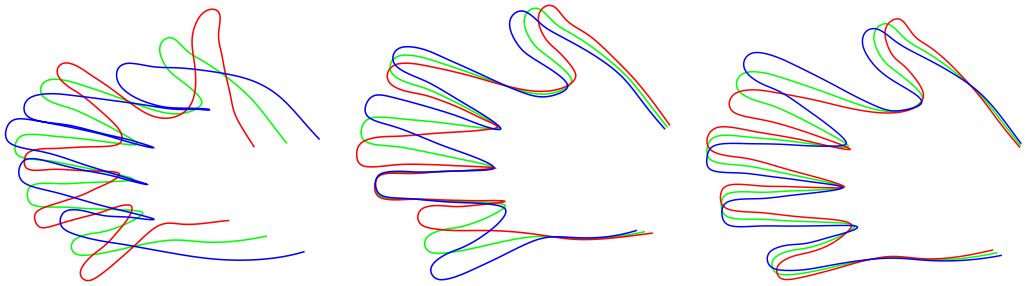

(a) $\bar{\mathbf{S}} \pm 2\sigma_1 \mathbf{V}_1$ (b) $\bar{\mathbf{S}} \pm 2\sigma_2 \mathbf{V}_2$ (c) $\bar{\mathbf{S}} \pm 2\sigma_3 \mathbf{V}_3$

Figure 4.2: The first three eigen-modes of the shapes. Green one is the mean shape, red is the $+2\sigma$ deviation and blue is the -2σ deviation.

Figure 4.2 shows the first three eigen-modes of the hand shapes obtained by principal component analysis.

In Figure 2.7 we show the cumulative shape variances. In which the first 8 modes have captured 98.14% of the shape variances and the first 11 modes have captured 99.01% of the shape variances.

On the mean shape $\overline{\mathbf{S}}$ of the training populations, we manually create a generic FE mesh by ANSYS. This generic FE mesh will be used as a template to create subject-specific FE meshes.

Figure 4.3 shows the quadrilateral mesh of the mean shape of the 40 hands in chapter 2, the color shows the value of Jacobians, which are all positive.

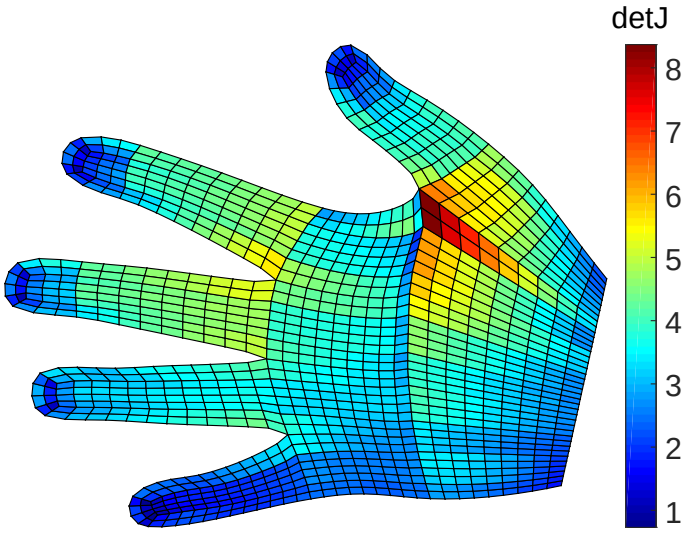

Figure 4.3: The quadrilateral mesh of the mean shape $\bar{\mathbf{S}}$ and the Jacobians.

4.3 Shape instantiation and projection

By statistical shape modeling, we obtain the mean shape $\bar{\mathbf{S}}$ and the eigen-modes $\Psi_1, \Psi_2, \cdots, \Psi_{n_s-1}$ of the training populations. The eigen-modes capture the shape variations and together span a linear shape space. By choosing the first m eigen-modes corresponding to the major shape variations as described in 4.2, we obtain the eigen-space Θ, and an instance in it can be instantiated by $\widetilde{\mathbf{S}} = \bar{\mathbf{S}} + \sum_{k=1}^{m} w_k \boldsymbol{\Psi}_k$, where $\mathbf{w} = [w_1, w_2, \cdots, w_m]^T$ are the shape parameters.

Given a new shape $\hat{\mathbf{S}}$, we search in the eigen-space to find the optimal shape parameters $\mathbf{w}$ that best synthesize it and obtain the optimal shape instance $\widetilde{\mathbf{S}}$ in Θ for $\hat{\mathbf{S}}$. Then we project the points of $\widetilde{\mathbf{S}}$ onto $\hat{\mathbf{S}}$ along the normal vectors of $\widetilde{\mathbf{S}}$ so to obtain the finally synthesized shape $\widetilde{\mathbf{S}}^P$, from which the point-wise correspondences between the given shape and the atlas can be established.

During the eigen-space search, the instantiated shape $\widetilde{\mathbf{S}}$ is in the reference frame of Θ, while $\hat{\mathbf{S}}$ locates in the image frame or the corresponding physical frame if it is obtained by point scanning. and we denote the transformation from the reference frame to the physical frame as $\mathbf{t}_{R,T,s}$ with parameters R, T, s, where R is the rotation, T is the translation and s is the scaling. For a point $\mathbf{p}$, $\mathbf{t}_{R,T,s}(\mathbf{p}) = sR\mathbf{p} + T$. In our later expression, we use $\mathbf{t}_{R,T,s} \circ \mathbf{S}$ to denote the transformation of a shape under $\mathbf{t}_{R,T,s}$ point-wisely.

Similar with the free-form deformation, we search for the optimal shape parameters and transformation by minimizing the distances between the given shape $\hat{\mathbf{S}}$ and the instantiated shape $\widetilde{\mathbf{S}}$. A regularization term is added to stabilize the optimization. The total energy function is:

$$\min_{R,T,s,\mathbf{w}} \; E = E_d + \gamma E_r, \tag{4.3}$$

where E_d is the distance term and E_r is the regularization term similar as E_{smooth} in the free-form deformation. Large regularization coefficient γ will give strong penalizations to large shape parameters $\mathbf{w}$ when compared with the square roots of the eigen-values $\sigma_k = \sqrt{\lambda_k}, k = 1, \cdots, m$. We have

$$E_d = \|\hat{\mathbf{S}}^c - \mathbf{t}_{R,T,s} \circ (\bar{\mathbf{S}} + \Psi\mathbf{w})\|^2, \tag{4.4}$$

captures the discrepancies between the given shape $\hat{\mathbf{S}}$ and the instantiated shape $\widetilde{\mathbf{S}} = \bar{\mathbf{S}} + \Psi\mathbf{w}$, where $\Psi = [\Psi_1, \Psi_2, \cdots, \Psi_m]$, and $\hat{\mathbf{S}}^c$ is the re-sampling of $\hat{\mathbf{S}}$ based on

the correspondence. We have

$$E_r = \mathbf{w}^T \Lambda^{-1} \mathbf{w}, \tag{4.5}$$

as the regularization term, where $\Lambda = \text{diag}(\sigma_1^2, \cdots, \sigma_m^2)$ is the diagonal matrix of the eigen-values. The regularization term represents our prior belief about the shape parameters. The values beyond the standard deviation σ_i of the corresponding shape parameter σ_i are less likely to happen.

Similar to the non-rigid registration algorithm in [47; 46; 45], we choose large initial regularization coefficient γ and reduce it gradually. So at the beginning, more global transformations are recovered by R, T, s and as γ is reduced, major shape variations are recovered by the parameters corresponding to larger eigen-values, and as γ keep reducing, local fine shape variations are recovered as the parameters corresponding to smaller eigen-values being effective in (4.3).

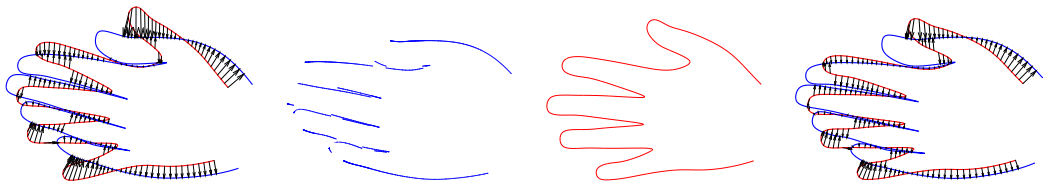

(a) Searching: red $\widetilde{\mathbf{S}}$, blue $\hat{\mathbf{S}}$ (b) re-sampling: $\hat{\mathbf{S}}^c$ (c) Instantiation: $\widetilde{\mathbf{S}}$ (d) Searching

Figure 4.4: The iterative shape instantiation from a given shape: (a) the correspondence between the instantiated shape $\mathbf{t}_{R,T,s} \circ \widetilde{\mathbf{S}}$ and the given shape $\hat{\mathbf{S}}$ is obtained by searching the closest point; (b) the re-sampling $\hat{\mathbf{S}}^c$ of $\hat{\mathbf{S}}$ is obtained with the current correspondence; (c) a newly instantiated and transformed shape is obtained by minimizing (4.3) with the current $\hat{\mathbf{S}}^c$; (d) updating the correspondence by the newly instantiated shape and iterate.

The shape instantiation is done through an iterative process as shown in Figure 4.4, in which the correspondence and the parameters $\mathbf{w}, R, T, s$ are optimized iteratively.

Starting from the mean shape $\bar{\mathbf{S}}$, we build the correspondence between $\bar{\mathbf{S}}$ and the given shape $\hat{\mathbf{S}}$ by searching the closest points. Based on the correspondence, we re-sample $\hat{\mathbf{S}}$ and obtain $\hat{\mathbf{S}}^c$, with which we search for the optimal shape parameters $\mathbf{w}$ and transformation R, T, s by minimize (4.3). After that we instantiate a shape instance by $\widetilde{\mathbf{S}} = \bar{\mathbf{S}} + \mathbf{\Psi}\mathbf{w}$ and transform it to the frame of $\hat{\mathbf{S}}$ by $\mathbf{t}_{R,T,s} \circ \widetilde{\mathbf{S}}$. Then we update the correspondence with the newly instantiated shape and iterate until (4.3) convergence to a local minimum. With fixed value of γ, equation (4.3) is guaranteed to converge to a local minimum, since each step reduces E. The correspondence is updated by the closest points, so E_d is reduced while E_r remains the same. Based on the obtained correspondence, optimal R, T, s and $\mathbf{w}$ are solved so E is reduced.

With known correspondence and the re-sampled points $\hat{\mathbf{S}}^c$, formula (4.3) is minimized through iteratively optimizing the shape parameters $\mathbf{w}$ and the transformation R, T, s by applying the Protocol 1 (Matching model points to target points) of the active shape algorithm in [49], which was originally used for image segmentation in [49; 42]. The difference is that in image segmentation, the shape $\widetilde{\mathbf{S}}$ evolves in the image domain and the domain information (e.g. nearby pixel values, gradient information) can be utilized to find the best match. In [49] the values of nearby pixels along the gradient is utilized to match the instantiated shape $\widetilde{\mathbf{S}}$ and the target shape $\hat{\mathbf{S}}$ in image domain. However, in this paper the goal is to find the point correspondences between two shapes represented by point sets, which is essentially a discrete problem [48], the best match of $\widetilde{\mathbf{S}}$ on $\hat{\mathbf{S}}$ is obtained by the closest points. Based on the closest points

sampling $\hat{\mathbf{S}}^c$, the optimal parameters $\mathbf{w}, R, T, s$ are updated. In order to stabilize the matching process, the regularization term is added thus by letting $\frac{\partial E}{\partial \mathbf{w}} = 0$, we have

$$\mathbf{w} = (\mathrm{I} + \frac{\gamma}{s^2}\Lambda^{-1})^{-1}\Psi^T(\mathbf{t}_{R,T,s}^{-1} \circ \hat{\mathbf{S}}^c - \overline{\mathbf{S}}), \tag{4.6}$$

where $\mathbf{t}_{R,T,s}^{-1}$ is the inverse transformation of $\mathbf{t}_{R,T,s}$, I is the $m \times m$ identity matrix. When $\gamma = 0$, we have $\mathbf{w} = \Psi^T(\mathbf{t}_{R,T,s}^{-1} \circ \hat{\mathbf{S}}^c - \bar{\mathbf{S}})$ as in [49].

The below Algorithm gives a detailed description of our approach:

Algorithm 1 Automatic shape synthesis by SSM

- Initialize: $\widetilde{\mathbf{S}} = \bar{\mathbf{S}}$, $R = \mathrm{I}, T = 0, s = 1$, I is the $m \times m$ identity matrix.
- For each regularization coefficient $\gamma \in \{\gamma_1, \cdots, \gamma_n\}$, $\gamma_i > \gamma_{i+1}$.
  - Until $\|\Delta \mathbf{w}\| < \varepsilon$
    1. Find the correspondence by the closest points of $\mathbf{t}_{R,T,s} \circ \widetilde{\mathbf{S}}$ in $\hat{\mathbf{S}}$;
    2. Determine the parameters $\mathbf{w}, R, T, s$ by (4.3) for the current correspondence and γ;
    3. Instantiate the shape by $\widetilde{\mathbf{S}} = \bar{\mathbf{S}} + \mathbf{\Psi w}$ and transform it to the subject frame by $\mathbf{t}_{R,T,s}$.
  - If the correspondence does not change, exit the main loop.
- Project the final instance $\mathbf{t}_{R,T,s} \circ \widetilde{\mathbf{S}}$ onto $\hat{\mathbf{S}}$ along the normal and obtain $\widetilde{\mathbf{S}}^P$, exit.

The inputs for Algorithm 1 are the mean shape $\bar{\mathbf{S}}$, the eigen-modes Ψ and the given shape $\hat{\mathbf{S}}$ for synthesis; the output is the finally synthesized shape $\widetilde{\mathbf{S}}^P$. With the initialization, we start from the mean shape and deform it to the given shape through successive shape instantiations.

In the outer loop, under the current regularization coefficient γ, we found the

optimal correspondence, shape parameters $\mathbf{w}$ and transformations R, T, s for the given shape $\hat{\mathbf{S}}$ which respect to (4.3). Then we reduce the regularization coefficient γ, and use the current parameters as the initial input and optimize. If the correspondence does not change any more, we exit the outer loop otherwise we go to γ_n.

In the inner loop, we find the optimal parameters for the current γ by iteratively optimize the correspondence and the parameters $\mathbf{w}, R, T, s$. The convergence criteria for the inner loop is that the 2-norm of the change of the shape parameters $\|\Delta\mathbf{w}\|^2$ is smaller than $\varepsilon = 10^{-6} \times$ total shape variance.

Once the correspondence is not changing, we project $\mathbf{t}_{R,T,s} \circ \widetilde{\mathbf{S}}$ onto $\hat{\mathbf{S}}$ along the normal and obtain the optimal shape synthesis $\widetilde{\mathbf{S}}^P$ for $\hat{\mathbf{S}}$, by which we obtain the one-to-one correspondences between the mean shape $\bar{\mathbf{S}}$ and the given shape $\hat{\mathbf{S}}$ as a by product.

It is worth mentioning that without the regularization term E_r, the algorithm converges slowly and often converges to bad local minimums (e.g. with some shape parameter larger than 10 $\times$ the standard deviation). With the regularization term and starting with large penalization coefficient γ, the algorithm converges in a few hundreds of iterations and $\widetilde{\mathbf{S}}$ is deformed closely to $\hat{\mathbf{S}}$. In [49] shape parameters larger than three standard deviations are truncated at three standard deviations. It works in image segmentation, but in our experiments in correspondence finding, oscillations at observed since in this case the objective function E is not guaranteed to be reduced at every step.

4.4 Meshing subject-specific shape by morphing

In section 4.3 we have shown how to automatically register the subject shape $\hat{\mathbf{S}}$ to the mean shape $\bar{\mathbf{S}}$ by the shape instantiation and projection. As a byproduct, we obtain the transformation $\mathbf{t}_{R,T,s}$ from the reference frame to the frame of $\hat{\mathbf{S}}$, by its inverse $\mathbf{t}_{R,T,s}^{-1}$ we transform the subject shape $\hat{\mathbf{S}}$ to the reference frame where the mean shape locates. Then with the explicit correspondences between the boundaries of $\hat{\mathbf{S}}$ and $\bar{\mathbf{S}}$, we obtain a smooth deformation field that morphs the mesh of $\bar{\mathbf{S}}$ to $\hat{\mathbf{S}}$ by

$$\min_{\{\mathbf{P_i}\}} \sum_{j=1}^{N} \|\mathbf{f}(\overline{\mathbf{p}}_j) - \hat{\mathbf{p}}_j\|^2 + \alpha E_{smooth}, \tag{4.7}$$

where $\mathbf{f}$ is the B-spline field defined in (2.3), $\mathbf{P_i}, \mathbf{i} \in \mathcal{I}$ are its control points. $\overline{\mathbf{p}}_j, j \in 1, \cdots, N$ is the point on the mean shape $\bar{\mathbf{S}}$, and $\hat{\mathbf{p}}_j$ is its corresponding point on $\hat{\mathbf{S}}$ obtained by the shape instantiation and projection. The smoothing term E_{smooth} is the same as in section 2.2.2 and α is the smoothing coefficient. Here since we know the right correspondences, a small α that balances the magnitudes of the first term and second term in (4.7) is enough: in this we choose case $\alpha = 50$. Note that in pairwise registration in 2.2.2, we begin with $\alpha = 30,000$, such that the smooth term αE_{smooth} is thousands times more sensitive to the position change of the control points than the distance term, thus initially only rigid transformations are allowed, any distortion in the Bspline field will be amplified and be prevented. With the obtained deformation field $\mathbf{f}$, we morph the FE mesh of $\bar{\mathbf{S}}$ to $\hat{\mathbf{S}}$.

Figure 4.5 shows the correspondence obtained by the method of section 4.3 and the resulting FE mesh from mesh morphing with the correspondence. The Jacobians

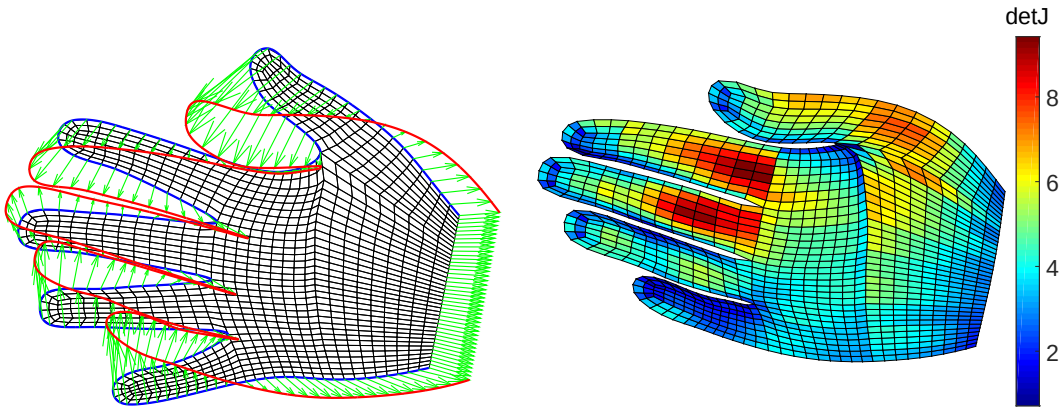

(a) Correspondence (b) Morphed FE mesh

Figure 4.5: Meshing subject-specific shape by morphing: (a) The correspondence between $\bar{\mathbf{S}}$ and $\hat{\mathbf{S}}$; (b) results of FE mesh morphing.

in Figure 4.5(b) are all positive which means the mesh is valid.

4.5 Evaluation

To examine the quality of the proposed approach, we use three measures: the distance between the instantiated shape and the given shape, and correlation of normal vectors between the mean shape and the given shape, and the Jacobians of the subject-specific mesh obtained.

4.5.1 Shape deviations

The distance between the instantiated shape and the given shape is calculated by (4.4) at the end of the instantiation to evaluate the quality of the shape instantiation. Small distance means that we find an instance in the eigen-space that is very close

to the given shape, thus by the projection we can build a reliable correspondence between them. Large distance means either the given shape is far from the eigen-space or the method has failed to instantiate the correct shape instance.

As long as the training shapes are homeomorphic, the instantiated shape $\tilde{\mathbf{S}}$ will be homeomorphic with large likelihood since it is instantiated in the shape space learned from the training shapes. Our observations show that invalid shape instances occur only when we extrapolate too far from the mean shape (beyond three or even four standard deviations). However, in reality the chances that we observe data beyond three or four standard deviations are rare. In normal distribution, only 0.27% of the data are beyond three standard deviations, and 0.006% of the data are beyond four standard deviations.

4.5.2 Correlation of normal vectors

The correlation of the normal vectors at the corresponding points between the mean shape and the given shape is calculated to quantize the quality of the correspondence.

For two random variables x and y, their correlation coefficient

$$\rho(x,y) = \frac{\mathrm{Cov}(x,y)}{\mathrm{Cov}(x,x)^{\frac{1}{2}}\mathrm{Cov}(y,y)^{\frac{1}{2}}}, \tag{4.8}$$

measures the similarity in behavior between x and y, here $\mathrm{Cov}(x,y)$ is the covariance between x and y. The square of the correlation coefficient $\rho^2(x,y)$ is the proportion of the total variation in x that is explained by the variable y in a simple linear regression model and visa versa [66].

For a random variable x and a d dimension random vector $\mathbf{Y}$, the multiple correlation coefficient $\varrho(x, \mathbf{Y}) \in [0, 1]$ between them is defined as [67]

$$\sup_{\mathbf{A}} \ \varrho^2(x, \mathbf{Y}) = \rho^2(x, \mathbf{AY}), \tag{4.9}$$

where ρ is defined in (4.8). It turns out that $\mathbf{A} = \Sigma_{12}\Sigma_{22}^{-1}$ is the vector of regression coefficients of x on $\mathbf{Y}$, where Σ_{12} is the covariance between x and $\mathbf{Y}$ whose dimensions are $1 \times d$, Σ_{22} is the covariance of $\mathbf{Y}$ itself and is a $d \times d$ matrix. So by (4.8) and (4.9) we have [67]

$$\varrho(x, \mathbf{Y}) = \sqrt{\Sigma_{12}\Sigma_{22}^{-1}\Sigma_{21}}/\sqrt{\sigma_{11}}, \tag{4.10}$$

where σ_{11} is the variance of x, $\Sigma_{21} = \Sigma_{12}^T$. Similarly, $\varrho^2(x, \mathbf{Y})$ is the proportion of the variation in x that is explained by the variables in $\mathbf{Y}$ by linear regression with the regression coefficients $\mathbf{A} = \Sigma_{12}\Sigma_{22}^{-1}$.

For two random vectors $\mathbf{X}_{d_1 \times 1}$ and $\mathbf{Y}_{d_2 \times 1}$, for each individual component $x_i, i = 1, \cdots, d_1$ of $\mathbf{X}$, we calculate its multiple correlation with $\mathbf{Y}$ and obtain $\mathbf{r} = [\varrho_1, \cdots, \varrho_{d_1}]^T$ by (4.10), while ϱ_i^2 is the proportion of variation in x_i that is explained by $\mathbf{Y}$ by linear regression. Thus the total proportion of variation in $\mathbf{X}$ that is explained by $\mathbf{Y}$ can be calculated by $\sum_{i=1}^{d_1} \varrho_i^2\sigma_{ii} / \sum_{i=1}^{d_1} \sigma_{ii}$, where σ_{ii} is the variance of x_i, and $\sum_{i=1}^{d_1} \sigma_{ii}$ is the total variation in $\mathbf{X}$, and $\sum_{i=1}^{d_1} \varrho_i^2\sigma_{ii}$ is the variation of $\mathbf{X}$ being explained by $\mathbf{Y}$ by linear regression.

We define

$$\varrho(\mathbf{X}, \mathbf{Y}) = \sqrt{\sum_{i=1}^{d_1} \varrho_i^2 \sigma_{ii} / \sum_{i=1}^{d_1} \sigma_{ii}}, \tag{4.11}$$

be the correlation between $\mathbf{X}$ and $\mathbf{Y}$ and use it to calculate the correlation of normal vectors of two registered shapes. Note that $\varrho(\mathbf{X}, \mathbf{Y}) \in [0, 1]$, which achieves 1 if and only if $\mathbf{r} = [1, 1, \cdots, 1]^T$, and achieves 0 if and only if $\mathbf{r} = [0, 0, \cdots, 0]^T$. Below is the definition of what is a good correspondence when judged by this metric:

Definition: we say $c^a : \mathbf{S}_1 \to \mathbf{S}_2$ is a better correspondence than $c^b : \mathbf{S}_1 \to \mathbf{S}_2$ if

$$\varrho(\mathbf{n}_1(\mathbf{x}), \mathbf{n}_2(c^a(\mathbf{x}))) > \varrho(\mathbf{n}_1(\mathbf{x}), \mathbf{n}_2(c^b(\mathbf{x}))), \ \mathbf{x} \in \mathbf{S}_1, \tag{4.12}$$

where $\mathbf{n}_1(\mathbf{x})$ is the normal vector at the point $\mathbf{x}$ on $\mathbf{S}_1$, $\mathbf{n}_2(c^a(\mathbf{x}))$ the normal vector at the corresponding point of $\mathbf{x}$ on $\mathbf{S}_2$, and $\varrho(\mathbf{n}_1, \mathbf{n}_2)$ is defined in (4.11). The inequality (4.12) says that c^a is a better correspondence than c^b if it gives larger correlation between the normal vectors on $\mathbf{S}_1$ and $\mathbf{S}_2$.

4.5.3 Mesh quality metric

To check the quality of the morphed mesh for the subject-specific shape, we calculate the Jacobians at the vertices of each element. It can be shown that the Jacobians over a linear Bézier element (which degenerates to a linear Lagrange element) are bounded by the Jacobians at it's corners [68]. So, for the mesh of bi-linear 2D finite elements and tri-linear 3D finite elements, it is sufficient to check the Jacobians at the vertices of each element. For further discussions on the Jacobians

of higher order elements, please refer to [69; 70].

4.6 Numerical results

In the proposed approach in section 4.2 , 4.3, and 4.4, we build the statistical atlas from the population of training shapes and use it to aid the automatic construction of the subject-specific FE mesh. Then we evaluate the approach by the metrics proposed in section 4.5. Here we show the numerical results of the examples of the 2D hand shapes, 3D femur proximals and 3D aortas.

4.6.1 2D hand shapes

In this section we apply our method on the subject-specific FE modeling of the 2D hand shapes. We have 40 hand shapes in total and they are scaled and moved into the $[0, 1] \times [0, 1]$ bounding box. Each shape is represented by 2001 uniformly sampled points.

In the FFD registration, the shape $\mathbf{S}_{23}$ is chosen as the template shape and has been registered to the other training shapes by FFD. Then we re-sample all the other training shapes by the points on $\mathbf{S}_{23}$ with the correspondences obtained. The size of the B-spline control grid in this example is 20×20, the smoothing coefficient α is chosen to be 30000 at the start of the deformation and is halved per 8 iterations until $\alpha < 10$. We choose the weight of landmarks $\beta = 5$.

In Figure 2.5 and 4.2 we show the mean shape and eigen-modes calculated from the training set of all the 40 re-sampled shapes. Here we design a leave-one-out

experiment. For $k = 1, \cdots, 40$, each time the kth shape is selected as the subject shape and the remaining 39 shapes are used as the training shapes. The statistical shape model is built from the re-samplings of the 39 training shapes. In this way, the training set will not contain the exact subject shape.

In the shape instantiation, we use the first 11 eigen-modes (captures more than 99% of the variation) to instantiate the new shape. The regularization coefficient γ is chosen to be 0.3 initially and multiplied by $\frac{1}{4}$ each outer iteration in Algorithm 1 until it is less than 0.008. The rule of thumb is to choose the initial value of γ such that at the beginning only rigid transformations are allowed. Then γ is gradually decreased so to allow more and more shape changes. The final value of γ is chosen such that γE_r is an order of magnitude smaller than E_d (10 times smaller) so the shape deviations dominates the deformation at the end. In the FE mesh morphing, we choose the smoothing coefficient $\alpha = 50$ that balances the magnitudes of the distance term and smoothing term in (4.7).

The results of shape instantiation and FE mesh construction of shapes $\mathbf{S}_1, \mathbf{S}_{26}, \mathbf{S}_{37}$ are shown in Figure 4.6. Left column shows the results of shape instantiation and right column shows the results of FE mesh construction. In the FE mesh construction, the subject shapes were transformed to the reference frame by $\mathbf{t}_{R,T,s}^{-1}$.

Among the 40 shapes, only the instantiation of the shape $\mathbf{S}_{38}$ has failed, as shown in Figure 4.7(a). As mentioned in [40], $\mathbf{S}_{38}$ belongs to one of the two outliers $(\mathbf{S}_{38}, \mathbf{S}_{40})$ in the training set, which means it is much farther from the mean shape than other shapes, and is more likely to be trapped in the local minimum. We say that it is trapped in the local minimum because there does exist an instance $\widetilde{\mathbf{S}}_{38}$ in the

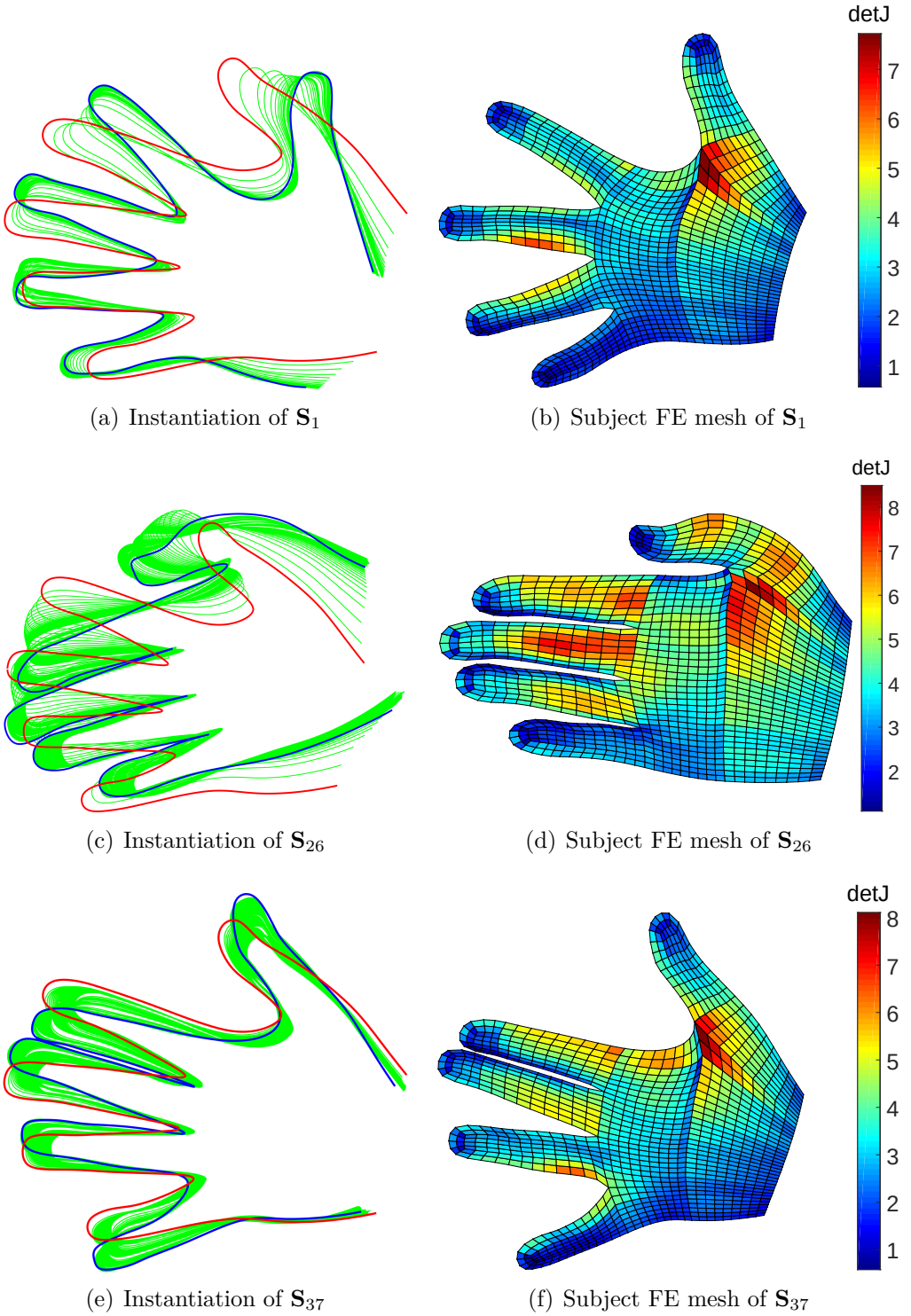

(a) Instantiation of $\mathbf{S}_1$ (b) Subject FE mesh of $\mathbf{S}_1$

(c) Instantiation of $\mathbf{S}_{26}$ (d) Subject FE mesh of $\mathbf{S}_{26}$

(e) Instantiation of $\mathbf{S}_{37}$ (f) Subject FE mesh of $\mathbf{S}_{37}$

Figure 4.6: The results of shape instantiation and subject FE mesh construction. In the left column, the red contour is the mean shape, the blue contour is the subject shape, the green contours are the locus of shape instantiation. The right column shows the subject FE mesh and the Jacobians. We could see that all the meshes have positive Jacobians.

eigen-space built from $\mathcal{S}^{(38)} = \{\mathbf{S}_1^c, \cdots, \mathbf{S}_{37}^c, S_{39}^c, S_{40}^c\}$ that is closer to $\mathbf{S}_{38}$ than the one we found, as shown in 4.7(b).

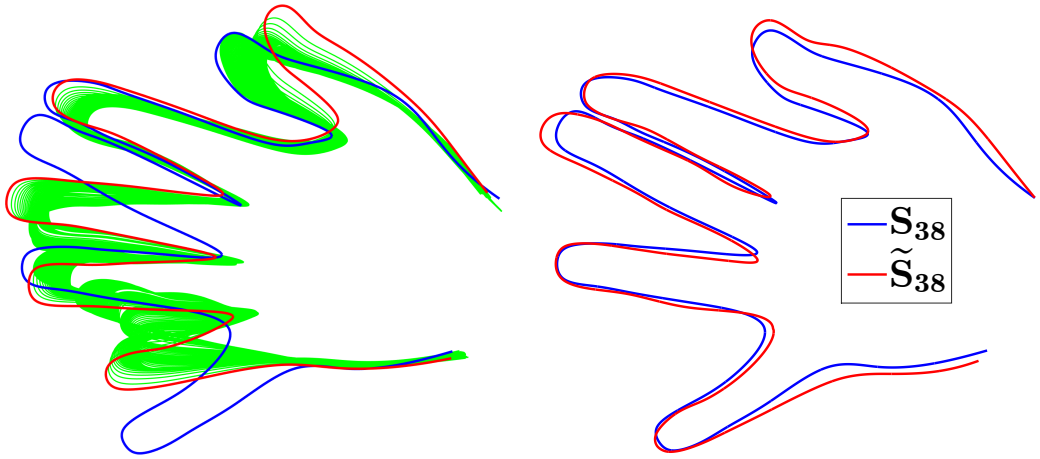

(a) Instantiation of $\mathbf{S}_{38}$ (b) The best match $\widetilde{\mathbf{S}}_{38}$

Figure 4.7: The algorithm has failed to correctly instantiate $\mathbf{S}_{38}$: (a) the locus of the instantiation, the mean shape is in red, $\mathbf{S}_{38}$ blue; (b) the best match for $\mathbf{S}_{38}$ in the eigen-space.

The best match of $\mathbf{S}_{38}$ is obtained by projecting $\mathbf{S}_{38}^c$ into the eigen-space by

$$\widetilde{\mathbf{S}}_{38} = \bar{\mathbf{S}} + \Psi\Psi^T(\mathbf{S}_{38}^c - \bar{\mathbf{S}}),$$

where $\mathbf{S}_{38}^c$ is the re-sampling of $\mathbf{S}_{38}$ with the correspondence obtained by FFD with 56 landmarks, $\bar{\mathbf{S}}$ is the mean shape of $\mathcal{S}^{(38)}$.

In all other examples of 3D femur and aorta there are no failure cases because the shapes are similar with each other.

Figure 4.8 shows the distance of the instantiated shape (E_d in section 4.3) to the given shape at each iterations. We could see most of the instantiations succeed in

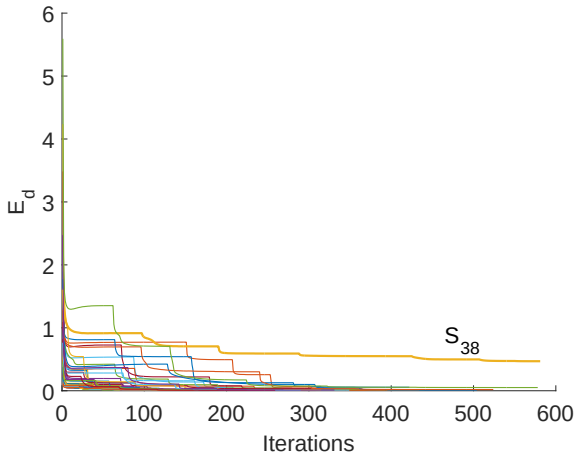

Figure 4.8: The value of E_d at each iteration. The bold green curve corresponds to $\mathbf{S}_{38}$.

finding an instance close to the given shape except for $\mathbf{S}_{38}$, which deviates too much from the mean shape. The running time is from 1.507530 seconds ($\mathbf{S}_{13}$, 168 iteration) to 5.910679 seconds ($\mathbf{S}_{38}$, 581 iterations) on Matlab with processor: Intel Core i7, 3.50GHz. Table 4.1 shows the detailed statistics.

Table 4.1: Performances (2D hands): on Matlab with Intel Core i7, 3.50 GHz

	Running time	**Iterations**	**Num. of pts**
minimum	1.51 s	168	2001
maximum	5.91 s	581	2001

In Figure 4.9 we plot the correlation coefficients of normals between the template shape and all other registered shapes before and after the free-form deformation, which are in triangles and squares, and the correlation coefficients obtained by the shape instantiation, which is in circle. We could see that the proposed correlation metric has nicely distinguished the registered shapes and unregistered shapes while show no

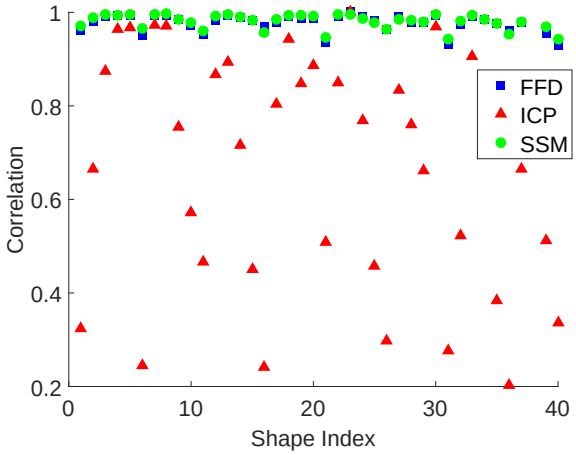

Figure 4.9: The correlation coefficient of normals. Here, we only calculate the correlation coefficients for the 39 successfully registered shapes.

major differences between the FFD and the shape instantiation, which indicates that the automatic shape registration by eigen-space search without manually intervention gives as good correspondence as the free form deformation method with carefully chosen landmarks. Actually, the 56 landmarks we used in the FFD based registration are the same landmarks used by [40].

4.6.2 3D femur proximals

The clinical diagnosis of femur proximal abnormal relies on the analysis of femur shapes, here we apply our method with the femur example to demonstrate its success in 3D shape synthesis and FE mesh generation.

Constructing statistical atlas

We have a set of 29 femur proximals as shown in Figure 4.10. These femurs are represented by boundary triangulations and are scaled into the unite bounding box. The number of vertex of each femur varies from 2912 to 3567. We find the

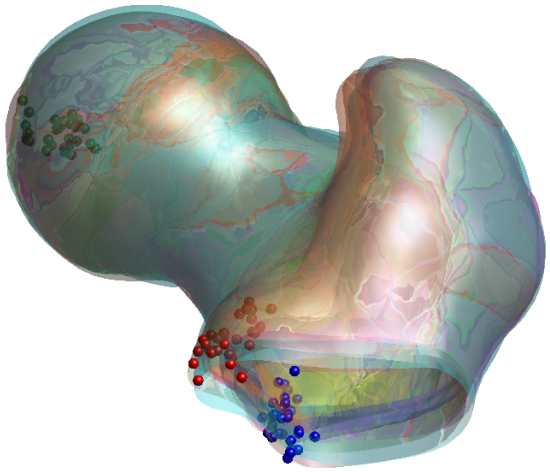

Figure 4.10: Overlay of 29 femur proximals plotted in different colors. The red, blue and green points are, respectively, landmarks on the protrude, lower laterals, and femur heads.

correspondences between those shapes by FFD with the chosen landmarks in Figure 4.10. Then we re-sample each shape based on the correspondences and conduct the statistical shape modeling.

Figure 4.11 shows the shapes before GPA, after GPA and the mean shape $\bar{\mathbf{S}}$ of the femurs. Figure 4.12 has shown the first three eigen-modes out of the 28 and Figure 4.13 shows the cumulative shape variances captured by the increasing number of shape modes from one mode to the whole 28 modes.

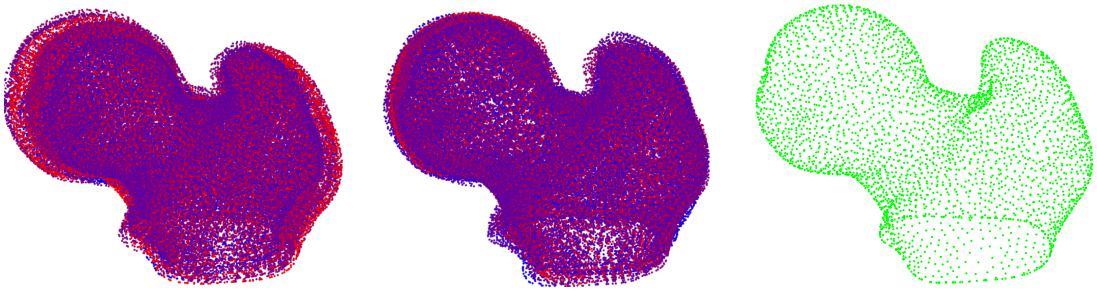

(a) (b) (c)

Figure 4.11: (a) 29 shapes before GPA; (b) 29 shapes after GPA; (c) mean shape $\bar{\mathbf{S}}$.

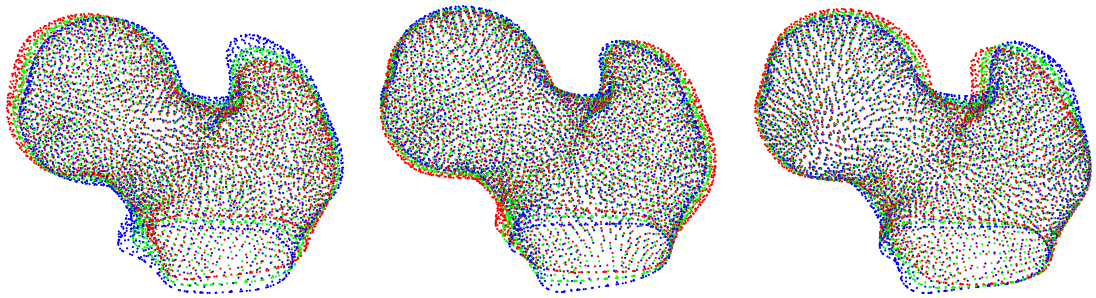

(a) $\bar{\mathbf{S}} \pm 2\sigma_1\Psi_1$ (b) $\bar{\mathbf{S}} \pm 2\sigma_2\Psi_2$ (c) $\bar{\mathbf{S}} \pm 2\sigma_3\Psi_3$

Figure 4.12: The first three eigen-modes of the fenurs: green one is the mean shape, red is the $+2\sigma$ deviation and blue is the -2σ deviation.

After we obtained the statistical shape model, we create finite element mesh for the mean shape as shown in Figure 4.14.

Shape instantiation and projection

With the obtained statistical shape model, we can conduct eigen-space search for a given subject-specific shape. Here we did the same leave-one-out experiment for the femur-proximal as in the 2D hand example. In the experiment we use 15 eigen-modes (captures more than 96% of the variation) to instantiate the new shape.

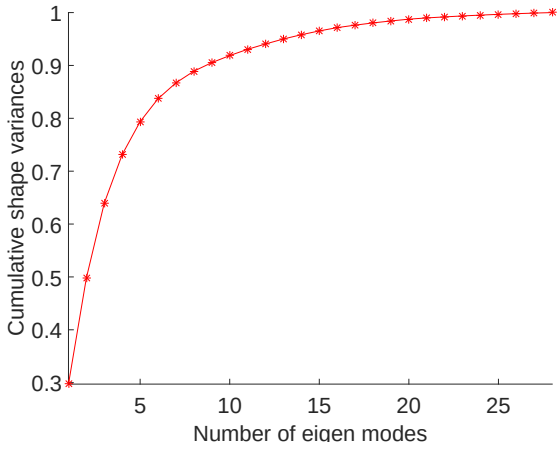

Figure 4.13: The cumulative shape variances captured by the increasing number of shape modes.

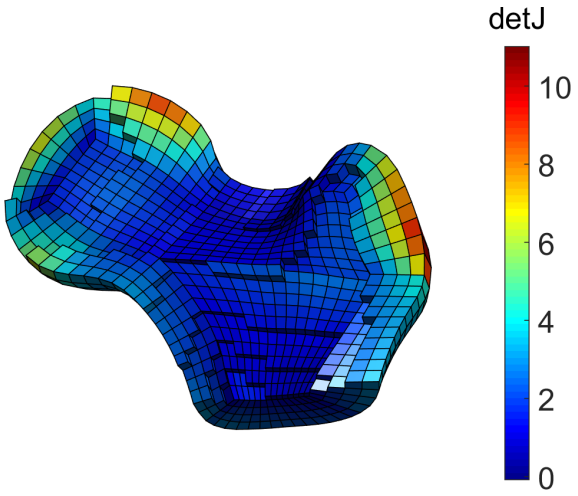

Figure 4.14: Hex-mesh of the mean shape and the Jacobians.

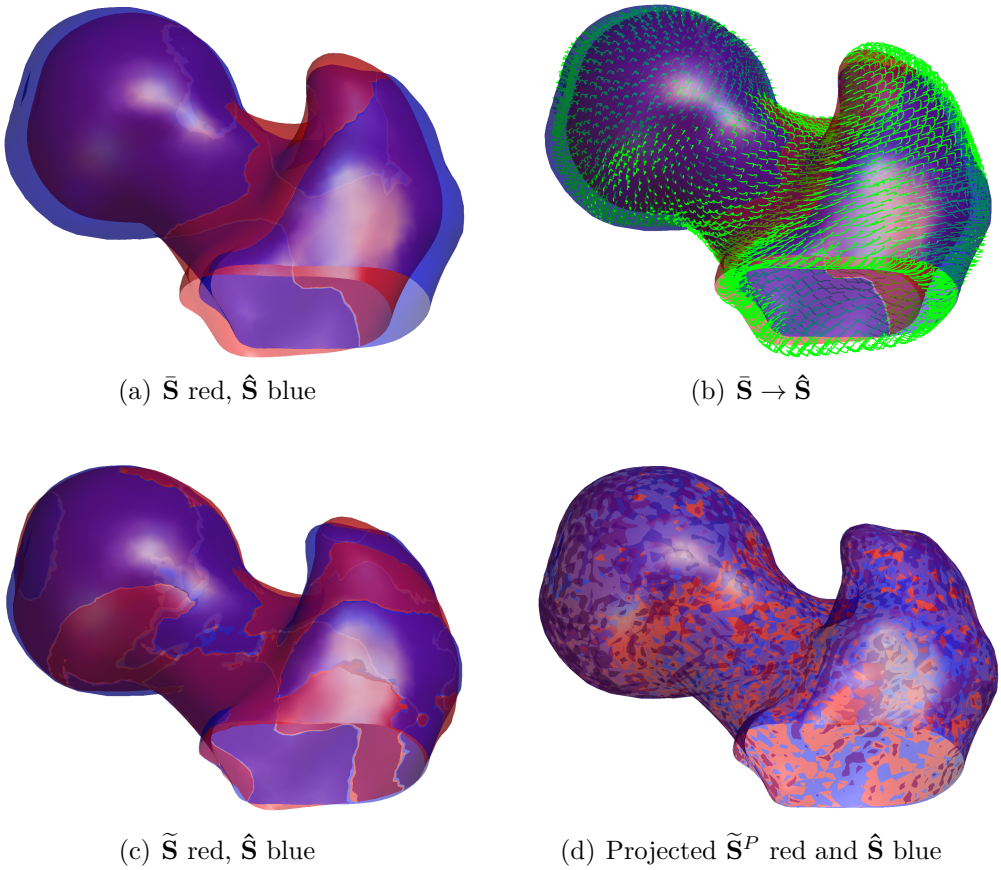

(a) $\bar{\mathbf{S}}$ red, $\hat{\mathbf{S}}$ blue

(b) $\bar{\mathbf{S}} \rightarrow \hat{\mathbf{S}}$

(c) $\widetilde{\mathbf{S}}$ red, $\hat{\mathbf{S}}$ blue

(d) Projected $\widetilde{\mathbf{S}}^P$ red and $\hat{\mathbf{S}}$ blue

Figure 4.15: (a) The mean shape $\bar{\mathbf{S}}$ (the inner red one) and the given shape $\hat{\mathbf{S}}$ (blue); (b) the locus of each vertex in the eigen-space search; (c) the result $\widetilde{\mathbf{S}}$ of eigen-space search; (d) normal projection.

Figure 4.15 shows one example of shape instantiation and projection. Figure 4.15(c) shows the instantiated shape $\widetilde{\mathbf{S}}$ and Figure 4.15(d) shows its projection $\widetilde{\mathbf{S}}^P$ onto the given shape $\hat{\mathbf{S}}$. It is clear that the deviation between the synthesized shape $\widetilde{\mathbf{S}}^P$ and the given shape$\hat{\mathbf{S}}$ is random, indicting a good accuracy of the synthesis process.

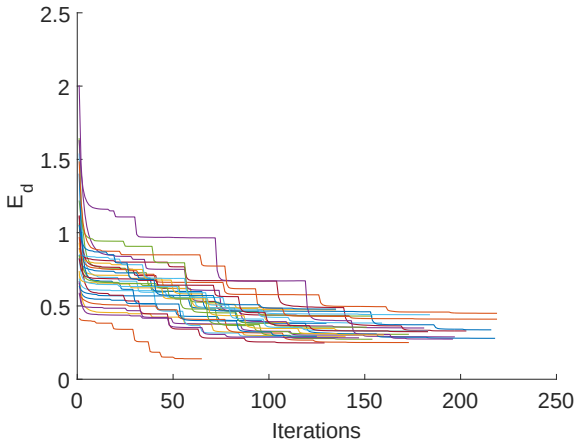

Figure 4.16: The value of E_d at each iteration.

Figure 4.16 shows the distance of the instantiated shape (E_d in section 4.3) to the given shape at each iterations. The average edge length of each triangle mesh is around 0.02, and all the instantiations have given an average surface deviation just about half of the average edge length, which shows the success of the instantiation. The average surface deviation is calculated by $\sqrt{E_d/n_v}$, where E_d is the square distance defined in (4.4) and n_v is the number of vertex. The running time is from 0.939999 seconds ($\mathbf{S}_2$, 65 iteration) to 3.337465 seconds ($\mathbf{S}_8$, 218 iterations) on Matlab with processor: Intel Core i7, 3.50GHz. Table 4.2 shows the detailed statistics.

In Figure 4.17 we compare the correlation coefficients of normals among the ICP,

Table 4.2: Performances (3D femurs): on Matlab with Intel Core i7, 3.50 GHz

	Running time	**Iterations**	**Num. of pts**
minimum	0.94 s	65	2912
maximum	3.34 s	218	3567

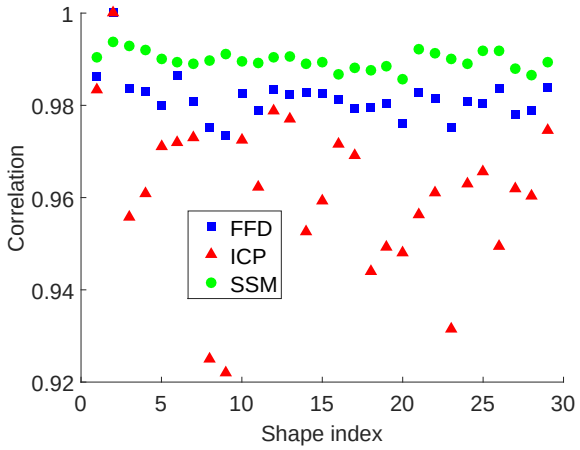

Figure 4.17: The correlation coefficient of normals.

FFD and SSM based methods. In ICP and FFD, shape 2 is chosen as the template, so the correlation with itself is 1. For SSM based shape synthesis, we conducted a leave-one-out test and thus obtained correlation for 29 shapes. The correlations obtained by SSM synthesized shapes (circle) is slightly better than the correlations obtained by FFD (square) and show obvious improvement than the correlations (triangles) obtained by ICP. This suggests that both FFD and SSM based approach leads to comparable shape correspondence. However, FFD requires 3 landmark points for guidance during the deformation process.

In Figure 4.18 we have removed the top of the given shapes $\hat{\mathbf{S}}_1, \hat{\mathbf{S}}_2, \hat{\mathbf{S}}_3$ and repeated the same process as we did in Figure 4.15. The results show that our method is

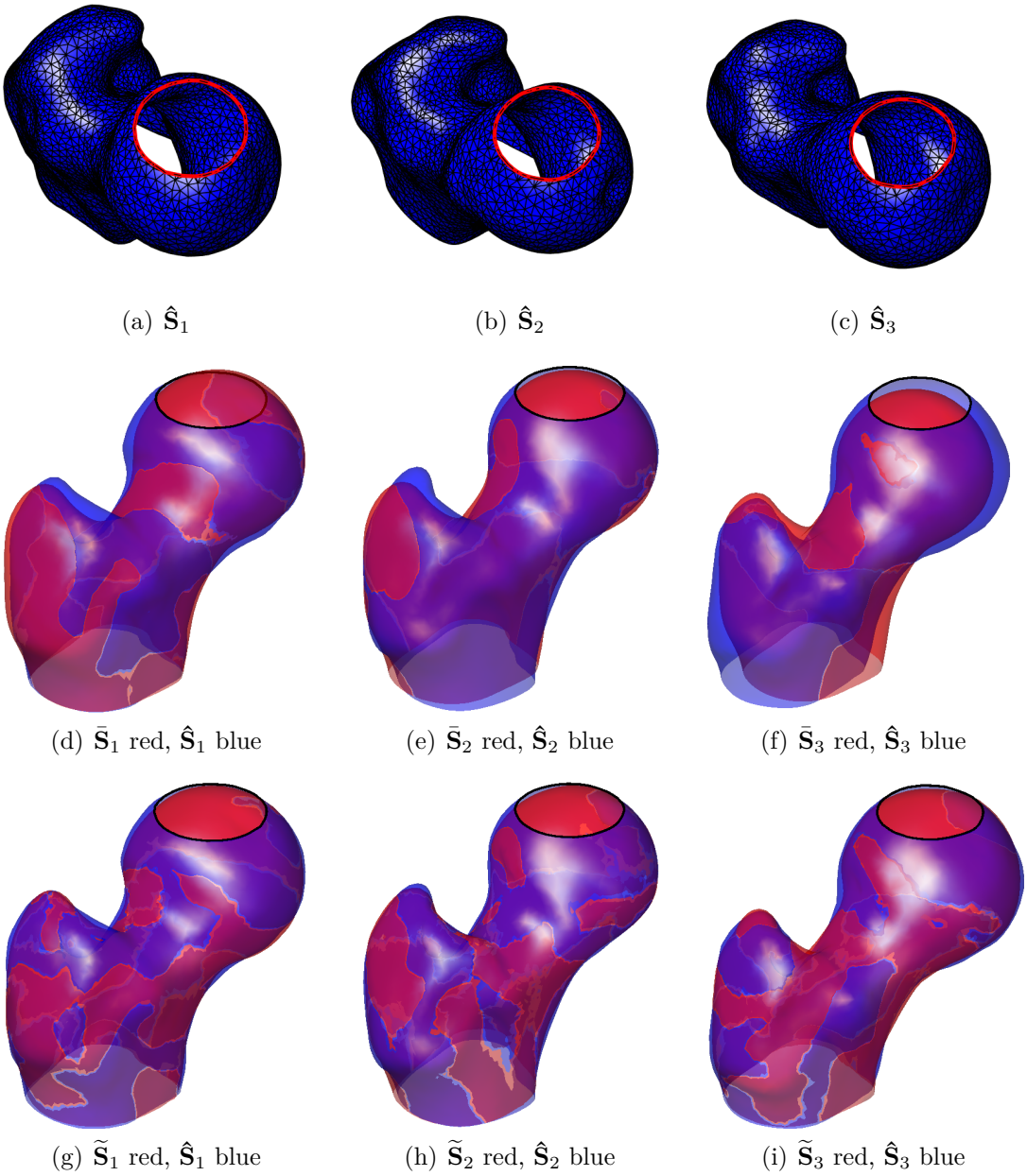

(a) $\hat{\mathbf{S}}_1$ (b) $\hat{\mathbf{S}}_2$ (c) $\hat{\mathbf{S}}_3$

(d) $\bar{\mathbf{S}}_1$ red, $\hat{\mathbf{S}}_1$ blue (e) $\bar{\mathbf{S}}_2$ red, $\hat{\mathbf{S}}_2$ blue (f) $\bar{\mathbf{S}}_3$ red, $\hat{\mathbf{S}}_3$ blue

(g) $\widetilde{\mathbf{S}}_1$ red, $\hat{\mathbf{S}}_1$ blue (h) $\widetilde{\mathbf{S}}_2$ red, $\hat{\mathbf{S}}_2$ blue (i) $\widetilde{\mathbf{S}}_3$ red, $\hat{\mathbf{S}}_3$ blue

Figure 4.18: (a), (b), and (c) are the shapes with missing top; (d), (e), and (f) are the overlappings of the mean shapes (red) and their respective target shapes (blue); (g), (h), and (i) shows the results $\widetilde{\mathbf{S}}_1, \widetilde{\mathbf{S}}_2, \widetilde{\mathbf{S}}_3$ of eigen-space search (synthesizing). Here we didn't do normal projection because the given shape is incomplete.

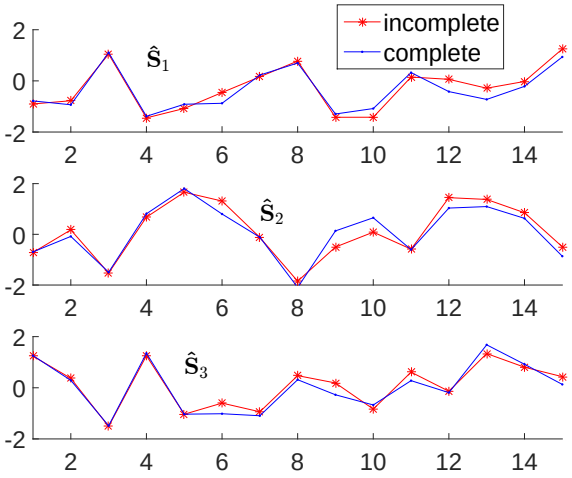

Figure 4.19: A comparison of the shape parameters $\frac{w_i}{\sigma_i}, i = 1, \cdots, 15$ found for the complete shapes in Figure 4.15 and the incomplete shapes in Figure 4.18. On the x-axis are the index of the eigen-modes, on the y-axis is the value of the shape parameter.

very robust even when the shapes are incomplete. In Figure 4.19 we have compared the shape parameters we obtained from the given complete shapes and the given incomplete shapes by the shape instantiation, the two sets of parameters only have minor differences and are in good accordance with each other. This suggests that the automatic shape instantiation is robust with incomplete data.

Automatic FE model generation

As shown in Figure 4.20, with the boundary correspondences obtained in the previous section, we morph the FE mesh of the mean shape in Figure 4.14 to the given shapes $\hat{\mathbf{S}}_1, \hat{\mathbf{S}}_2, \hat{\mathbf{S}}_3$ and obtain the subject-specific FE meshes, whose Jacobians are non-negative.

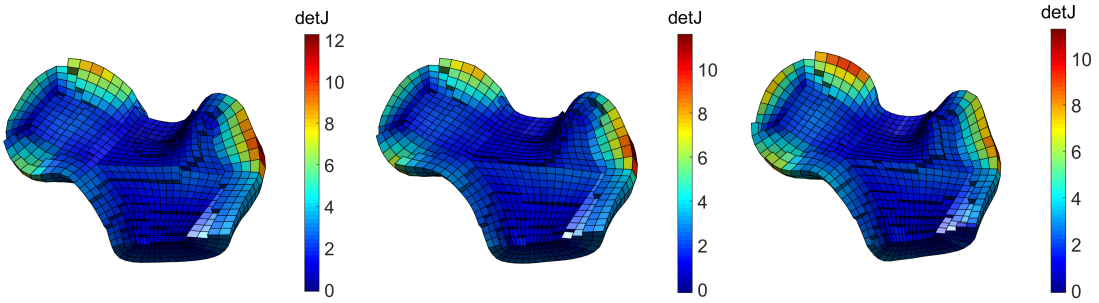

(a) FE mesh of $\hat{\mathbf{S}}_1$ (b) FE mesh of $\hat{\mathbf{S}}_2$ (c) FE mesh of $\hat{\mathbf{S}}_3$

Figure 4.20: The automatic generated FE mesh for the three given shapes in Figure 4.18.

4.6.3 Aorta

Due to the complex structures (two inlets on the main body and three leaflets inside), the mesh generation of aorta is very time consuming and the automatic FE mesh generation for aorta would be very appealing and have important potential practical applications.

Constructing statistical atlas

We have five aortic models, four of them were used for constructing statistical atlas and one was used as the given shape for synthesis.

As shown in Figure 4.21, we have four shapes in the training set. On each shape we have marked 13 landmarks, based on which we conducted the FFD based shape registration. Figure 4.22 shows the obtained mean shape model and eigen-modes of the statistical shape model.

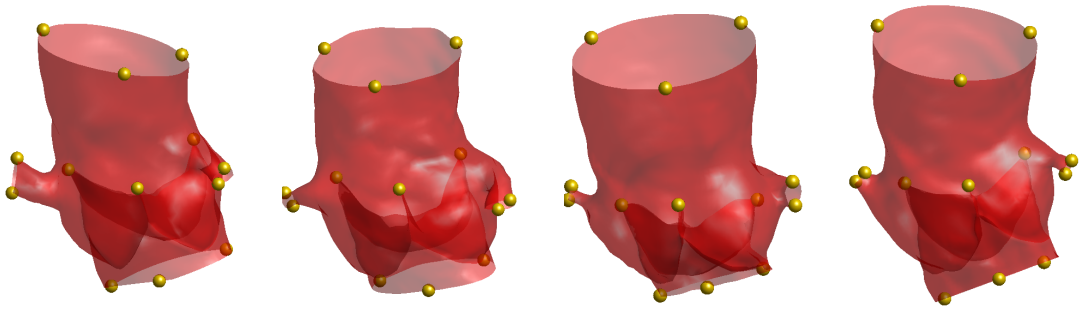

(a) $\mathbf{S}_1$ (b) $\mathbf{S}_2$ (c) $\mathbf{S}_3$ (d) $\mathbf{S}_5$

Figure 4.21: Four aortas in the training set to build the statistical atlas.

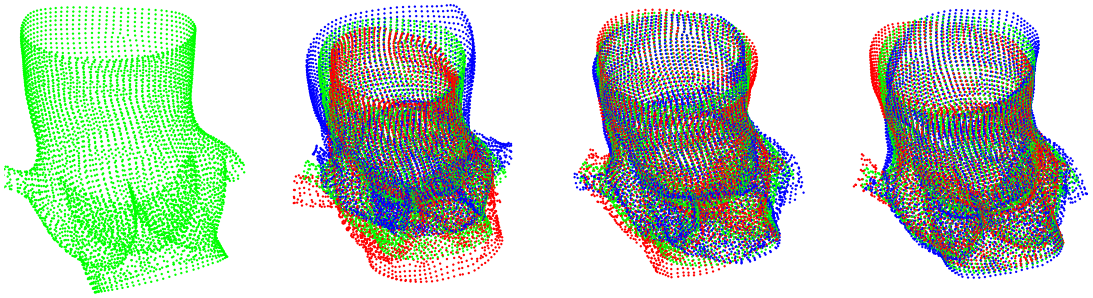

(a) $\bar{\mathbf{S}}$ (b) $\bar{\mathbf{S}} \pm 2\sigma_1\Psi_1$ (c) $\bar{\mathbf{S}} \pm 2\sigma_2\Psi_2$ (d) $\bar{\mathbf{S}} \pm 2\sigma_3 Psi_3$

Figure 4.22: Mean shape and the eigen-shapes.

Shape instantiation and projection

With the obtained mean shape $\bar{\mathbf{S}}$ and three eigen-modes Ψ_1, Ψ_2, Ψ_3, given a new shape $\hat{\mathbf{S}}$, we automatically instantiate it with the shape instances in the eigen-space and find the correspondences between the given shape $\hat{\mathbf{S}}$ and the mean shape $\bar{\mathbf{S}}$. In Figure 4.23 we show the process of shape instantiation and projection.

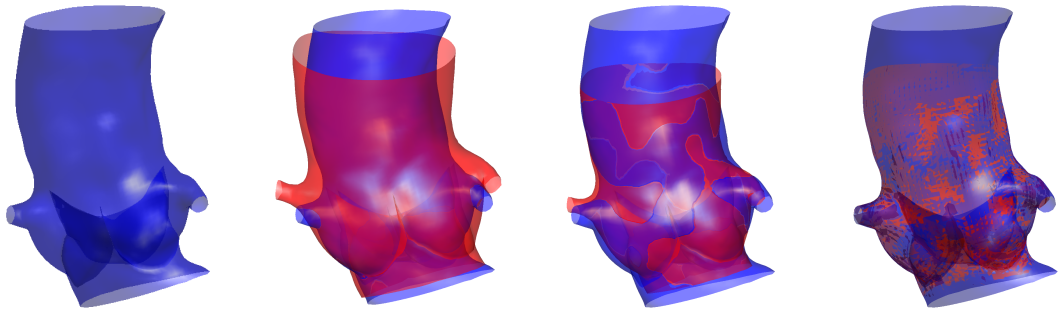

(a) $\hat{\mathbf{S}}$ (b) $\bar{\mathbf{S}} \rightarrow \hat{\mathbf{S}}$ (c) $\widetilde{\mathbf{S}}$ and $\hat{\mathbf{S}}$ (d) $\widetilde{\mathbf{S}}^P$

Figure 4.23: (a) The given shape $\hat{\mathbf{S}}$; (b) the overlay of the mean shape $\bar{\mathbf{S}}$ (red) and $\hat{\mathbf{S}}$ (blue); (c); shape instance $\widetilde{\mathbf{S}}$ optimized in the eigen-space; (d) projection to obtain the synthesized shape $\widetilde{\mathbf{S}}^P$.

Automatic FE mesh generation

With the correspondences obtained in the previous step, we automatically morph the hexahedral mesh of the mean shape to the given shape $\hat{\mathbf{S}}$ (Fig. 4.23(a)) by the free form-deformation in section 4.4. The resulting mesh was shown in Figure 4.24.

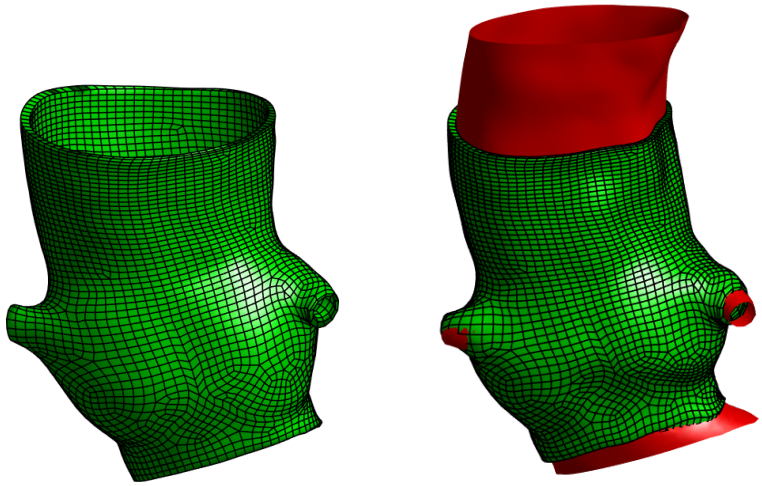

(a) $\overline{\mathbf{T}}$ (b) $\hat{\mathbf{T}}$

Figure 4.24: (a) Hexahedral mesh of the mean shape, (b) generated Hexahedral mesh (green) of the given shape $\hat{\mathbf{S}}$ (red).

5

A Taylor expansion approach for computing structural performance variation from population-based shape data

Rapid advancement of sensor technologies and computing power has led to wide availability of massive population-based shape data. This chapter[1] presents a Taylor expansion based method for computing structural performance variation over its shape population. The proposed method takes four steps: 1) learning the shape parameters and their probabilistic distributions through the statistical shape modeling; 2) deriving analytical sensitivity of structural performance over shape parameter; 3) approximating the explicit function relationship between the finite element (FE) solution and the shape parameters through Taylor expansion; 4) computing the performance variation by the explicit function relationship.

[1]This chapter is based on the following paper: Xilu Wang, Xiaoping Qian, "A Taylor expansion approach for computing structural performance variation from population-based shape data", Journal of Mechanical Design 139 (2017): 111411.

To overcome the potential inaccuracy of Taylor expansion for highly nonlinear problems, a multi-point Taylor expansion technique is proposed, where the parameter space is partitioned into different regions and multiple Taylor expansions are locally conducted. It works especially well when combined with the dimensional reduction of the principal component analysis in the statistical shape modeling.

Numerical studies illustrates the accuracy and efficiency of this method.

5.1 Background

Our approach builds on statistical analysis of shape variations, also known as statistical shape modeling (SSM). SSM has emerged as a powerful tool [34] for shape learning from a population where statistical analysis of shape variation is conducted, typically through principal component analysis. It has found its success in various fields including image segmentation [71], motion tracking [44], and parametric shape design [24; 13]. The use of statistical shape modeling techniques to understand shape variations and its effect on biomechanical performance has been recently attempted in [6; 28; 39; 35; 39; 36]. However, the computing of the structure performance variation over a population is usually through the Monte Carlo simulation, i.e. by randomly generating the shape parameters according to the learned probabilistic distributions, and obtaining a set of new shapes and new finite element meshes usually through mesh deformation. The finite element analysis is then performed on each of the generated finite element models and the results are collected from which the structural performance variation is obtained. For example, in [36], the performance of

the cementless osseointegrated tibial tray in a general population was studied using 1000 finite element analyses on different subjects. The drawback of such Monte Carlo simulation based approach lies in its inefficiency. In order to obtain a result with reasonable accuracy, a large number of experiments (usually > 500) are needed and each experiment, in this context, requires an expensive finite element analysis.

The advantage of our approach lies in the fact that only one time FE analysis of the mean shape is used to predict the subject-specific shape's structural performance and the performance variation over the population. Figure 5.1 shows the proposed approach as applied in a heat transfer problem: approximating temperature fields for a shape population with Taylor expansion of the FE solution for the mean shape. Given a population of shapes, the mean shape and the modes of variation are obtained by the statistical shape modeling. A shape instance is then represented as the linear combination of the mean shape and the modes of variation. The weights $\mathbf{w} = [w_1 \cdots w_m]^T$ is called the shape parameters. Based on the shape sensitivity analysis $\partial\mathbf{u}/\partial\mathbf{w}$, where $\mathbf{u}$ is the FE solution, the Taylor expansion is conducted to approximate the function $\mathbf{u}(\mathbf{w})$ and extrapolate the solution on the mean shape to other shapes.

The limitation of usual Taylor expansion lies in its potential inaccuracy for non-linear problems. In this work, to overcome potential inaccuracy of Taylor expansion, a multi-point based Taylor expansion technique is proposed. The parameter space of the shape population is partitioned into different regions and multiple Taylor expansions are conducted around the local bases within each region. This technique is extremely powerful when combined with the dimensional reduction of principal

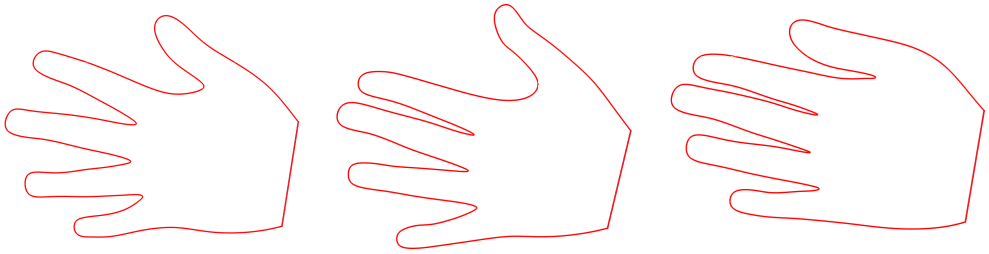

(a) A shape population

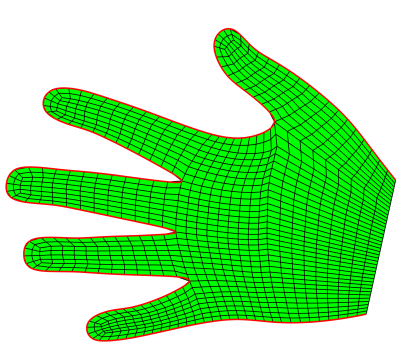

(b) FE mesh of the mean shape

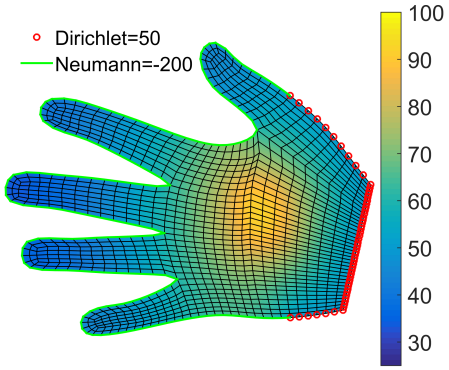

(c) FE result of (b)

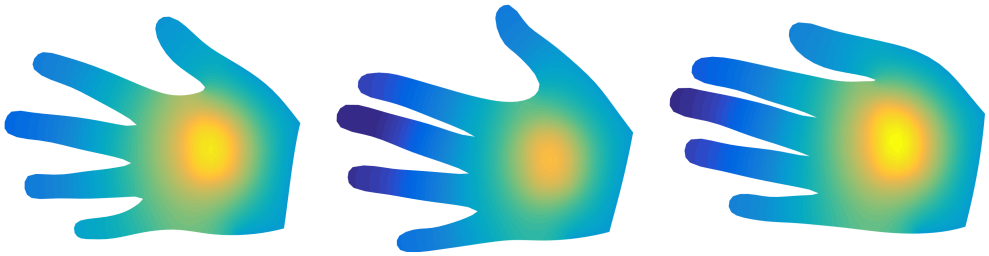

(d) Subject-specific temperature distributions from Taylor expansion

Figure 5.1: Proposed approach for predicting subject-specific structural performance: Taylor series expansion of the FE solution for the mean shape as applied in a heat transfer problem.

component analysis (PCA) in SSM. Since as a result of PCA, the first several shape parameters capture a majority of the shape variations. Thus the region partition is only carried with respect to the first few shape parameters and the dimension

of the problem has been significantly reduced. To determining the positions of the expansion bases, an optimization based approach is designed.

5.2 Method overview

The inputs for our method are the boundary shapes: $\left\{\mathbf{X}_\Gamma^{(k)}, k = 1, \cdots, n_s\right\}$, the loading conditions, and the structural performance c of interest (e.g. the structural compliance in linear elasticity and the thermal compliance in heat transfer). The outputs are: a statistical shape model that parameterizes the training shapes, the FE model and corresponding FE solution on the mean shape, the structural performance c as an explicit function of the shape parameters $\mathbf{w}$, and the probability distribution of the structural performance c within the population.

The proposed method involves four steps: 1) statistical shape modeling; 2) shape sensitivity analysis; 3) approximation by Taylor expansion; and 4) computing the performance variation.

Firstly, the shape parameters and their probabilistic distributions are learned from the statistical shape modeling. The shapes are parameterized by the eigen-shapes $\{\boldsymbol{\psi}_k\}$ and the shape parameters $\{w_k\}$

$$\mathbf{X}_\Gamma = \overline{\mathbf{X}}_\Gamma + \sum_{k=1}^{m} w_k \boldsymbol{\psi}_k, \;\; w_k \sim N(0, \lambda_k), \tag{5.1}$$

where $\mathbf{X}_\Gamma$ is the boundary shape, $\overline{\mathbf{X}}_\Gamma$ is mean shape of the population. $w_k \sim N(0, \lambda_k)$ means that the kth shape parameter is normally distribution with mean 0 and variance λ_k.

Secondly, the analytical sensitivities of the FE solution $\mathbf{u}$ and the structural performance c with respect to the shape parameters $\mathbf{w} = [w_1, \cdots, w_m]^T$ are calculated

$$\frac{\partial c}{\partial w_k} = \frac{\partial c}{\partial \mathbf{u}^t} \frac{\partial \mathbf{u}}{\partial w_k}, \ k = 1, \cdots, m. \tag{5.2}$$

Then, with the results of sensitivity analysis, the structural performance c is represented as an explicit function of the shape parameters $\mathbf{w}$ by Taylor expansion:

$$\tilde{c}(\mathbf{w}) = c(\mathbf{0}) + \sum_{k=1}^{m} \frac{\partial c}{\partial w_k} w_k, \tag{5.3}$$

where $c(\mathbf{0})$ is the structural performance of the mean shape. Note that Taylor expansion $\tilde{c}(\mathbf{w})$ is an approximation of the true function $c(\mathbf{w})$, in the later context, "tilde" will denote approximation by default.

Finally, the probability distribution $p(\tilde{c})$ of the structural performance is obtained by the explicit function relationship $\tilde{c}(\mathbf{w})$ and the learned probability distribution of the shape parameters $p(\mathbf{w})$.

The output is the cumulative distribution function (CDF) $F_{\tilde{c}}(c^*) = p(\tilde{c} \leq c^*)$ of the structural performance $\tilde{c}$, where $p(\tilde{c} \leq c^*)$ is the probability that $\tilde{c}$ is less than c^*.

In this study, we use $p(\cdot)$ to denote the probability of a specific event. The boundary shapes are represented by discrete sampling points: $\mathbf{X}_\Gamma = [\mathbf{x}_1, \cdots, \mathbf{x}_{n_b}]^t$, where $\mathbf{x}_i = [x_{i,1}, x_{i,2}]^t$ is vector of coordinates and n_b is the number of sampling points. We use $\mathbf{X}$ to denote the FE mesh in general. When $\mathbf{X}$ appears in the equations, it means the positions of the mesh nodes, for example, $\mathbf{X} = [\mathbf{p}_1, \cdots, \mathbf{p}_{n_p}]^t$, where $\mathbf{p}_i = [p_{i,1}, p_{i,2}]^t$ is vector of coordinates and n_p is the number of mesh nodes. We use

$\mathbf{u}$ to denote the FE solution in general. When $\mathbf{u}$ appears in the equations, it means the nodal values of the FE solution, for example, $\mathbf{u} = [u_1, \cdots, u_{n_p}]^t$. If $\mathbf{u}$ is an $n_p \times 1$ vector and $\mathbf{w}$ is an $m \times 1$ vector, $\frac{\partial \mathbf{u}}{\partial \mathbf{w}^t}$ would be an $n_p \times m$ matrix, its element in the ith row and jth column is $\frac{\partial u_i}{\partial w_j}$.

5.3 Statistical shape modeling

Statistical shape modeling plays important roles in computing the structural performance variation over a shape population. It computes the mean shape and the modes of variations in a population. It captures the variability of shapes in space through the probability distribution of the learned shape parameters. The mean shape of the population provides a statistical atlas, based on which we create the template FE mesh. For more details of statistical shape modeling please refer to chapter 2.

5.4 Shape sensitivity analysis

Through statistical shape modeling, a shape in the population is parameterized by the shape parameters $\mathbf{w}$. In this section we derive the analytical sensitivity of the FE solution $\mathbf{u}$ over the shape parameters $\mathbf{w}$. Assume we have the FE state equation

$$\mathbf{K}(\mathbf{w})\mathbf{u} = \mathbf{b}(\mathbf{w}), \tag{5.4}$$

the sensitivity of the FE solution over the shape parameters is calculated by [31]

$$\frac{\partial \mathbf{u}}{\partial w_k} = \mathbf{K}^{-1}\left(\frac{\partial \boldsymbol{b}}{\partial w_k} - \frac{\partial \mathbf{K}}{\partial w_k}\mathbf{u}\right), k = 1, \cdots, m. \tag{5.5}$$

For a specific element e in the stiffness matrix $\mathbf{K}$ or the loading vector $\mathbf{b}$, by the chain rule we have

$$\frac{\partial e}{\partial w_k} = \frac{\partial e}{\partial \mathbf{X}^t}\frac{\partial \mathbf{X}}{\partial \mathbf{X}_\Gamma^t}\frac{\partial \mathbf{X}_\Gamma}{\partial w_k}, \tag{5.6}$$

where $\frac{\partial e}{\partial \mathbf{X}^t}|_{1\times 2n_p}$ is the sensitivity of element e with respect to the mesh nodes, it is calculated according to the governing equations of the finite element method[50; 72; 31]; $\frac{\partial \mathbf{X}}{\partial \mathbf{X}_\Gamma^t}|_{2n_p\times 2n_b}$ is the sensitivity of the mesh nodes with respect to the boundary points; and $\frac{\partial \mathbf{X}_\Gamma}{\partial w_k}|_{2n_b\times 1}$ is the sensitivity of the boundary points with respect to the shape parameters and from equation (5.1) we have

$$\frac{\partial \mathbf{X}_\Gamma}{\partial w_k} = \boldsymbol{\psi}_k,\ k = 1, \cdots, m. \tag{5.7}$$

The only unknown in equation (5.6) is $\frac{\partial \mathbf{X}}{\partial \mathbf{X}_\Gamma^t}$, the sensitivity of the mesh nodes with respect to the boundary points. Here the thin-plate deformation (TPS) [73] is used to transfer the boundary perturbations to the interior nodes due to its simplicity, robustness.

Figure 5.2 shows an example of the thin-plate deformation, in which the boundary perturbation is transferred to the whole physical domain Ω. The FE mesh of the mean shape is embedded in the domain Ω and is deformed accordingly.

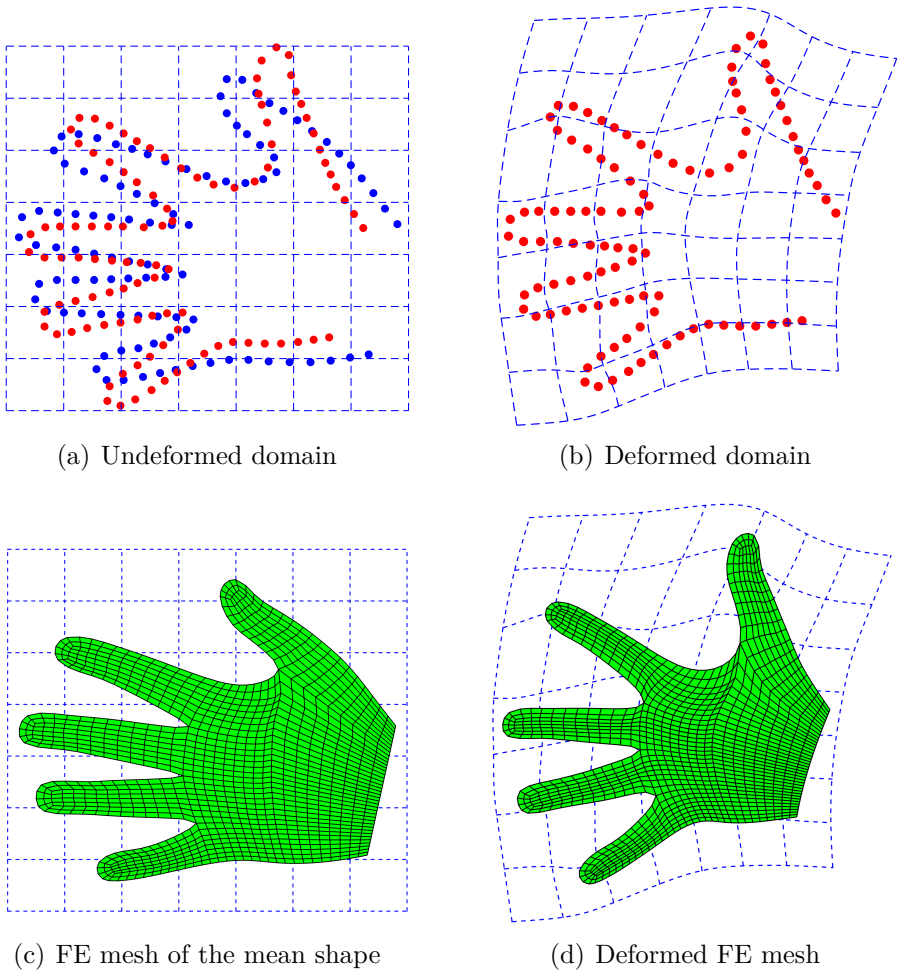

(a) Undeformed domain

(b) Deformed domain

(c) FE mesh of the mean shape

(d) Deformed FE mesh

Figure 5.2: The thin-plate deformation as a function of the boundary points $\mathbf{X}_\Gamma$: (a) the undeformed domain, the initial boundary points $\overline{\mathbf{X}}_\Gamma$ (blue), and the positions of the perturbed boundary points $\mathbf{X}_\Gamma$ (red); (b) the deformed domain based on the boundary perturbation $\overline{\mathbf{X}}_\Gamma \rightarrow \mathbf{X}_\Gamma$; (c) the FE mesh of the mean shape; (d) the deformed FE mesh.

The formulation of the thin-plate deformation is

$$\mathbf{\Phi}(\mathbf{x}) = \mathbf{c} + \mathbf{A}\mathbf{x} + \mathbf{V}^t\mathbf{U}(\mathbf{x}), \tag{5.8}$$

where $\mathbf{x} = [x_1, x_2]^t$ is the domain point and is deformed to $\mathbf{\Phi}(\mathbf{x})$; $\mathbf{c} = [c_1, c_2]^t$ is the translation vector; $\mathbf{A}$ is the 2×2 affine transformation matrix; $\mathbf{V}^t\mathbf{U}(\mathbf{x})$ is the deformation part, where $\mathbf{U}(\mathbf{x}) = [\rho(\mathbf{x} - \overline{\mathbf{x}}_1^\Gamma), \cdots, \rho(\mathbf{x} - \overline{\mathbf{x}}_{n_b}^\Gamma)]^t$ is the $n_b \times 1$ vector of kernel functions, $\overline{\mathbf{x}}_1^\Gamma, \cdots, \overline{\mathbf{x}}_{n_b}^\Gamma$ are the coordinates of boundary points with $\overline{\mathbf{x}}_i^\Gamma = [\overline{x}_{i,1}^\Gamma, \overline{x}_{i,2}^\Gamma]^t$, and $\mathbf{V} = [\mathbf{v}_1, \cdots, \mathbf{v}_{n_b}]^t$ is the $n_b \times 2$ matrix of TPS weights with $\mathbf{v}_i = [v_{i,1}, v_{i,2}]^t$. The kernel function ρ is defined as

$$\rho(h) = \begin{cases} \|h\|^2 \log(\|h\|), & \|h\| > 0; \\ 0, & \|h\| = 0. \end{cases} \tag{5.9}$$

It is worth mentioning that other deformation methods could also be applied, for example, the free-form deformation [59], the deformation by pseudo linear elasticity[69]. The reason we choose thin-plate deformation is that the bending energy of the underly domain is minimized by thin-plate deformation. It is proved in [74] that the deformation by equation (5.8) minimizes the bending energy [34; 74] of the underlying domain Ω with regards to all possible interpolating functions that map from $\overline{\mathbf{X}}_\Gamma$ to $\mathbf{X}_\Gamma$. Since distortion of the underlying domain may cause mesh tangling, the property of minimum bending energy is desirable.

Given the coordinates of the initial boundary points $\overline{\mathbf{x}}_1^\Gamma, \cdots, \overline{\mathbf{x}}_{n_b}^\Gamma$, and the coordinates of the perturbed boundary points $\mathbf{x}_1^\Gamma, \cdots, \mathbf{x}_{n_b}^\Gamma$, the translation vector $\mathbf{c}$, affine transformation matrix $\mathbf{A}$ and the deformation weights $\mathbf{V}$ can be solved as[73; 34]:

$$\mathbf{V} = \mathbf{B}^{11}\mathbf{X}_\Gamma, \quad \begin{bmatrix} \mathbf{c}^t \\ \mathbf{A}^t \end{bmatrix} = \mathbf{B}^{21}\mathbf{X}_\Gamma, \tag{5.10}$$

where $\overline{\mathbf{X}}_\Gamma = [\overline{\mathbf{x}}_1^\Gamma, \cdots, \overline{\mathbf{x}}_{n_b}^\Gamma]^t$ is the $n_b \times 2$ matrix of initial boundary points, $\mathbf{X}_\Gamma = [\mathbf{x}_1^\Gamma, \cdots, \mathbf{x}_{n_b}^\Gamma]^t$ is the $n_b \times 2$ matrix of perturbed boundary points. In this paper the mean shape $\overline{\mathbf{X}}_\Gamma$ is set as the initial boundary. $\mathbf{B}^{11}$ $(n_b \times n_b)$ and $\mathbf{B}^{21}$ $(3 \times n_b)$ are coefficient matrices decided by the positions of the initial boundary points $\overline{\mathbf{X}}_\Gamma$, whose closed form formulation is given in [34].

Substituting (5.10) into (5.8), we have

$$\mathbf{\Phi}(\mathbf{x}) = \mathbf{X}_\Gamma^t \mathbf{B}^{12} \begin{bmatrix} 1 \\ \\ \mathbf{x} \end{bmatrix} + \mathbf{X}_\Gamma^t \mathbf{B}^{11} \mathbf{U}(\mathbf{x}), \tag{5.11}$$

where $\mathbf{B}^{12}$ is the transpose of $\mathbf{B}^{21}$.

Assume $\overline{\mathbf{X}} = [\overline{\mathbf{p}}_1, \cdots, \overline{\mathbf{p}}_{n_p}]^t$ the nodes of the FE mesh of the mean shape $\overline{\mathbf{X}}_\Gamma$, and $\mathbf{X} = [\mathbf{p}_1, \cdots, \mathbf{p}_{n_p}]^t$ the nodes of the deformed FE mesh. We have $\mathbf{X}$ as a linear function of the boundary points $\mathbf{X}_\Gamma$

$$\mathbf{X} = \left([\mathbf{1}, \overline{\mathbf{X}}^t] \mathbf{B}^{21} + \mathbf{U}^t(\overline{\mathbf{X}}) \mathbf{B}^{11} \right) \mathbf{X}_\Gamma, \tag{5.12}$$

where $\mathbf{U}(\overline{\mathbf{X}}) = [\mathbf{U}(\overline{\mathbf{p}}_1), \cdots, \mathbf{U}(\overline{\mathbf{p}}_{n_p})]$. From equation (5.12) we have the sensitivity of the mesh nodes with respect to the boundary points

$$\frac{\partial \mathbf{X}}{\partial \mathbf{X}_\Gamma^t} = \begin{pmatrix} [\mathbf{1}, \overline{\mathbf{X}}^t] \mathbf{B}^{21} + \mathbf{U}^t(\overline{\mathbf{X}}) \mathbf{B}^{11} & \\ & [\mathbf{1}, \overline{\mathbf{X}}^t] \mathbf{B}^{21} + \mathbf{U}^t(\overline{\mathbf{X}}) \mathbf{B}^{11} \end{pmatrix}, \tag{5.13}$$

on the left side of the equation $\mathbf{X}$ and $\mathbf{X}_\Gamma$ are vectorized.

Now, we have the sensitivity of the FE nodal solutions $\frac{\partial \mathbf{u}}{\mathbf{w}^t}$ from equations (5.5) and (5.6). The sensitivity of the structural performance $\frac{\partial c}{\partial \mathbf{w}^t}$ can be easily obtained

by the chain rule:

$$\frac{\partial c}{\partial \mathbf{w}^t} = \frac{\partial c}{\partial \mathbf{u}^t}\frac{\partial \mathbf{u}}{\partial \mathbf{w}^t}. \tag{5.14}$$

5.5 Taylor approximation of structural performance

Taylor expansion is used to approximate the structural performance c by an explicit function $\tilde{c}(\mathbf{w})$ of the shape parameters $\mathbf{w}$.

5.5.1 Single point Taylor expansion

In the single point Taylor expansion, the performance function $c(\mathbf{w})$ is expanded around the mean shape, where the shape parameters are zeros.

$$\tilde{c}(\mathbf{w}) \;\; = \;\; c(\mathbf{0}) + \frac{\partial c}{\partial \mathbf{w}^t}\mathbf{w}, \tag{5.15}$$

where $c(\mathbf{0}) = c(\mathbf{u}(\mathbf{0}))$, and $\mathbf{u}(\mathbf{0})$ is the FE solution on the mean shape solved from the below equation:

$$\mathbf{K}(\mathbf{0})\mathbf{u} = \mathbf{b}(\mathbf{0}). \tag{5.16}$$

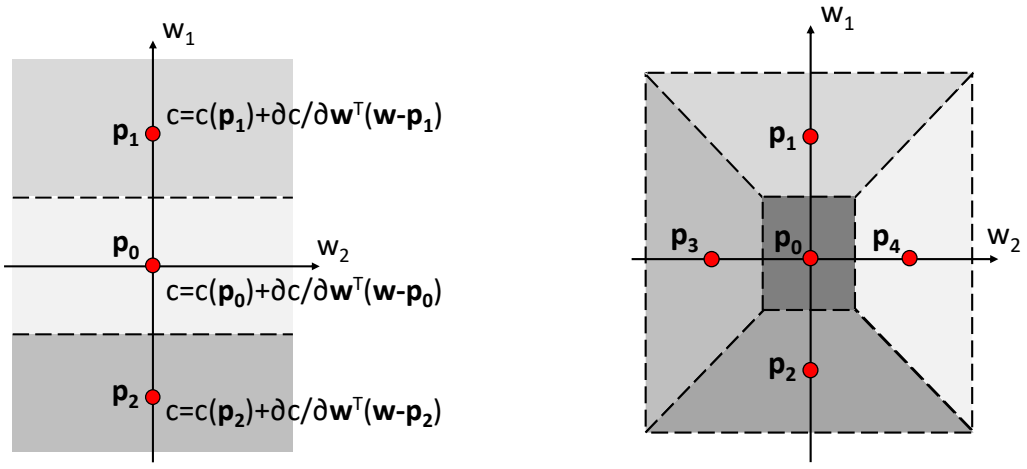

(a) Three regions (b) Five regions

Figure 5.3: Partition the domain into different regions and conduct Taylor expansion in each region separately.

5.5.2 Multi-point Taylor expansion

To overcome the potential inaccuracy of Taylor expansion at points far away from the mean shape, a multi-point Taylor expansion technique is proposed.

As shown in Figure 5.3 are two different examples of the multi-point Taylor expansion. In Figure 5.3(a) the domain has been partitioned into three regions by the two dashed horizontal lines. The Taylor expansions are conducted locally in each region around the bases $\mathbf{p}_i, i = 0, 1, 2$. In Figure 5.3(b) the domain has been partitioned into five regions. The procedure of the multi-region Taylor expansion is as follows:

1. Choosing n number of expansion bases $\{\mathbf{p}_0, \mathbf{p}_1, \cdots, \mathbf{p}_n\}$.

2. Partition the parametric domain into n regions $\Omega_0, \Omega_1, \cdots, \Omega_n$ according to the

closest distance to the base points:

$$\Omega_i = \left\{ \mathbf{w} \mid \|\mathbf{w} - \mathbf{p}_i\| = \min_{j=0,\cdots,n} \|\mathbf{w} - \mathbf{p}_j\| \right\}.$$

3. Approximate $c(\mathbf{w})$ piece-wisely by the Taylor expansions around the local bases:

$$\tilde{c}(\mathbf{w}) = \begin{cases} c(\mathbf{p}_0) + \frac{\partial c}{\partial \mathbf{w}^T}(\mathbf{w} - \mathbf{p}_0), \ \forall \mathbf{w} \in \Omega_0 \\ \vdots \\ c(\mathbf{p}_n) + \frac{\partial c}{\partial \mathbf{w}^T}(\mathbf{w} - \mathbf{p}_n), \ \forall \mathbf{w} \in \Omega_n \end{cases} \tag{5.17}$$

It should be noted that, though $\tilde{c}(\mathbf{w})$ may not be continuous, the obtained probability distribution $p(\tilde{c})$ will be close to that of the true performance $p(c)$ as long as $\tilde{c}(\mathbf{w})$ is close to $c(\mathbf{w})$.

Choosing appropriate expansion bases $\mathbf{p}_0 \cdots \mathbf{p}_n$ is critical in the multi-point Taylor expansion. For each point $\mathbf{w}$, it is expanded with respect to the closest base point. So the range of extrapolation at $\mathbf{w}$ is $l(\mathbf{w}) = \min_{j=0,\cdots,n} \|\mathbf{w} - \mathbf{p}_j\|$. Since the error of Taylor expansion is propositional to $l(\mathbf{w})^{r+1}$, where r is the degree of expansion and in this paper $r = 1$, it is desirable to minimize the overall squared range of extrapolation. However, each shape parameter $\mathbf{w}$ does not appear in the same frequency, the accuracy of approximation is more important at the regions of high probability. Based on that, an objective function is designed:

$$\min_{\{\mathbf{p}_j\}} \quad E = \int_{\Omega} l(\mathbf{w})^2 p(\mathbf{w}) d\mathbf{w}, \tag{5.18}$$

where the extrapolation range $l(\mathbf{w})^2$ is weighted by the probability density $p(\mathbf{w})$ and is integrated over the whole domain. Note that $l(\mathbf{w})$ in equation (5.18) is a minimum formula and will cause obstacles for the optimization. Since the p-norm is widely used in approximating the minimum and maximum formulas, $l^2(\mathbf{w}) = \min\limits_{j=0,\cdots,n} \|\mathbf{w} - \mathbf{p}_j\|^2$ is substituted by $(\sum_{i=0}^{n} l_j^{-2q})^{-\frac{1}{q}}$. Considering that the probability density $p(\mathbf{w})$ of the shape parameters is symmetric with respect to the origin as in equation (5.20), it is desirable to have the expansion bases also symmetric with respect to the origin. At last, we have the optimization formula:

$$\begin{aligned} \min_{\{\mathbf{p}_j\}} \quad & E = \int_{\Omega} (\sum_{i=0}^{n} l_j^{-2q})^{-\frac{1}{q}} p(\mathbf{w}) d\mathbf{w}, \\ \text{s.t.} \quad & \mathbf{p}_j = -\mathbf{p}_{n-j}, j = 0, \cdots, n. \end{aligned} \tag{5.19}$$

Locations of expansion bases are then obtained from (5.19) through a gradient decent approach.

5.6 Probabilistic distribution of the structural performance

Through the Taylor expansion, an explicit function relationship $\tilde{c}(\mathbf{w})$ between the shape parameters $\mathbf{w}$ and the structural performance c is obtained. By the statistical shape modeling, the probability density function of the shape parameters are learned:

$$p(\mathbf{w}) = \Pi_{k=1}^{m} (2\pi\lambda_k)^{-\frac{1}{2}} e^{-\frac{w_k^2}{2\lambda_k}}, \tag{5.20}$$

where w_k is the kth shape parameter and λ_k is the shape variance in the kth principal direction.

The cumulative distribution function of the approximated structural performance $\tilde{c}$ is given by:

$$F_{\tilde{c}}(c^*) = p(\tilde{c} \leq c^*) = \int\limits_{\tilde{c}(\mathbf{w}) \leq c^*} p(\mathbf{w}) d\mathbf{w}. \tag{5.21}$$

5.6.1 Closed form solution

If the obtained structural performance $\tilde{c}$ is linear and continuous as in equation (5.15), since it is assumed that the shape parameters are normally distributed, we have that $\tilde{c}$ is also normally distributed with mean $c(\mathbf{0})$ and variance:

$$\lambda_c = \frac{\partial c}{\partial \mathbf{w}^t} \Lambda \frac{\partial c}{\partial \mathbf{w}}, \tag{5.22}$$

where $\Lambda = \text{diag}(\lambda_1 \cdots \lambda_m)$ is the covariance matrix of $\mathbf{w}$. The closed form of equation (5.21) is then obtained accordingly.

5.6.2 Monte Carlo integration

If the obtained structural performance $\tilde{c}$ is discontinuous as in equation (5.17). A closed form of equation (5.21) is either non-existent or very hard to obtain. In such cases, the Monte Carlo integration is used to integrate (5.21) at various c^* values. The algorithm is as follows:

1. Randomly generate N (in this paper N=1000) sets of shape parameters $\{\mathbf{w}_i\}$

according to $p(\mathbf{w})$.

2. Calculate $c_i = \tilde{c}(\mathbf{w}_i)$ for each parameter $\mathbf{w}_i$ by equation (5.17).

3. Order the values of $\{c_i\}$ ascendantly and we have:

$$F_{\tilde{c}}(c_i) \approx \frac{i}{N}. \tag{5.23}$$

The 95% confidence interval of $p(\tilde{c} \leq c_i)$ is approximately $[\frac{i}{N} - \frac{1}{\sqrt{N}}, \frac{i}{N} + \frac{1}{\sqrt{N}}]$. Thus to achieve an accuracy of 5%, we need $N \geq 500$; to achieve an accuracy of 1%, we need $N \geq 10000$. In our examples we set $N = 1000$. The function evaluation of $\tilde{c}(\mathbf{w})$ in equation (5.17) is quite cheap, so the Monte Carlo integration is very efficient compared with the simulations by finite element analysis.

In order to obtain equation (5.17) the FEA problem need to be solved at every p_j. Here, as a result of dimensionality reduction of principal component analysis, most of the shape variances are concentrated along the first few shapes parameters, so the multi-point Taylor expansion only need to be done with respect to the first few shape parameters and is very efficient. In our later linear elasticity example, it is done with respect to the first shape parameter with three and five points respectively.

5.7 Numerical results

In this section, the influence of geometrical variation on the structural performances have been studied with a 2D heat transfer problem and a 2D elasticity problem. We examine the numerical accuracy of the Taylor expansion for various modes of shape

variations. We also compare the distributions of the structural performances obtained by Taylor expansion with those obtained by the Monte Carlo simulation.

The evaluation process of Monte Carlo simulation (MCS) is as follows:

1. Randomly generate $N \geq 500$ sets of shape parameters $\{\mathbf{w}_i\}$ according to $p(\mathbf{w})$.
2. For each shape parameter $\mathbf{w}_i$, generate the corresponding boundary shape $\mathbf{X}_\Gamma^{(i)}$ by the statistical shape model (5.1).
3. Generate the finite element mesh $\mathbf{X}^{(i)}$ for $\mathbf{X}_\Gamma^{(i)}$ by the thin-plate deformation of the FE mesh of the mean shape (5.12).
4. Conduct the FE analysis, record the results and repeat steps 2,3,4 until $i = N$.

In our numerical study, the 40 hand shapes in [40] are used as the training set as in Figure 2.1. Each shape is represented by $n_b = 2001$ number of discrete points. We model the shape variations among them through the statistical shape modeling method as detailed in [58]. The first 8 shape modes is used to compactly represent the overall shape variation, which captures more than 98% of the total shape variance. The template FE mesh is created on the mean shape and has $n_p = 1250$ number of nodes.

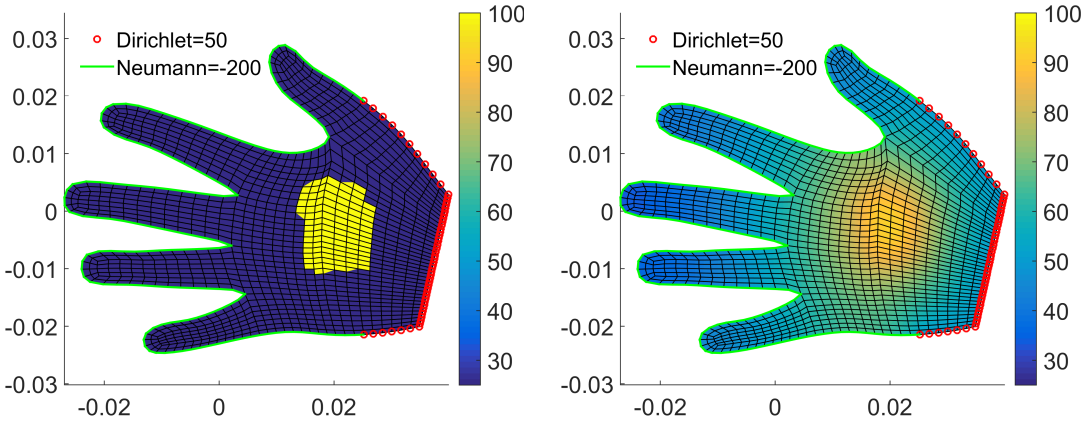

(a) Boundary conditions on the mean shape (b) FE solution

Figure 5.4: A 2D heat transfer problem: Dirichlet boundary condition $u = 50$ on Γ_1 (red circle), Neumann boundary condition $\frac{\partial u}{\partial \mathbf{n}} = -200$(green boundary), thermal load: $q = 1000000$ in the center of the hand (yellow area).

5.7.1 2D heat transfer problem

The 2D heat transfer is governed by the Poisson equation:

$$-\Delta u = q \quad \text{in} \quad \Omega \tag{5.24}$$

$$u = T_1 \quad \text{on} \quad \Gamma_1 \tag{5.25}$$

$$\frac{\partial u}{\partial \overrightarrow{n}} = g \quad \text{on} \quad \Gamma_2 \tag{5.26}$$

where u is the temperature, q is the thermal load, Ω is the domain of heat transfer, Γ_1 is the Dirichlet boundary, T_1 is the boundary temperature, Γ_2 is the Neumann boundary, and g is the Neumann boundary condition.

Figure 5.4 shows the 2D heat transfer on the hand shape. Figure 5.4(a) shows the FE mesh of the mean shape and the boundary conditions. Figure 5.4(b) shows the

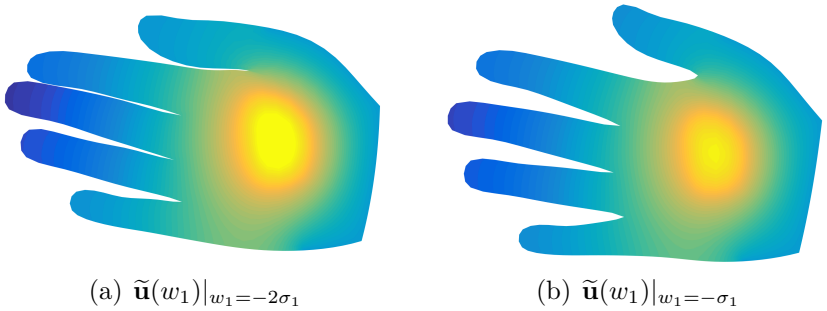

(a) $\widetilde{\mathbf{u}}(w_1)|_{w_1=-2\sigma_1}$ (b) $\widetilde{\mathbf{u}}(w_1)|_{w_1=-\sigma_1}$

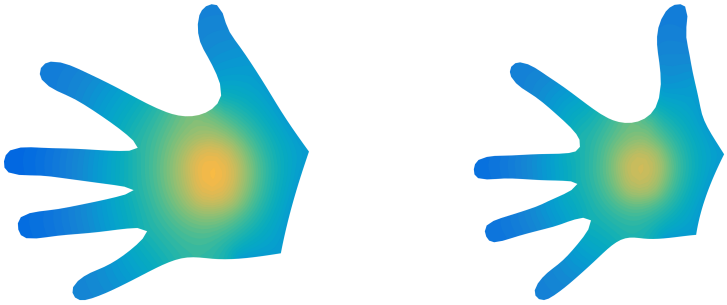

(c) $\widetilde{\mathbf{u}}(w_1)|_{w_1=\sigma_1}$ (d) $\widetilde{\mathbf{u}}(w_1)|_{w_1=2\sigma_1}$

Figure 5.5: Predicted temperature distribution due to shape variations in the first mode. The color means the temperature, and its range follows the same color bar as in Figure 5.4.

corresponding FE solution. In this example, the variability of the thermal compliance $c = \int_\Omega qud\Omega$ due to the shape variations is studied.

Temperature distribution by Taylor expansion

Figure 5.5 shows the predicted temperature distribution of shapes due to the change of the first shape parameter. We can see that as w_1 increases from $-2\sigma_1$ to $2\sigma_1$ in Figure 5.5(a), 5.5(b), 5.5(c), and 5.5(d), the hand becomes more expanded, and the temperature in the field decreases.

In order to examine the accuracy of Taylor expansion, here we compare the results predicted by the Taylor expansion with the ones obtained by the finite element analysis.

The Taylor expansion of the nodal temperatures $\mathbf{u}(\mathbf{w})$ and the thermal compliance $c(\mathbf{w})$ around the mean are done through equation (5.15). The finite element analysis are conducted at the designed points, as shown by the stars $*$ in Figure 5.7. At each point, a new shape is generated by the corresponding shape parameters, the FE mesh is obtained by the thin-plate deformation of the FE mesh of the mean shape and a new FE analysis is conducted.

Figure 5.6(a) and 5.6(b) show the errors between the temperatures predicted by Taylor expansion and from FE analysis with shape change in the first mode. The results are obtained by varying the first shape parameter from negative two standard deviations to positive two standard deviations, while keeping all the other shape parameters 0. The maximum errors in Figure 5.6(a) and 5.6(b) are 6.89 and 7.03, respectively, while the scale of temperature variation in our FE solution is about 80 as shown in Figure 5.4. We could see that the maximum error happens at the tip of the little finger, where the shape variation is large and is far from the Dirichlet boundary. The Taylor expansion extrapolates the FE solution of the mean shape to other shapes, so it is reasonable to expect that the maximum error happens at the farthest extrapolation point (large shape deviation). Since the temperature on the Dirichlet boundary is fixed, so there is no error on the Dirichlet boundary.

Figure 5.6(c) and 5.6(d) compare the Taylor expansion with the FE solutions for shape changes along the second mode. The maximum errors in Figure 5.6(c)

and 5.6(d) are 1.59 and 2.15, respectively. Figure 5.6(e) and 5.6(f) compares the Taylor expansion with the FE solutions for shape changes along the third mode. The maximum errors in Figure 5.6(e) and 5.6(f) are 0.80 and 0.81, respectively.

It could be seen that from the first mode to the third mode, the errors become smaller and smaller. That's because as a result of PCA, the first mode captures a majority of the total shape variances and the remaining modes captures fewer and fewer shape variances. So the deviation from the mean shape becomes smaller and smaller.

Thermal compliance by Taylor expansion

Figure 5.7(a) shows the relationship between the first shape parameter w_1 and the thermal compliance c by Taylor expansion and from the FE analysis. Since the thermal load q as in Figure 5.4(a) is added in the middle area, where has small extrapolation errors as in Figure 5.7(a), the results of Taylor expansion $\tilde{c}$ is close to the FE analysis c. The maximum relative error (max $|\tilde{c} - c|/c$) is 6.77%.

Figure 5.7(b) and 5.7(c) show the relationships between the second and third shape parameters with the thermal compliance. The results of Taylor expansion agree well with the finite element analysis, the maximum relative errors are 0.42% and 0.49% respectively.

Since the Taylor expansions in Figure 5.7(a), 5.7(b), and 5.7(c) gives relatively small extrapolation errors, the single-point Taylor expansion (5.15) around the mean shape is used to approximate $c(\mathbf{w})$ and calculate the cumulative probability function (CDF) of the thermal compliance. In this case we have the analytical solution (5.22).

The result is shown in Figure 5.7(d), it can be seen that the analytical CDF conforms well to that obtained by the Monte Carlo simulations. The three horizontal curves in Figure 5.7(d) partition the space into four intervals at the cumulative probabilities of 5%, 50%, and 95%. From the two inner intervals we could see that, for about 90% of the shapes in the population, the thermal compliance c should be within the range $[5.8 \times 10^9, 7.1 \times 10^9]$. The run time for the Taylor expansion based approach is 2.88s including the sensitivity calculation. The run time for the 500 Monte Carlo simulations is 106.54s. The computing is performed with MATLAB on the processor of "intel(R) Core(TM) i7-5500U".

5.7.2 2D elasticity problem

The governing PDEs of the linear elasticity problem are

$$-\boldsymbol{\nabla} \cdot \boldsymbol{\sigma} = \mathbf{f} \text{ in } \Omega, \tag{5.27}$$

$$\boldsymbol{\sigma} = 2\mu\boldsymbol{\varepsilon} + \lambda(\boldsymbol{\nabla} \cdot \mathbf{u})\mathbf{I} \text{ in } \Omega, \tag{5.28}$$

$$\boldsymbol{\varepsilon} = \frac{1}{2}(\boldsymbol{\nabla}\mathbf{u} + \boldsymbol{\nabla}\mathbf{u}^T) \text{ in } \Omega, \tag{5.29}$$

$$\mathbf{u} = \hat{\mathbf{u}} \text{ on } \Gamma_D, \tag{5.30}$$

$$\boldsymbol{\sigma}\mathbf{n} = \hat{\mathbf{t}} \text{ on } \Gamma_N, \tag{5.31}$$

where $\boldsymbol{\sigma}$ is the domain stress, $\mathbf{f}$ is the domain force, Ω is the domain, $\mathbf{u}$ is the displacement, $\mathbf{I}$ is the identity matrix, $\hat{\mathbf{u}}$ is the fixed displacement on the Dirichlet boundary Γ_D, and $\hat{\mathbf{t}}$ is the traction on the Neumann boundary Γ_N.

In this example, the variability of the structural compliance $c = \int_{\Gamma_N} \mathbf{u}^T \hat{\mathbf{t}} d\Gamma$ due to the shape variations is studied.

Figure 5.8(a) shows the FE model $\overline{\mathbf{X}}$ of the mean shape $\overline{\mathbf{X}}_\Gamma$ and the boundary conditions. Figure 5.8(b) shows the solved nodal displacements.

Nodal displacements by Taylor expansion

In this section we display the nodal displacements predicted from the Taylor expansion of equation (5.15) for shapes with varying shape parameters.

Figure 5.9 shows the predicted nodal displacements of shapes due to the change of the first shape parameter. As w_1 increases from $-2\sigma_1$ to 2σ in Figure 5.9(a), 5.9(b), 5.9(c), and 5.9(d), the hand becomes more expanded and smaller, and the displacements decreases.

Structural compliance by Taylor expansion

In this section the single-point Taylor expansion around the mean shape (5.15) is used to obtain the cumulative distribution function of the structural compliance.

Figure 5.10(a),5.10(b), and 5.10(c) plot the relationship between the first, second, and third shape parameters and the resulting structural compliance c by the Taylor expansions and from the FE analysis. It could be seen that the results of Taylor expansion deviates a lot from that of the FE analysis.

Figure 5.10(d) compares the cumulative distribution function of the structural compliance $\widetilde{c}$ obtained by the Taylor expansion with the one obtained by 500 Monte

Carlo simulations. We can see that the analytical CDF obtained by the Taylor expansion deviates a lot from the CDF obtained by the Monte Carlo simulations.

Multi-point Taylor expansion

The drawback of Taylor expansion lies in the fact that the approximation error becomes larger as the range of extrapolation increases. For certain problems, for example the 2D elasticity problem in this paper, it will cause large discrepancy between the approximated function $\tilde{c}(\mathbf{w})$ and the real one $c(\mathbf{w})$, and thus large discrepancy between the corresponding cumulative distribution functions. By observing Figure 5.10(a), 5.10(b) and 5.10(c), it can be seen that the response of the real FE analysis is quit curved and the Taylor expansion of the points far away from the mean shape deviates a lot from the real FE solution. To overcome this issue, the multi-point Taylor expansion technique, as discussed in section 5.2, is used.

Figure 5.11 shows the results obtained by the multi-point Taylor expansion. We can see that the cumulative distribution function obtained by the Multi-point Taylor expansion conform well with that of the Monte Carlo simulation. The expansion bases $\{\mathbf{P}_0 \cdots \mathbf{P}_n\}$ are obtained by the optimization formula (5.18). In this example, the multi-point Taylor expansion is only carried with respect to the first three shape parameters (w_1, w_2, w_3), which captures 91.0% of the total shape variances $\sum_{i=1}^{3} \sigma_i^2 / \sum_{i=1}^{40} \sigma_i^2 = 0.91$.

With $n = 2$, the obtained expansion bases are: $(1.107, 0, 0)$, $(0, 0, 0)$, $(-1.107, 0, 0)$, the result is shown in Figure 5.11(a). With $n = 4$, the obtained expansion bases are: $(1.764, 0, 0)$, $(-0.798, 0, 0)$, $(0, 0, 0)$, $(0.798, 0, 0)$, $(-1.764, 0, 0)$, the result is shown

in Figure 5.11(b). It is very interesting to notice that all the expansion bases are arranged along the first dimension. This perhaps can be ascribed to the fact that the 1st mode captures 66.7% of the total shape variances.

The run time for the multi-point Taylor expansion is 12.98s with $n = 2$ and 21.86s with $n = 4$ including the sensitivity calculation. The run time for the 500 Monte Carlo simulations is 133.86s. The computing is performed with MATLAB on the processor of "intel(R) Core(TM) i7-5500U".

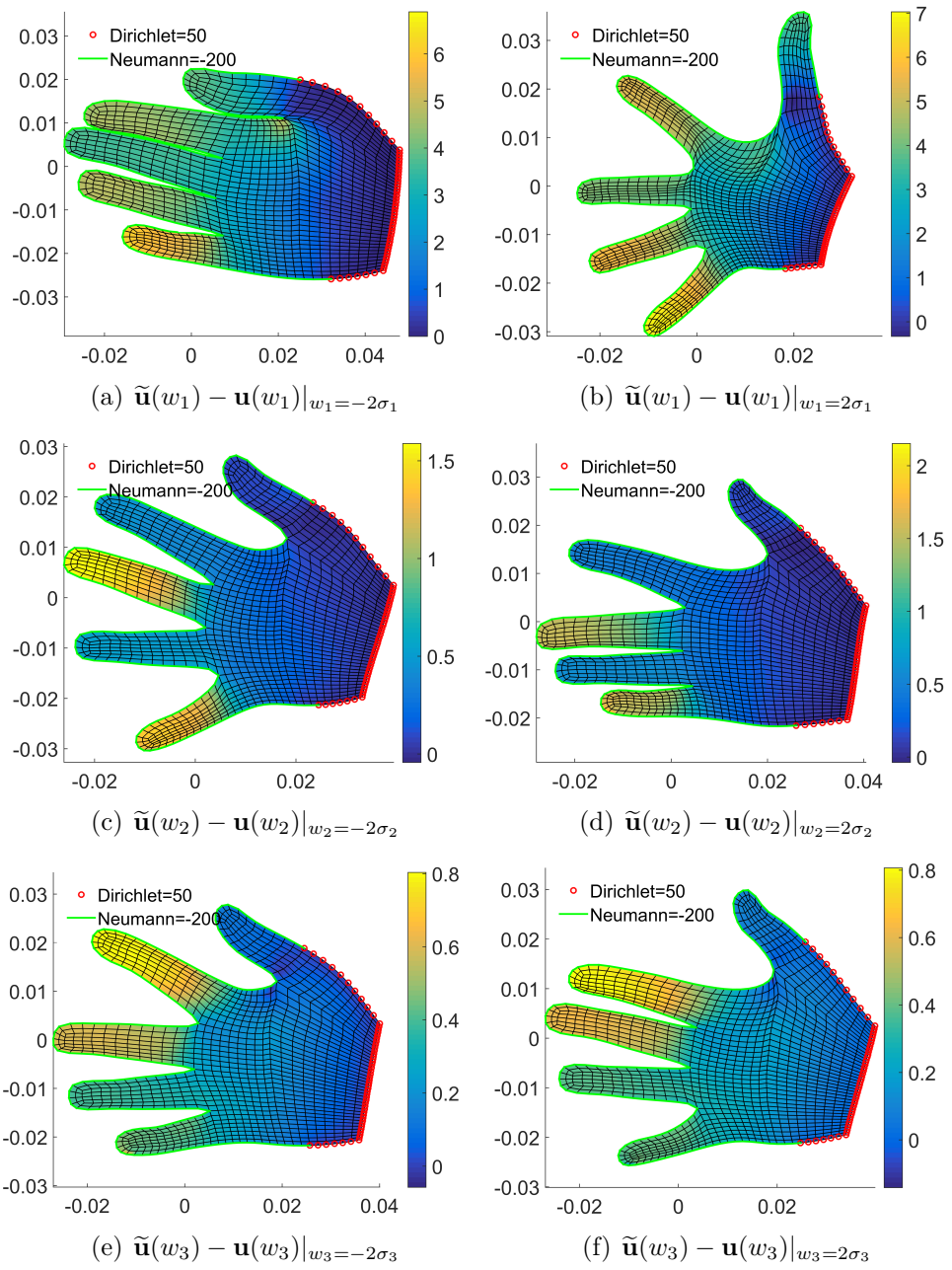

(a) $\widetilde{\mathbf{u}}(w_1) - \mathbf{u}(w_1)|_{w_1=-2\sigma_1}$ (b) $\widetilde{\mathbf{u}}(w_1) - \mathbf{u}(w_1)|_{w_1=2\sigma_1}$

(c) $\widetilde{\mathbf{u}}(w_2) - \mathbf{u}(w_2)|_{w_2=-2\sigma_2}$ (d) $\widetilde{\mathbf{u}}(w_2) - \mathbf{u}(w_2)|_{w_2=2\sigma_2}$

(e) $\widetilde{\mathbf{u}}(w_3) - \mathbf{u}(w_3)|_{w_3=-2\sigma_3}$ (f) $\widetilde{\mathbf{u}}(w_3) - \mathbf{u}(w_3)|_{w_3=2\sigma_3}$

Figure 5.6: The errors between the temperatures predicted by Taylor expansion and from FE analysis.

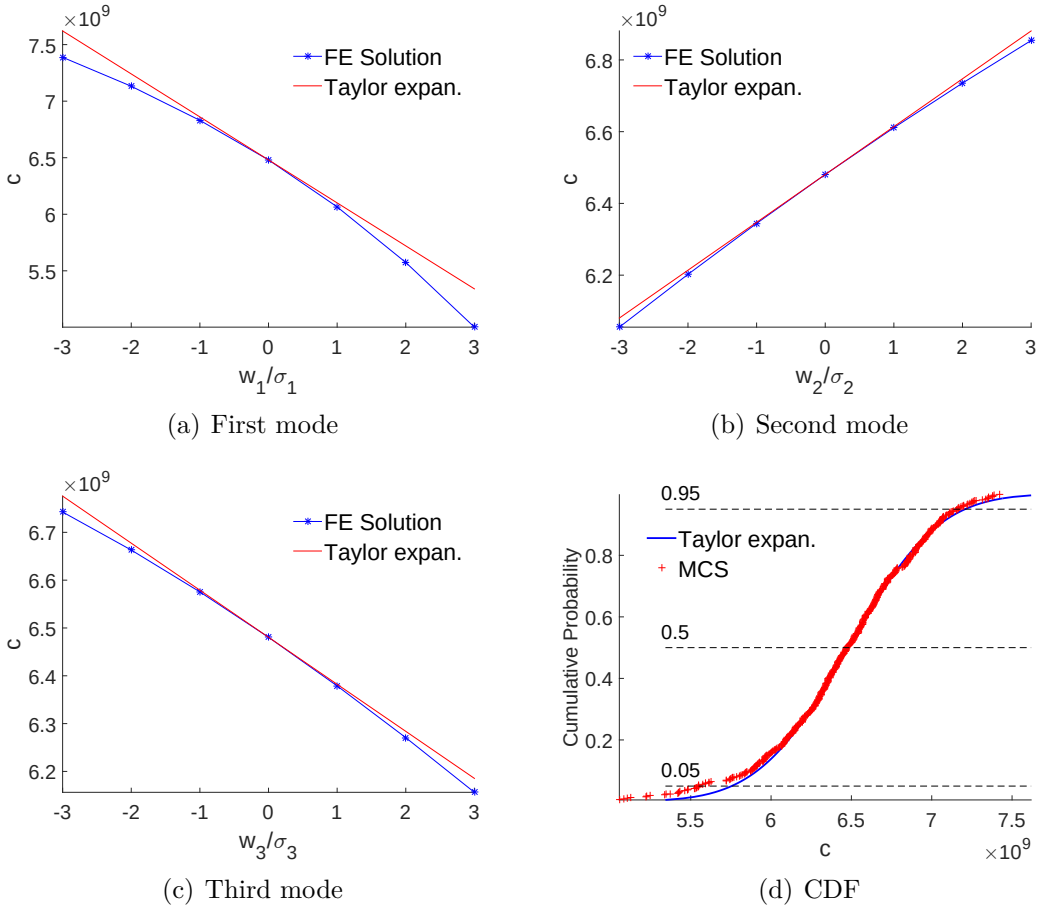

(a) First mode (b) Second mode

(c) Third mode (d) CDF

Figure 5.7: Comparing Taylor expansion with FE analysis of thermal compliance: (a) $\widetilde{c} = c(0) + w_1 \partial c/\partial w_1$; (b) $\widetilde{c} = c(0) + w_2 \partial c/\partial w_2$; (c) $\widetilde{c} = c(0) + w_3 \partial c/\partial w_3$; (d) cumulative distribution functions from Taylor expansions and from 500 Monte Carlo simulations.

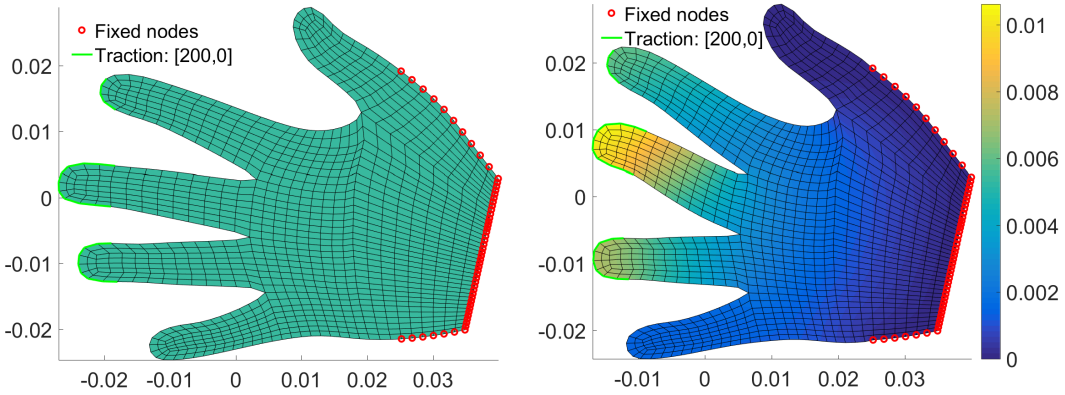

(a) Boundary conditions on the mean shape (b) Nodal displacements

Figure 5.8: A 2D linear elasticity problem: (a) FE model of the mean shape: Dirichlet boundary condition $\hat{\mathbf{u}} = [0, 0]^T$ on Γ_D (red circle), Neumann boundary condition $\hat{\mathbf{t}} = [200, 0]^T$ (green boundary); (b) the resulting nodal displacements, the color shows the values of horizontal displacements.

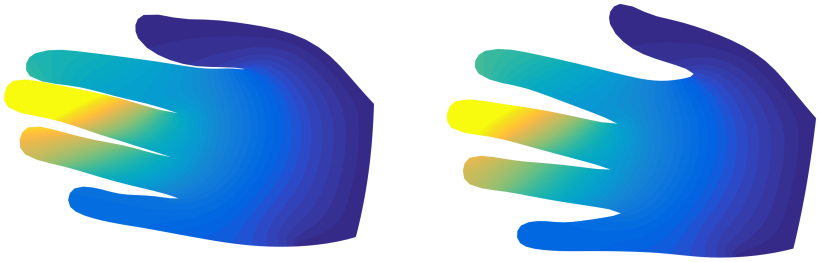

(a) $\widetilde{\mathbf{u}}(w_1)|_{w_1=-2\sigma_1}$ (b) $\widetilde{\mathbf{u}}(w_1)|_{w_1=-\sigma_1}$

(c) $\widetilde{\mathbf{u}}(w_1)|_{w_1=\sigma_1}$ (d) $\widetilde{\mathbf{u}}(w_1)|_{w_1=2\sigma_1}$

Figure 5.9: Taylor expansion predicted nodal displacements due to shape variations in the first mode. The color shows the values of horizontal displacements and its range follows the same color bar as in Figure 11.

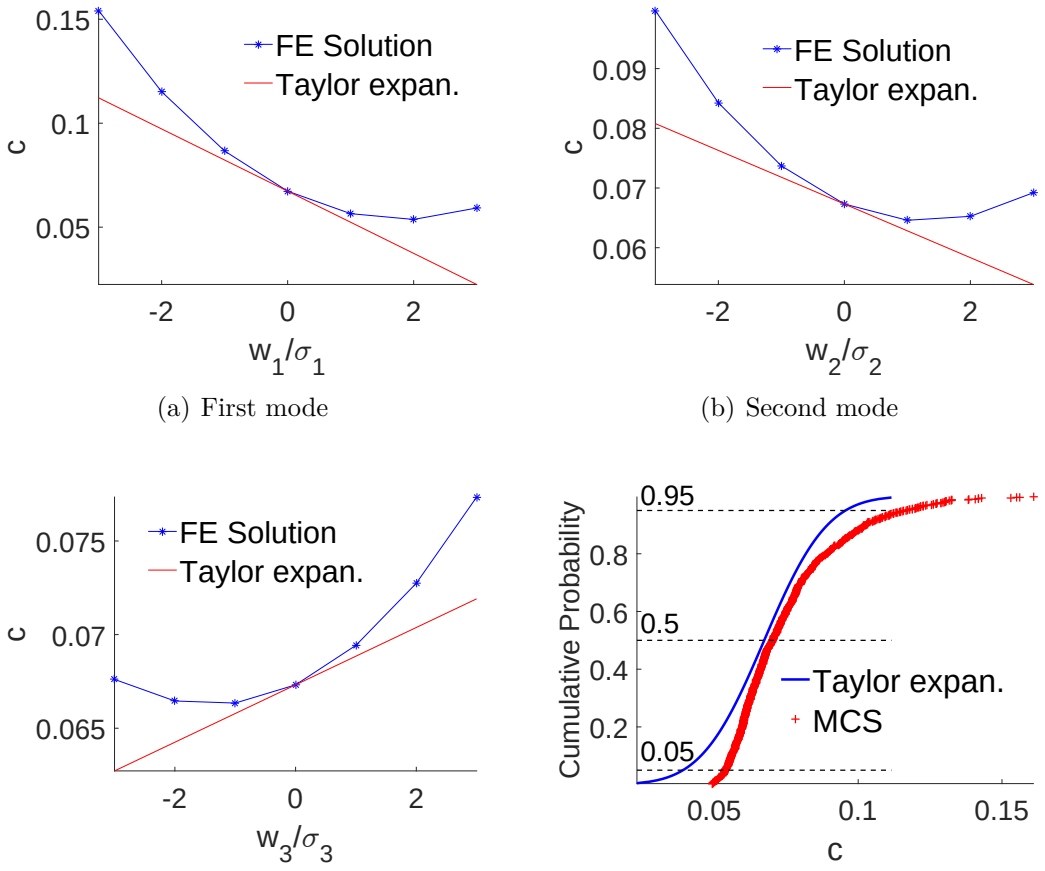

(a) First mode

(b) Second mode

(c) Third mode

(d) CDF

Figure 5.10: Comparing Taylor approximation with FE solutions of structural compliance.

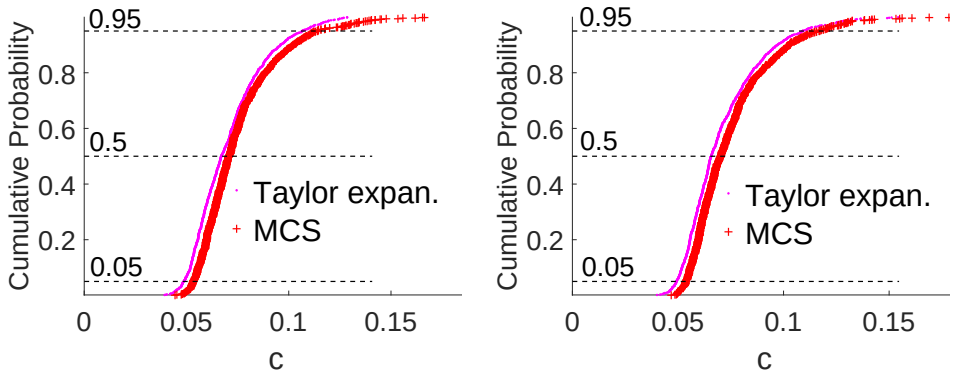

(a) Three bases (b) Five bases

Figure 5.11: Cumulative distribution function by multi-point Taylor expansion: (a) result with three expansion bases; (b) result with five expansion bases.

6

Conclusions and future work

6.1 Conclusions

In this dissertation research, a statistical atlas based approach that incorporates statistical shape modeling in finite element analysis and parametric shape design is developed for custom design and analysis. Given the measurements of a physical subject, its corresponding shape parameters in the linear shape space are obtained. With the obtained shape parameters, a complete shape model can be synthesized and used in virtual reality for custom fitting and interaction design. The subject-specific structural performance is obtained by extrapolating the FE solution of the mean shape to the obtained shape parameters through Taylor expansion. When necessary, subject-specific finite element analysis is performed by morphing the FE mesh of the mean shape to the obtained shape parameters. The structural performance variation over the shape population is computed from the explicit function obtained by Taylor expansion and the variances of the shape parameters.

The advantages of the developed approach include:

1) Construct faithful subject-specific shape models from very few measurements. Under the assumptions that the shape population follows normal distribution and that

the training shapes well represent the underlying shape population, the expectation of the squared error of shape reconstructions (3.14) is minimized by the selected feature points (or sizing dimensions). In our human body example, with the 15 selected feature points, the mean surface deviation of the reconstructions is 4.26 millimeter, while the mean surface deviation of the reconstructions by the selected anatomical landmarks is 4.50 millimeter and by the randomly generated points is 6.1 millimeter (Table 3.1 and Figure 3.13).

2) Automatically and efficiently create subject-specific FE model from the given shape model. The subject-specific FE mesh is obtained by morphing the FE mesh of the mean shape. The mesh morphing is guided by the boundary correspondence between the mean shape and the given shape, which is automatically sought in the shape space. Compared with the free-form deformation approach which has hundreds or even thousands of parameters (e.g. A $20 \times 20 \times 20$ Bspline grids have 8000 control points), the shape space is spanned by the first few eigenvectors of shape covariance matrix, thus (11 eigenvectors for 2D hands, 15 eigenvectors for human femurs, and 39 eigenvectors for human bodies). Thus deforming in the shape space is much more robust and efficient than by the free-form deformation. In our 2D and 3D examples, the shape space search only takes a few seconds and convergences within hundreds of iterations (Table 4.1 and 4.2), while the shape registration by free-form deformation takes several minutes to find the correspondences, not to mention the time needed for manually picking landmarks.

3) Efficiently predict subject-specific structural performance from given shape models. Subject-specific FE analysis is avoided by the Taylor expansion of the FE

solution on the mean shape to the subject-specific shapes. The single-point Taylor expansion approach is 50 times faster than the Monte Carlo simulations (2.88s vs 106.54s) in computing the structural performance variation over the population. The multi-point Taylor expansion approach is 10 times faster than the Monte Carlo simulations (12.98s vs 133.86s).

The main contributions of this dissertation research include:

- A statistical atlas based approach for custom design and analysis.

  The developed approach sits on the existing techniques of statistical shape modeling [34], builds on our own perspectives of shape space and shape distribution, and finds its success in subject-specific shape reconstruction, subject-specific FE modeling, and structural performance prediction. It allows efficient and faithful shape reconstruction from sparse measurements. It can bypass the laborious and manual process of subject-specific FE modeling and analysis. Such an ability brings about unprecedented capabilities and tantalizing opportunities for mass customization, part-specific failure prediction and just-in-time part maintenance, and patient-specific biomedical intervention and treatment.

- An approach that selects feature points and sizing dimensions based on the total variance they capture of the shape population.

  In the literature, feature point is selected on a single shape by its differential property or saliency. Here, statistical shape modeling is used to learn the population information and to formulate a quantitative metric that evaluates the percentage variance of the shape population captured by the feature points

and sizing dimensions. A forward selection algorithm is developed to select the feature points and sizing dimensions based on the metric. In the human body example, the selected feature points and sizing dimensions are capable of capturing the shape variations that are not captured by the 67 anatomical landmarks in [1] and the 25 sizing dimensions from the traditional measurement list [1]. The ability of capturing population information makes the selected feature points and dimensions powerful in sparse shape reconstruction and parametric shape design. In the shape classification example (rabbit tibia), the additional dimension that captures the bending mode of the tibia head is selected which nicely distinguishes the two groups of shapes, while in [64] only longitudinal information (tibia length and the change of tibia length) is used.

- A statistical atlas based approach for automated shape registration and finite element modeling.

  The developed approach allows automatic FE modeling of subject-specific shapes, even when a given subject-specific shape deviates significantly from the mean shape. The correspondence between a given subject-specific shape and the statistical atlas is sought by deforming the mean shape to the subject shape in the shape space. This is advantageous over the template deformation based approach in that large deviations between the template and the given shape usually require manual specification of shape correspondence for it to work. Searching shape correspondence by deforming in the shape space is inspired by the Active Shape Model in image segmentation [49]. The difference is that in image segmentation, the instantiated shape $\widetilde{\mathbf{S}}$ evolves in the image domain

and the domain information (e.g. nearby pixel values, gradient information) is utilized to guide the deformation. In [49] the values of nearby pixels along the gradient is utilized to match the instantiated shape $\widetilde{\mathbf{S}}$ to the unknown shape $\hat{\mathbf{S}}$ in image domain. However, our goal is to find the point correspondences between two discrete shapes represented by point sets, there's no domain information, the best match of $\widetilde{\mathbf{S}}$ on $\hat{\mathbf{S}}$ is updated by the closest points. In order to stabilize the matching process, a regularization term that reflects our prior belief of the likelihood of the shape parameters is added to the object function and the corresponding optimization strategy is developed (Algorithm 1 in Chapter 4).

- A multi-correlation based metric to evaluate the quality of the obtained shape correspondences.

  The multi-correlation of the normal vectors of two shapes is used to evaluate the obtained shape correspondences. The proposed metric nicely distinguishes the correspondences obtained by non-rigid registration (guided by landmarks) from the correspondences obtained by rigid shape registration. Since the former approach is much more flexible than the latter approach, it proves the effectiveness of the proposed metric.

- A Taylor expansion approach for predicting subject specific structural performance and computing structural performance variation over a shape population.

  Taylor expansion is used in structural reliability analysis [31; 32; 50] to extrapolate the FE solution of the template structure to the structures with different design parameters. However, for the structures that are not readily parame-

terized (e.g. bio-structures with freestyle shape variations), direct application of this approach remains challenging. In this research, the design parameters (shape parameters) are learned by the statistical analysis of training shapes. Our Taylor expansion approach allows computing of structural performance variations over a shape population without conducting a large number of FE analysis. The technical contributions of this work include: 1) We have derived the analytical sensitivity of the FE solution with respect to the shape parameters and applied it in the Taylor series approximation of the FE solutions. Numerical results confirms its accuracy with respect to FE solutions. 2) We have demonstrated that the multi-point Taylor expansion technique can effectively overcome the potential inaccuracy of Taylor expansion when combined with the dimensionality reduction of principal component analysis.

6.2 Limitations and future work

This section discusses the limitations of this work and the potential extensions to address these limitations in the future work:

- An important assumption in this work is that the shape parameters are normally distributed, which is in accordance with the observations of our training shapes (human body shapes, femur shapes, hands shapes and rabbit tibia shapes). The normal distribution assumption plays important role in computing structural performance variation from population based shape data, in feature point identification and dimension selection. However, there are shape populations

that are essentially not normally distributed, especially when obvious pose changes are involved [75; 76]. An enhanced edition of the foregoing assumption in dimension selection is that the joint distribution of the shape parameters and the sizing dimensions are normally distributed. This is in accordance with most of our observations, for example the joint distribution of the head breadths and the first shape parameter of the human body models as in Figure 6.1(a). However, we do observed one case that the joint distribution is not even close to normal distribution. Figure 6.1(b) shows the joint distribution of the chest circumferences and the first shape parameter of the human body models, which is bimodal due to the anatomical differences between male and female (normal distribution is single modal). This also explains that why the chest circumference, as a very important measure in anthropometry, is not selected by Algorithm 1 in Chapter 3.

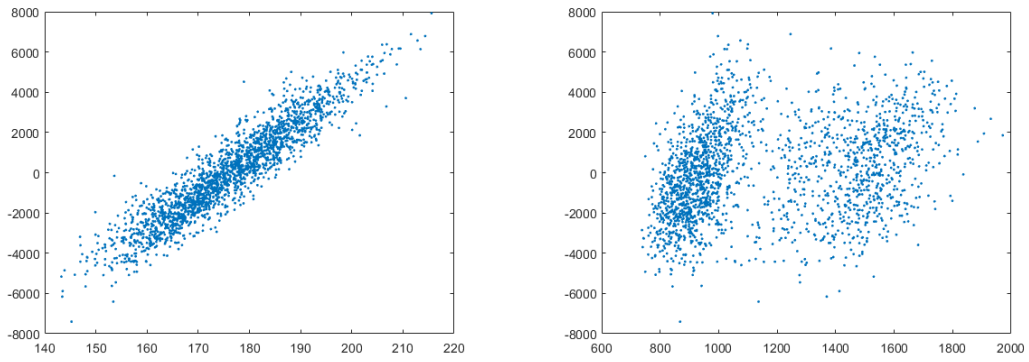

(a) Distribution: head breadth and w_1 (b) Distribution: chest circumference and w_1

Figure 6.1: Joint distributions of: (a) the head breadths and the first shape parameter of the human body models; (b) the chest circumferences and the first shape parameter of the human body models.

Normal distribution has very good analytical properties such as the linear combination of normally distributed variables is still normally distributed. This property is utilized to compute the probabilistic distribution of structural performance variation across the population. Another good analytical property of normal distribution is that given the joint distribution of two vectors (e.g. shape parameters and feature points), the conditional distribution of one vector on the other is still normal distribution. In parametric shape design, the conditional mean can be used for shape reconstruction (from feature points or sizing dimensions), and the conditional variance is used for feature point identification and dimension selection in this work.

To preserve the good properties of normal distribution, when the shape parameters are not normally distributed or the joint distribution does not follow the normal distribution, multi-variable transformation method [66] can be used to transform the data to close to normal distribution. This could be an interesting work for the future.

However, transforming the data to normal distribution also means loss of information, since normal distributions have no "inner structures", this may not always be desirable. Our statistical shape modeling approach builds on the assumption that the shapes are normally distributed and uses principal component analysis to extract the shape bases, the obtained model is a linear model. Alternative techniques for statistical shape learning can be considered such as the support vector machine (SVM) [77; 78], Gaussian process latent variable models (GPLVMs) [79; 80], and neural networks [81; 82], which learn

nonlinear models and have the potential to account for the inner structures of the shape data. For example, for the human body shape models, the inner structures correspond to different feature vectors for males and females and for different body types. The challenges for applying the foregoing nonlinear methods in shape learning include the considerable amount of time needed for learning and the risk of over-fitting, especially when the training set is not big enough. In image recognition people work with millions of images (e.g. ImageNet [83]), however, for shape learning, the current largest open dataset contains just a few thousands of shapes [1]. Parallelized computing techniques can be applied to solve the time issue. Reinforcement learning [84; 85] can be considered and combined to relieve the heavy dependency on the training data. A very inspirational news recently is that AlphaGo Zero beats AlphaGo in all the 100 games they played by three days of reinforcement learning [85] without the external training data that represent the human knowledge.

- Another limitation of our approach is that the shape instantiation is subject to local minimum due to the discrete nature of the optimization formula (4.3) which is essentially an NP hard problem [48; 60]. However, the examples show that in most cases we can find the correct shape instance even when the subject shape deviates significantly from the mean shape. For the failed case, a few landmarks can be added to guide the deformation (the number of landmarks needed will be much smaller than that of the free-form deformation). Future research on this issue includes comparing the effects of different landmarks on shape registration by free-form deformation and on shape instantiation with

large shape deviations. A bold guess here is that the landmarks that capture the shape variations of the population would perform better in shape registration (e.g. when evaluated by the multi-correlation metric in Chapter 4).

- The developed 1st order Taylor expansion approach is a linear approximation of the true FE solution, and the use of multi-point Taylor expansion makes it possible to account for non-linearity. For shapes with large variations, it would be interesting to compare our multi-point Taylor expansion with higher-order approximations. The future work would include extending the proposed Taylor expansion approach to 3D finite element analysis and to other physical problems whose solutions are highly nonlinear and even oscillatory with respect to the design parameters. The challenges are: 1) how to efficiently perform sensitivity analysis for these problems; and 2) how to address the highly nonlinearity and potential oscillations of the solution of these problem based on the developed approach.

Bibliography

[1] K. M. Robinette, S. Blackwell, H. Daanen, M. Boehmer, S. Fleming, Civilian american and european surface anthropometry resource (caesar), final report. volume 1. summary, Tech. rep., DTIC Document (2002).

[2] R. Ball, J. Molenbroek, Measuring chinese heads and faces, in: Proceedings of the 9th international congress of physiological anthropology. Human diversity: design for life, 2008, pp. 150–5.

[3] OAI, The osteoarthritis initiative (OAI), `https://oai.epi-ucsf.org/datarelease/About.asp`, [Online; 2017-01-25] (2017).

[4] S.-Y. Baek, K. Lee, Statistical foot-shape analysis for mass-customisation of footwear, International Journal of Computer Aided Engineering and Technology 8 (1-2) (2016) 80–98.

[5] C.-Y. Tseng, I.-J. Wang, C.-H. Chu, Product personalization using 3d parametric face models: An example of the eyeglass frame design, in: ASME 2015 International Design Engineering Technical Conferences and Computers and Information in Engineering Conference, American Society of Mechanical Engineers, 2015, pp. V01BT02A018–V01BT02A018.

[6] R. Bryan, P. B. Nair, M. Taylor, Use of a statistical model of the whole femur in a large scale, multi-model study of femoral neck fracture risk, Journal of biomechanics 42 (13) (2009) 2171–2176.

[7] C. Martin, W. Sun, Comparison of transcatheter aortic valve and surgical bioprosthetic valve durability: A fatigue simulation study, Journal of biomechanics 48 (12) (2015) 3026–3034.

[8] C. Martin, W. Sun, J. Elefteriades, Patient-specific finite element analysis of ascending aorta aneurysms, American Journal of Physiology-Heart and Circulatory Physiology 308 (10) (2015) H1306–H1316.

[9] J. E. Bischoff, Y. Dai, C. Goodlett, B. Davis, M. Bandi, Incorporating population-level variability in orthopedic biomechanical analysis: A review, Journal of biomechanical engineering 136 (2) (2014) 021004.

[10] D. Lacko, T. Huysmans, J. Vleugels, G. De Bruyne, M. M. Van Hulle, J. Sijbers, S. Verwulgen, Product sizing with 3d anthropometry and k-medoids clustering, Computer-Aided Design 91 (2017) 60–74.

[11] Y. Jun, K. Choi, Design of patient-specific hip implants based on the 3d geometry of the human femur, Advances in Engineering Software 41 (4) (2010) 537–547.

[12] W. Li, D. D. Anderson, J. K. Goldsworthy, J. L. Marsh, T. D. Brown, Patient-specific finite element analysis of chronic contact stress exposure after intraarticular fracture of the tibial plafond, Journal of orthopaedic research 26 (8) (2008) 1039–1045.

[13] C.-H. Chu, Y.-T. Tsai, C. C. Wang, T.-H. Kwok, Exemplar-based statistical model for semantic parametric design of human body, Computers in Industry 61 (6) (2010) 541–549.

[14] C. C. Wang, Parameterization and parametric design of mannequins, Computer-Aided Design 37 (1) (2005) 83–98.

[15] S. Wuhrer, C. Shu, P. Bose, Automatically creating design models from 3d anthropometry data, Journal of Computing and Information Science in Engineering 12 (4) (2012) 041007.

[16] B. Allen, B. Curless, Z. Popović, The space of human body shapes: reconstruction and parameterization from range scans, in: ACM Transactions on Graphics (TOG), Vol. 22, ACM, 2003, pp. 587–594.

[17] V. Blanz, A. Mehl, T. Vetter, H.-P. Seidel, A statistical method for robust 3D surface reconstruction from sparse data, in: 3D Data Processing, Visualization and Transmission, 2004. 3DPVT 2004. Proceedings. 2nd International Symposium on, IEEE, 2004, pp. 293–300.

[18] X. Chen, A. Saparov, B. Pang, T. Funkhouser, Schelling points on 3d surface meshes, ACM Transactions on Graphics (TOG) 31 (4) (2012) 29.

[19] D. Anguelov, P. Srinivasan, D. Koller, S. Thrun, J. Rodgers, J. Davis, Scape: shape completion and animation of people, in: ACM Transactions on Graphics (TOG), Vol. 24, ACM, 2005, pp. 408–416.

[20] W. Zhang, M. Brady, Feature Point Detection for Non-rigid Registration of Digital Breast Tomosynthesis Images, in: Digital Mammography/IWDM, Springer, 2010, pp. 296–303.

[21] T. Kadir, M. Brady, Saliency, scale and image description, International Journal of Computer Vision 45 (2) (2001) 83–105.

[22] C. H. Lee, A. Varshney, D. W. Jacobs, Mesh saliency, in: ACM transactions on graphics (TOG), Vol. 24, ACM, 2005, pp. 659–666.

[23] S. Katz, G. Leifman, A. Tal, Mesh segmentation using feature point and core extraction, The Visual Computer 21 (8-10) (2005) 649–658.

[24] S.-Y. Baek, K. Lee, Parametric human body shape modeling framework for human-centered product design, Computer-Aided Design 44 (1) (2012) 56–67.

[25] M. A. Baldwin, J. E. Langenderfer, P. J. Rullkoetter, P. J. Laz, Development of subject-specific and statistical shape models of the knee using an efficient segmentation and mesh-morphing approach, computer methods and programs in biomedicine 97 (3) (2010) 232–240.

[26] L. Grassi, N. Hraiech, E. Schileo, M. Ansaloni, M. Rochette, M. Viceconti, Evaluation of the generality and accuracy of a new mesh morphing procedure for the human femur, Medical engineering & physics 33 (1) (2011) 112–120.

[27] M. Bucki, C. Lobos, Y. Payan, A fast and robust patient specific finite element mesh registration technique: application to 60 clinical cases, Medical image analysis 14 (3) (2010) 303–317.

[28] R. Bryan, P. S. Mohan, A. Hopkins, F. Galloway, M. Taylor, P. B. Nair, Statistical modelling of the whole human femur incorporating geometric and material properties, Medical engineering & physics 32 (1) (2010) 57–65.

[29] Y. Zhang, X. Liang, et al., An atlas-based geometry pipeline for cardiac hermite model construction and diffusion tensor reorientation, Medical image analysis 16 (6) (2012) 1130–1141.

[30] G. Stefanou, The stochastic finite element method: past, present and future, Computer Methods in Applied Mechanics and Engineering 198 (9) (2009) 1031–1051.

[31] S. Reh, J.-D. Beley, S. Mukherjee, E. H. Khor, Probabilistic finite element analysis using ansys, Structural Safety 28 (1) (2006) 17–43.

[32] P. Laz, M. Browne, A review of probabilistic analysis in orthopaedic biomechanics, Proceedings of the Institution of Mechanical Engineers, Part H: Journal of Engineering in Medicine 224 (8) (2010) 927–943.

[33] Ö. Çavdar, A. Bayraktar, A. Çavdar, S. Adanur, Perturbation based stochastic finite element analysis of the structural systems with composite sections under earthquake forces.

[34] I. L. Dryden, K. V. Mardia, Statistical shape analysis, Vol. 4, J. Wiley Chichester, 1998.

[35] C. Rao, C. K. Fitzpatrick, P. J. Rullkoetter, L. P. Maletsky, R. H. Kim, P. J. Laz, A statistical finite element model of the knee accounting for shape and alignment variability, Medical engineering & physics 35 (10) (2013) 1450–1456.

[36] F. Galloway, M. Kahnt, H. Ramm, P. Worsley, S. Zachow, P. Nair, M. Taylor, A large scale finite element study of a cementless osseointegrated tibial tray, Journal of biomechanics 46 (11) (2013) 1900–1906.

[37] N. Metropolis, S. Ulam, The monte carlo method, Journal of the American statistical association 44 (247) (1949) 335–341.

[38] G. Schuëller, Developments in stochastic structural mechanics, Archive of Applied Mechanics 75 (10-12) (2006) 755–773.

[39] F. Galloway, P. Worsley, M. Stokes, P. Nair, M. Taylor, Development of a statistical model of knee kinetics for applications in pre-clinical testing, Journal of biomechanics 45 (1) (2012) 191–195.

[40] M. B. Stegmann, D. D. Gomez, A brief introduction to statistical shape analysis, Informatics and Mathematical Modelling, Technical University of Denmark, DTU 15 (2002) 11.

[41] T. F. Cootes, C. J. Taylor, Active shape modelsâŁ”âŁ˜smart snakesâŁ™, in: BMVC92, Springer, 1992, pp. 266–275.

[42] T. F. Cootes, C. J. Taylor, D. H. Cooper, J. Graham, Active shape models-their training and application, Computer vision and image understanding 61 (1) (1995) 38–59.

[43] T. F. Cootes, C. J. Taylor, D. H. Cooper, J. Graham, Training models of shape from sets of examples, in: BMVC92, Springer, 1992, pp. 9–18.

[44] D. Cremers, Dynamical statistical shape priors for level set-based tracking, Pattern Analysis and Machine Intelligence, IEEE Transactions on 28 (8) (2006) 1262–1273.

[45] B. Amberg, S. Romdhani, T. Vetter, Optimal step Non-rigid ICP algorithms for surface registration, in: Computer Vision and Pattern Recognition, 2007. CVPR'07. IEEE Conference on, IEEE, 2007, pp. 1–8.

[46] H. Wang, B. Fei, Non-rigid point registration for 2D curves and 3D surfaces and its various applications, Physics in medicine and biology 58 (12) (2013) 4315.

[47] H. Chui, A. Rangarajan, A new point matching algorithm for Non-rigid registration, Computer Vision and Image Understanding 89 (2) (2003) 114–141.

[48] S. Belongie, J. Malik, J. Puzicha, Matching shapes, in: Computer Vision, 2001. ICCV 2001. Proceedings. Eighth IEEE International Conference on, Vol. 1, IEEE, 2001, pp. 454–461.

[49] T. Cootes, E. Baldock, J. Graham, An introduction to active shape models, Image Processing and Analysis (2000) 223–248.

[50] K. K. Choi, N.-H. Kim, Structural sensitivity analysis and optimization 1: linear systems, Springer Science & Business Media, 2006.

[51] D. Zhang, G. Lu, Review of shape representation and description techniques, Pattern recognition 37 (1) (2004) 1–19.

[52] P. J. Besl, N. D. McKay, Method for registration of 3D shapes, in: Robotics-DL tentative, International Society for Optics and Photonics, 1992, pp. 586–606.

[53] H. Li, R. W. Sumner, M. Pauly, Global correspondence optimization for Non-rigid registration of depth scans, in: Computer graphics forum, Vol. 27, Wiley Online Library, 2008, pp. 1421–1430.

[54] X. Huang, N. Paragios, D. N. Metaxas, Shape registration in implicit spaces using information theory and free form deformations, Pattern Analysis and Machine Intelligence, IEEE Transactions on 28 (8) (2006) 1303–1318.

[55] R. H. Davies, C. J. Twining, T. F. Cootes, J. C. Waterton, C. J. Taylor, A minimum description length approach to statistical shape modeling, Medical Imaging, IEEE Transactions on 21 (5) (2002) 525–537.

[56] R. H. Davies, C. J. Twining, T. F. Cootes, C. J. Taylor, Building 3D statistical shape models by direct optimization, Medical Imaging, IEEE Transactions on 29 (4) (2010) 961–981.

[57] K. Li, X. Qian, Direct diffeomorphic reparameterization for correspondence optimization in statistical shape modeling, Computer-Aided Design 64 (2015) 33–54.

[58] X. Wang, X. Qian, A statistical atlas based approach to automated subject-specific FE modeling, Computer-Aided Design 70 (2016) 67–77.

[59] T. W. Sederberg, S. R. Parry, Free-form deformation of solid geometric models, in: ACM SIGGRAPH computer graphics, Vol. 20, ACM, 1986, pp. 151–160.

[60] S. Belongie, J. Malik, J. Puzicha, Shape matching and object recognition using shape contexts, Pattern Analysis and Machine Intelligence, IEEE Transactions on 24 (4) (2002) 509–522.

[61] J. C. Gower, Generalized procrustes analysis, Psychometrika 40 (1) (1975) 33–51.

[62] I. Guyon, A. Elisseeff, An introduction to variable and feature selection, Journal of machine learning research 3 (Mar) (2003) 1157–1182.

[63] K. Li, X. Qian, C. Martin, W. Sun, Toward patient-specific computational study of aortic diseases: a population based shape modeling approach, in: ASME 2014 International Design Engineering Technical Conferences and Computers and Information in Engineering Conference, American Society of Mechanical Engineers, 2014, pp. V01AT02A080–V01AT02A080.

[64] M. A. Halanski, T. Yildirim, R. Chaudhary, M. S. Chin, E. Leiferman, Periosteal fiber transection during periosteal procedures is crucial to accelerate growth in the rabbit model, Clinical Orthopaedics and Related Research® 474 (4) (2016) 1028–1037.

[65] L. Pishchulin, S. Wuhrer, T. Helten, C. Theobalt, B. Schiele, Building statistical shape spaces for 3D human modeling, Pattern Recognition 67 (2017) 276–286.

[66] D. Wackerly, W. Mendenhall, R. Scheaffer, Mathematical statistics with applications, Cengage Learning, 2007.

[67] T. W. Anderson, An introduction to multivariate statistical analysis, Vol. 2, Wiley New York, 1958.

[68] H. Lin, K. Tang, A. Joneja, H. Bao, Generating strictly non-self-overlapping structured quadrilateral grids, Computer-Aided Design 39 (9) (2007) 709–718.

[69] X. Wang, X. Qian, An optimization approach for constructing trivariate B-spline solids, Computer-Aided Design 46 (2014) 179–191.

[70] X. Qian, O. Sigmund, Isogeometric shape optimization of photonic crystals via Coons patches, Computer Methods in Applied Mechanics and Engineering 200 (25) (2011) 2237–2255.

[71] T. Heimann, H.-P. Meinzer, Statistical shape models for 3D medical image segmentation: a review, Medical image analysis 13 (4) (2009) 543–563.

[72] X. Qian, Full analytical sensitivities in NURBS based isogeometric shape optimization, Computer Methods in Applied Mechanics and Engineering 199 (29) (2010) 2059–2071.

[73] F. L. Bookstein, Principal warps: Thin-plate splines and the decomposition of deformations, IEEE Transactions on Pattern Analysis & Machine Intelligence (6) (1989) 567–585.

[74] J. Kent, K. Mardia, The link between kriging and thin-plate splines (1994).

[75] N. Hasler, C. Stoll, M. Sunkel, B. Rosenhahn, H.-P. Seidel, A statistical model of human pose and body shape, in: Computer Graphics Forum, Vol. 28, Wiley Online Library, 2009, pp. 337–346.

[76] K. Grochow, S. L. Martin, A. Hertzmann, Z. Popović, Style-based inverse kinematics, in: ACM transactions on graphics (TOG), Vol. 23, ACM, 2004, pp. 522–531.

[77] C. Cortes, V. Vapnik, Support vector machine, Machine learning 20 (3) (1995) 273–297.

[78] J. A. Suykens, J. Vandewalle, Least squares support vector machine classifiers, Neural processing letters 9 (3) (1999) 293–300.

[79] N. D. Lawrence, Gaussian process latent variable models for visualisation of high dimensional data, in: Advances in neural information processing systems, 2004, pp. 329–336.

[80] C. H. Ek, P. H. Torr, N. D. Lawrence, Gaussian process latent variable models for human pose estimation, in: International workshop on machine learning for multimodal interaction, Springer, 2007, pp. 132–143.

[81] G. E. Hinton, R. R. Salakhutdinov, Reducing the dimensionality of data with neural networks, science 313 (5786) (2006) 504–507.

[82] Y. LeCun, Y. Bengio, G. Hinton, Deep learning, Nature 521 (7553) (2015) 436–444.

[83] J. Deng, W. Dong, R. Socher, L.-J. Li, K. Li, L. Fei-Fei, Imagenet: A large-scale hierarchical image database, in: Computer Vision and Pattern Recognition, 2009. CVPR 2009. IEEE Conference on, IEEE, 2009, pp. 248–255.

[84] R. S. Sutton, A. G. Barto, Reinforcement learning: An introduction, Vol. 1, MIT press Cambridge, 1998.

[85] D. Silver, J. Schrittwieser, K. Simonyan, I. Antonoglou, A. Huang, A. Guez, T. Hubert, L. Baker, M. Lai, A. Bolton, et al., Mastering the game of go without human knowledge, Nature 550 (7676) (2017) 354–359.